Dynamical properties of excitonic quasi-particles in II-VI semiconductors

Dissertation

presented to the Faculty of Physics of the
TU Dortmund University, Germany

by
Tillmann Godde

technische universität
dortmund

Dortmund, July 2013

Contents

Chapter 1

Introduction

Excitons are quasi-particles, that can form in semiconductors and consist of an electron-hole pair bound together by Coulumb attraction [1]. They can be excited by means of light and can form other quasi-particles. This work is concerned with the study of the dynamics of two different excitonic quasi-particles and how they are influenced by a magnetic field.

The first type of quasi-particles studied in this work are exciton polaritons. Exciton polaritons are the result between coupling and photons to excitons [1, 2]. An exciton polariton shares the characteristics of both excitons and photons [2]. Though it is possible to localize a polariton by confining the electromagnetic field of the light, which allows the study of quantum-mechanical phenomena like Bose-Einstein condensates [3, 4], polaritons are propagating states. Due to the excitonic part the velocity of their propagation is reduced. In bulk (Cd,Zn)Te crystals, the material used in this work, one can observe a delay up to 350 ps in a 755 µm thick crystal. This effect can be used for a delay-line memory in optical computation.

Furthermore, one can understand all light propagation inside a bulk crystal as polariton propagation. In this case, the polariton is not formed with one resonance, but a multitude of resonances [5, 6]. This is of special importance for magnetic-field-induced polarization effects. Due to the larger number of resonances, it is not always possible to determine the origin of a polarization effect [7].

One of these effects is magneto-spatial dispersion, which manifests as linear birefringence. It has been studied previously in bulk CdTe crystals in Voigt geometry. From symmetry considerations one can deduce further properties on, e.g., its allowance [8]. But even though an excitonic origin has been suspected [9], no model predicting its spectral or magnetic dependence has so far been presented. The development and testing of such a model are important aims of this work. This is possible due to a new experimental setup that allows one to measure both the propagation speed and polarization state of light. As these measurements are performed in Faraday geometry a non-trivial spectral dependence of the Faraday

rotation is discovered.

Using linear birefringence and Faraday rotation, it is possible to manipulate the polarization of light in a controlled fashion by controlling the exciton resonance using, for example, strain. Since the polarization of light can be used to transport information, such an application would be useful, for example, in quantum computing.

The second type of excitonic quasi-particles are exciton magnetic polarons [10]. They are formed in diluted magnetic semiconductors due to sp-d exchange interaction between the spin of an exciton and the spin of manganese atoms by orienting the manganese spins which reduces the energy of the exciton. In contrast to propagating polaritons, initial localization of the exciton is necessary for the exciton magnetic polaron formation. Also, the formation takes time [10]. It is necessary to study the dynamics since the exciton lifetime and the formation time can be comparable, leading to incomplete polaron formation. Further, the formation is supported by confining the exciton in potential wells. So the formation dynamics have been studied extensively in non-magnetic quantum wells with magnetic (Cd,Mn)Te barriers and some magnetic quantum wells [10, 11, 12].

In recent years, the manufacturing of CdSe based quantum wells has become feasible, but the knowledge of the interaction of different CdSe based alloys is still limited. Studying formation dynamics of exciton magnetic polarons in this novel material has led to a more defined understanding of the nature of the used quantum well. Exciton magnetic polarons are interesting from a fundamental physics standpoint as they provide optically induced ferromagnetism.

Chapter 2

Theory of excitons in zincblende II-VI semiconductors

2.1 Excitons in II-VI zincblende semiconductors

2.1.1 Crystal structure

CdTe is a II-VI semiconductor that crystallizes in the zincblende structure at normal pressure [13]. Its unit cell is shown in figure 2-1. The crystal lattice can be constructed from two face-centered cubic(fcc) lattices shifted against each other by a quarter of a unit cell diagonal. One fcc-lattice consists of cadmium while the

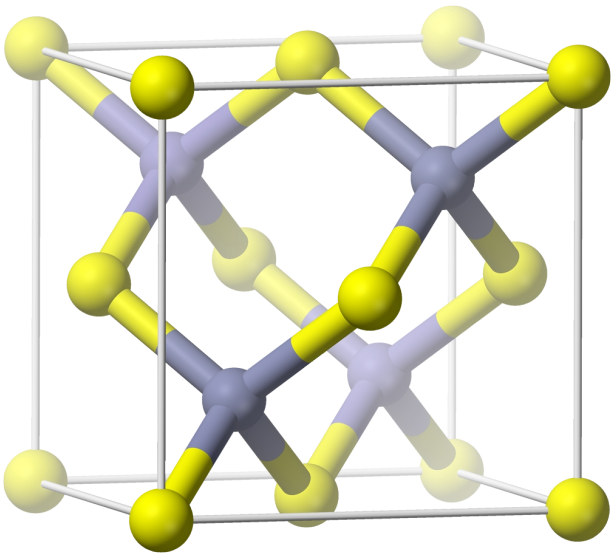

Figure 2-1: Unit cell of CdTe [14]. Gray spheres represent Cd atoms while yellow spheres represent Te atoms.

other of tellurium. Each cadmium atom is surrounded by 4 tellurium atoms. These

4 atoms are aligned like the vertices(corners) of a regular tetrahedron (triangular pyramid). This configuration determines the symmetry of the crystal. It is of T_d point group. This group contains all symmetry operations that transform a regular tetrahedron into itself [15].

2.1.2 Band structure

The band structure of CdTe is shown in figure 2-2. In this figure the filled valence-bands have an energy below $E = 0$ and the empty conduction-bands have a energy above $E = 0$. The fundamental band gap is between the valence-band with the highest energy and the conduction-band with the lowest. The smallest band gap is found at the Γ-point, the center of the first Brillouin-Zone, which makes the CdTe a direct band gap semiconductor. For both bands the electrons at the Γ-point do not have momentum and do not propagate. Further for both bands the density of states is small. There are several band gaps between empty conduction-bands

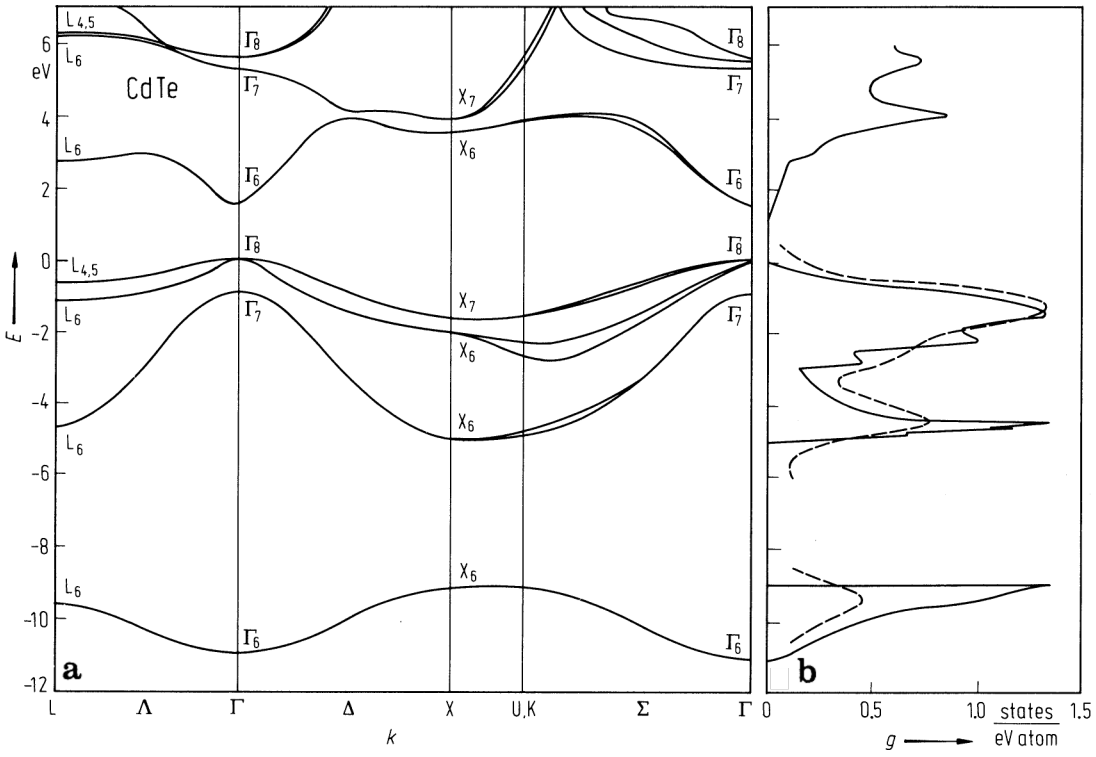

Figure 2-2: Band structure (a) and density of states (b). Solid curves represent nonlocal pseudopotential calculations [16], while dashed curves represent data from ultraviolet photoemission spectroscopy measurements [17].

and full valence-bands at the X- and L-points of the Brillouin-Zone, where both bands have higher densities of states than those of the smallest band gap. These band gaps determine the refractive index of CdTe [5, 6].

2.1.3 Wannier-Mott excitons

Excitons are quasi-particles that are formed from a valence-band hole and a conduction-band electron bound by their Coulomb interaction. They are either called Frenkel or Wannier-Mott excitons, depending on the volume of the wavefunction of the electron and hole [1]. In a Frenkel exciton the wavefunction's volume does not exceed one unit cell of the crystal. The other extreme are Wannier-Mott excitons. Here, the volume of the electron wavefunction and the hole wavefunction is large* These are the excitons studied in this work. They are described analogous to the model of a hydrogen atom, but their binding energy $E_n(\vec{k})$ is much smaller.

$$E_n(\vec{k}) = -\frac{e^4\mu}{2\hbar^2\kappa^2 n^2} + \underbrace{\frac{\hbar^2\vec{k}^2}{2M}}_{\text{kinetic energy}} . \tag{2.1}$$

Here κ is the macroscopic dielectric constant, while $n = 1, 2, \ldots, \infty$ is the principle quantum number corresponding to the shell in an atom. Also $\mu^{-1} = (m_\mathrm{e}^*)^{-1} + (m_\mathrm{h}^*)^{-1}$ and $M = m_\mathrm{e}^* + m_\mathrm{h}^*$, where m_e^* is the effective mass of the electron and m_h^* the effective mass of the hole. $\hbar K$ describes the momentum of the center of the mass. An exciton can propagate through the crystal, leading to a kinetic energy of $\frac{\hbar^2 K^2}{2M}$ [1].

Before an electron and a hole can form an exciton is has to be lifted from the valence-band into conduction-band. The corresponding energy of excitation is the band gap energy E_G between the edges of the valence- and conduction-band. If an exciton is formed it is usually in the lowest state $n = 1$ leading to an exciton energy E_exc of

$$E_\mathrm{exc} = E_\mathrm{G} - \underbrace{\frac{e^4\mu}{2\hbar^2\kappa^2}}_{E_\mathrm{x}} + \frac{\hbar^2 K^2}{2M}. \tag{2.2}$$

E_x is the exciton binding energy also known as the "exciton Rydberg" energy [1]. From the "exciton Rydberg" one can estimate the "exciton Bohr radius" a_x which is used as a measure of the size of the exciton wavefunction [1]

$$E_\mathrm{x} = \frac{e^4\mu}{2\hbar^2\kappa^2} = \frac{e^2}{2\kappa a_\mathrm{x}} = \frac{\hbar^2}{2\mu a_\mathrm{x}^2}. \tag{2.3}$$

*In CdTe bulk crystals a unit cell has a size of 0.4293 nm [18], while an exciton has a Bohr radius between $a_\mathrm{x} = 6.0\,\mathrm{nm}$[19] and $a_\mathrm{x} = 7.5\,\mathrm{nm}$[20].

2.2 Propagation of exciton polaritons

A polariton is a mixed particle formed by a photon and an exciton due to the coupling between photon and exciton. It has theoretically been predicted by Pekar[21] and Hopfield[22]. It affects the propagation of light, and also the properties of light during propagation. This section introduces the theory necessary to calculate the propagation of an exciton polariton.

The usual way to describe the propagation of light is the dielectric constant and the refractive index. A short introduction is given in section 2.2.1. After this the polariton concept is introduced in section 2.2.2. In section 2.2.4 the concept of the dielectric constant is expanded to describe anisotropic media.

The second part of section 2.2 is dedicated to the change of polarization of light during polariton propagation. In order to quantify the polarization, an experimentally accessible quantity, the Stokes vector, is presented in section 2.2.5, together with a more theoretical one, the Jones vector.

Building upon the dielectric tensor, different kinds of polarization effects are presented in section 2.2.6. In section 2.2.7 a method for calculating the strength of polarization effects from excitonic parameters is demonstrated. Moreover, the relation between the delay introduced by an exciton and excitonic polarization effects is discussed in section 2.2.8.

2.2.1 Plane wave in an isotropic medium

Electromagnetic waves in dielectric media without free charges and currents are described by Maxwell's equations

$$\nabla\vec{D} = 0 \quad , \quad \nabla\vec{B} = 0 \ ,$$
$$\nabla\times\vec{E} = -\frac{1}{c}\frac{\partial\vec{B}}{\partial t} \quad , \quad \nabla\times\vec{H} = \frac{1}{c}\frac{\partial\vec{D}}{\partial t} \ .$$

Here $\vec{D} = \varepsilon\vec{E}$ is the electric induction, $\vec{H} = \frac{\vec{B}}{\mu}$ is the magnetic field, $\vec{E}$ is the electric field and $\vec{B}$ the magnetic induction. The material parameter ε is the dielectric constant, also called permittivity, while μ is called the permeability.

An electromagnetic wave can propagate in any direction and has different shapes, but for this work the simple idealized case of a plane wave propagating along $\vec{z}$ is sufficient. In this case, the electric field, found as a solution of Maxwell's equations takes the form [23]

$$\vec{E}(z,w,t) = \vec{A}e^{\mathrm{i}kz+\mathrm{i}\omega t} \ , \qquad (2.4)$$
$$\text{with } k = \sqrt{\mu\varepsilon}\frac{\omega}{c} \ .$$

Because in this spectral range μ is 1 for most semiconductors, including (Cd,Zn)Te, the wave vector is

$$k = \sqrt{\varepsilon}\frac{\omega}{c} = n\frac{\omega}{c} \tag{2.5}$$

with n being the refractive index. $\vec{A}$ is a complex vector describing the amplitude and phase of the oscillation. This vector is orthogonal to the direction of propagation. If the wave vector has an imaginary part light will be absorbed during propagation and equation (2.4) can be written as

$$\begin{aligned}
\vec{E}(z,w,t) &= \vec{A}(e^{-\Im(k)z+\mathrm{i}\omega t}e^{\mathrm{i}\Re(k)z+\mathrm{i}\omega t}) \ , \\
\text{with } \Re(k) &= \frac{\sqrt{\Re(\varepsilon)+\sqrt{\Re(\varepsilon)^2+\Im(\varepsilon)^2}}}{\sqrt{2}}\frac{\omega}{c} \\
\text{and } \Im(k) &= \frac{\sqrt{-\Re(\varepsilon)+\sqrt{\Re(\varepsilon)^2+\Im(\varepsilon)^2}}}{\sqrt{2}}\frac{\omega}{c} \ .
\end{aligned}$$

The phase of a wave propagates with the so-called phase velocity $v_p = \frac{c}{n}$. A wave packet like the polariton propagates with the group velocity $v_G = \frac{\partial\omega}{\partial k}$. From this one can define a group refractive index $n_G = \frac{c}{v_G}$. It can differ significantly from the refractive index n in the case of dispersion where ε is a function of ω

$$n_G = \frac{\partial}{\partial\omega}\Re(\omega\sqrt{\varepsilon(\omega)}). \tag{2.6}$$

2.2.2 The exciton polariton concept

If an exciton has a non-vanishing dipole, it can be excited by an electromagnetic wave. If the energy of the electromagnetic wave is close to that of the exciton, the two particles will form a new quasi-particle called exciton polariton [1]. To calculate the dispersion of the polariton the dielectric constant ε is used. The concept of the dielectric constant ε is introduced in section 2.2.1. As an exciton can be described as a hydrogen atom one may use the model of a Lorentz oscillator. The dielectric constant of an oscillator with a frequency of $\frac{\omega}{2\pi}$ is described as

$$\varepsilon = \varepsilon_0 + \frac{f}{\omega_{\mathrm{res}}^2 - \omega^2 - \mathrm{i}\omega\Gamma}, \tag{2.7}$$

where f is the oscillator strength, Γ is the dampening of the oscillator, ω_{res} the resonance frequency, and ω the frequency of the light. The background dielectric constant ε_0 represents contributions, such as different exciton states and higher band transitions [2]. As equation (2.7) is a function of the frequency of the exciting light it can be called dielectric function. A typical example is shown in figure 2-4. For ease of comparison an energy scale has been used. With increasing energy the

real part of ε increases. At the resonance energy $\Re(\varepsilon)$ changes sign and increases again to approach ε_b. For photon energies close resonance energy ε has a significant imaginary part which leads to absorption.

Equation (2.7) has been developed for an atom that does not propagate. Since the exciton can propagate and has kinetic energy as stated in equation (2.1), equation (2.7) has to be modified. The kinetic energy has to be added to the exciton resonance energy. When forming a polariton the exciton and photon share a common wave vector $\vec{k}$. This leads to a more complicated equation where the wavevectors $\vec{k}$ satisfy the dispersion equation

$$\left(\frac{c\vec{k}}{\omega}\right)^2 = \varepsilon_0 + \frac{4\pi\alpha_0\omega_0^2}{\omega_0^2 - \omega^2 + (\hbar k^2/M)\omega_0 - \mathrm{i}\omega\Gamma}. \tag{2.8}$$

In the dispersion equation $\alpha_0 = 2d^2/\hbar\omega_0$, d is the dipole matrix element for optical excitation of the exciton and $\hbar\omega_0$ is the exciton energy for $\vec{k} = 0$ [2]. For each propagation direction there are two solutions for this equation. Both are shown in

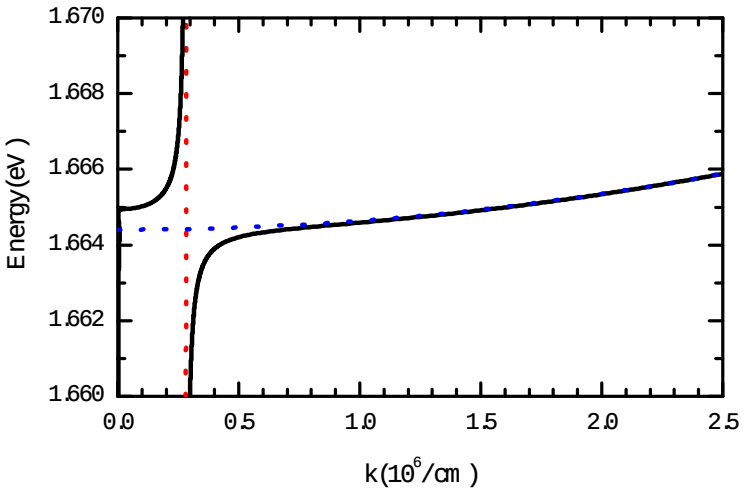

Figure 2-3: Dispersions of light (red dots), exciton (blue dots), upper and lower polariton branches calculated for $\varepsilon_0 = 11.2$, $\hbar\omega_0 = 1.6644\,\mathrm{eV}$, $4\pi\alpha_0 = 8.8 \times 10^{-3}$, $\hbar\Gamma = 8\,\mu\mathrm{eV}$ and $M = 1.6m_\mathrm{e}$ where m_e is the mass of a free electron.

figure 2-3 together with the dispersions of excitons and photons, which are depicted as a nearly vertical red dotted line and a blue dotted parabola, respectively. The two solutions are called upper and lower polariton branch. The one above the exciton parabola is the upper polariton branch (UP), while the one below the exciton parabola is the lower polariton branch (LP).

The upper polariton dispersion is shallow for low $\vec{k}$. With increasing $\vec{k}$ its slope increases until it follows the photon dispersion. The LP dispersion starts with a slope close to the photon dispersion at low energy. Then its slope decreases as the LP dispersion approaches the exciton dispersion. With further energy increase the polariton dispersion follows the exciton dispersion. The propagation speed, which

is determined by the slope of the dispersion, drops significantly when approaching the exciton resonance $\hbar\omega_0$.

The dependence of the exciton energy on the wave vector is called spatial dispersion [2]. One consequence is, that above a certain energy both branches exist. In this case, one can use the effective refractive index

$$\bar{n} = \frac{n_1 n_2 + \varepsilon_0}{n_1 + n_2}, \tag{2.9}$$

where n_1 and n_2 are the refractive indexes of the upper and lower branches, respectively, to describe the propagation of light. This is only necessary if the photon energy $\hbar\omega$ is close to the resonance energy $\hbar\omega_0$. For other energies the branch closer to the light dispersion dominates and the other branch can be neglected [2].

The resulting dielectric function is shown in figure 2-4. In comparison to the Lorentz oscillator, the increase of the dielectric function, when approaching the resonance from low energies, is not as pronounced. Further spatial dispersion leads to a slower approach to ε_0 for energies above the resonance energy and absorption in a wider spectral window.

Imperfect growing conditions may lead to a fluctuation of the exciton resonance energy $\hbar\omega_0$, called inhomogeneous broadening. Since the distribution of the exciton resonance energy can be described by a Gaussian with a width of Γ_{inh}, the dielectric function has to be convoluted with a Gaussian distribution. For a non-inhomogeneously broadened dielectric function $\varepsilon(\omega, \omega_0)$, where $\hbar\omega$ is the photon energy and $\hbar\omega_0$ is the resonance energy, the inhomogeneously broadened dielectric function $\varepsilon'(\omega, \omega_0)$ is

$$\varepsilon'(\omega, \omega_0) = \int_{-\infty}^{+\infty} \varepsilon(\omega, \omega_0 + \omega') \frac{\exp\left[-\frac{(\omega')^2}{2\Gamma_{\mathrm{inh}}^2}\right]}{\sqrt{2\pi}\Gamma_{\mathrm{inh}}} d\omega'. \tag{2.10}$$

2.2.3 Simplifications

Solving the dispersion relation shown in equation (2.8) is not always necessary and several simplifications can be done. For energies close to the resonance $|\omega_0 - \omega| \ll \omega_0$ one can simplify it to [2]

$$\left(\frac{c\vec{k}}{\omega}\right)^2 = \varepsilon_0 + \frac{4\pi\alpha_0\omega_0}{\omega_0 - \omega + (\hbar k^2/M) - \mathrm{i}\Gamma/2}.$$

For photon energies $\hbar\omega$ not too close to the exciton resonance $\hbar\omega_0$, where the influence of the spatial dispersion is very small $|\hbar k^2/M| \ll |\omega_0 - \omega|$, one can simply

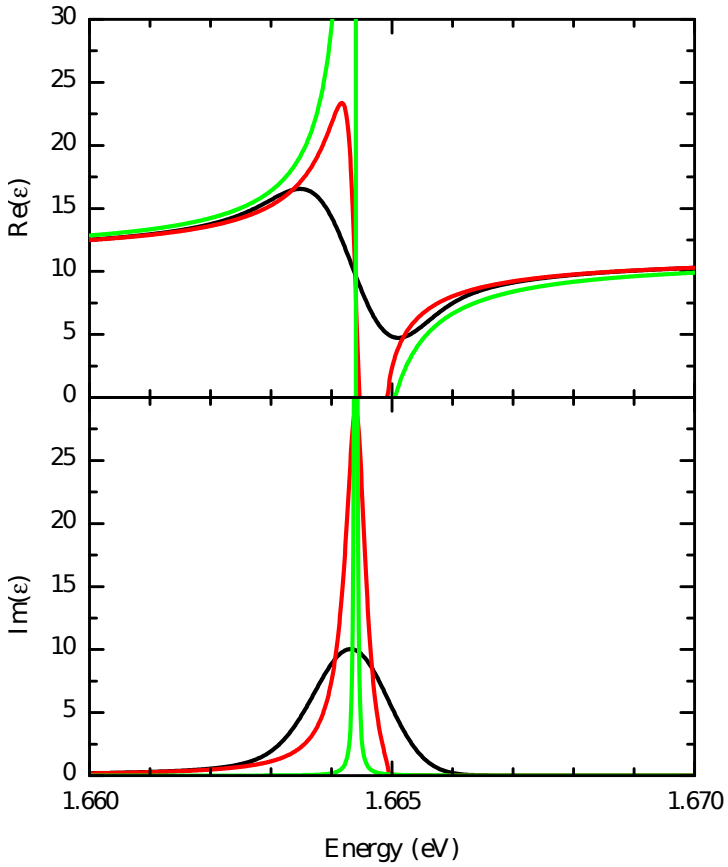

Figure 2-4: Dielectric functions of a simple Lorentz oscillator (green line) and polaritons with spatial dispersion without inhomogeneous broadening (red line) and with 1 meV in homogeneous broadening calculated for $\varepsilon_0 = 11.2$, $\hbar\omega_0 = 1.6644\,\mathrm{eV}$, $4\pi\alpha_0 = 8.8 \times 10^{-3}$, $\hbar\Gamma = 8\,\mu\mathrm{eV}$ and $M = 1.6 m_\mathrm{e}$.

calculate the dielectric constant as

$$\varepsilon(\omega) = \varepsilon_0 + \frac{\varepsilon_0 \omega_\mathrm{LT}}{\omega_0 - \omega - \mathrm{i}\Gamma/2}, \tag{2.11}$$

where $\omega_\mathrm{LT} = \frac{2\pi\alpha_0\omega_0}{\varepsilon_0}$ is the longitudinal-transverse splitting. The complex dispersion of the simplified model (SM) without spatial dispersion is presented in figure 2-5. For comparison, the dispersions of the LP branch and UP branch are also shown in figure 2-5. These dispersions are calculated for $Cd_{0.88}Zn_{0.12}Te$, which is the material used in this study, at a temperature of $T = 1.8\,\mathrm{K}$.

The SM does only have one branch. As long as the UP branch wavevector is real, UP and SM are in good agreement. For low energies up to 1.663 eV the SM and LP branches are in good agreement both for real and imaginary parts of the wavevector. In the small energy regime in between there are significant differences both in the real and the imaginary parts of k. In this energy window one cannot neglect spatial dispersion and needs to use the solutions of equation (2.8), but for energies below 1.663 eV the simple model is sufficient.

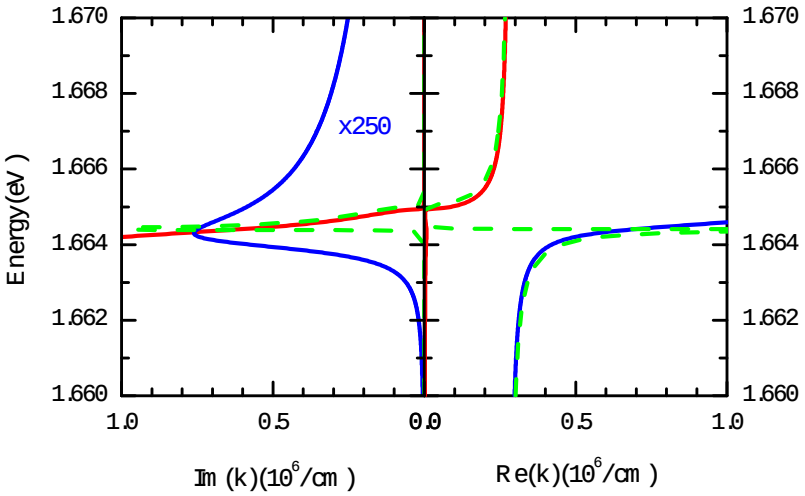

Figure 2-5: Complex dispersions of the LP branch (blue line), UP branch (red line) and simple Lorentz oscillator (dashed green line) without spatial dispersion calculated for $\varepsilon_0 = 11.2$, $\omega_0 = 1.6644\,\mathrm{eV}$, $4\pi\alpha_0 = 8.8 \times 10^{-3}$ and $M = 1.6 m_\mathrm{e}$.

In a crystal with significant inhomogeneous broadening of the exciton resonance one has to take into account this broadening. In this case one uses equation (2.10) with equation (2.11), and the resulting dielectric function reads

$$\varepsilon(\omega, \omega_0) = \varepsilon_0 \int_{-\infty}^{+\infty} \frac{\varepsilon_0 \omega_\mathrm{LT}}{\omega' - \omega - \mathrm{i}\Gamma/2} \frac{\exp\left[-\frac{(\omega'-\omega_0)^2}{2\Gamma_\mathrm{inh}^2}\right]}{\sqrt{2\pi}\Gamma_\mathrm{inh}} d\omega'. \tag{2.12}$$

2.2.4 Plane wave in an anisotropic medium

The dielectric constant is used to describe the propagation of electromagnetic waves in a medium. This parameter is a scalar in isotropic media, but has to be described as a tensor in anisotropic media. If the wave propagates along $\vec{z}$ this tensor can be simplified to a 2x2 matrix

$$\varepsilon_{ij} = \begin{pmatrix} \varepsilon_{xx} & \varepsilon_{xy} \\ \varepsilon_{yx} & \varepsilon_{yy} \end{pmatrix}. \tag{2.13}$$

Using symmetry analysis [8] one can identify three contributions

$$\varepsilon_{xy} = -\varepsilon_{yx} = \mathrm{i}\varepsilon_\mathrm{off} \tag{2.14}$$

$$\varepsilon_{xx} = \varepsilon_\mathrm{i} + \varepsilon_\mathrm{dia}/2 \;,\; \varepsilon_{yy} = \varepsilon_\mathrm{i} - \varepsilon_\mathrm{dia}/2 \tag{2.15}$$

to the dielectric tensor. Here ε_i is the dielectric constant for the isotropic case without polarization effects, ε_dia and ε_off are the contributions to the diagonal and off-diagonal elements of ε_{ij}, respectively. ε_{ij} can be diagonalized yielding two

eigenvectors $\vec{E}_1$ and $\vec{E}_2$ and eigenvalues ε_1 and ε_2. These read

$$\vec{E_{1,2}} = \begin{pmatrix} \frac{\mathrm{i}(\varepsilon_{\mathrm{dia}} \mp \sqrt{\varepsilon_{\mathrm{dia}}^2 + 4\varepsilon_{\mathrm{off}}^2})}{2\varepsilon_{\mathrm{off}}} \\ 1 \end{pmatrix}, \tag{2.16}$$

$$\varepsilon_{1,2} = \frac{2\varepsilon_{\mathrm{i}} \mp \sqrt{\varepsilon_{\mathrm{dia}}^2 + 4\varepsilon_{\mathrm{off}}^2}}{2}. \tag{2.17}$$

The propagation of an electromagnetic wave along $\vec{z}$ can now be described as a superposition of two eigenwaves

$$\vec{E}(z,t) = A_1\vec{E}_1 e^{\mathrm{i}n_1 z/c - \mathrm{i}\omega t} + A_2\vec{E}_2 e^{\mathrm{i}n_2 z/c - \mathrm{i}\omega t} \tag{2.18}$$

with complex amplitudes $A_{1,2}$ and refractive indices $n_{1,2} = \sqrt{\varepsilon_{1,2}}$. The complex amplitudes A_1 and A_2 are determined by the polarization of light entering the sample. Assuming that the crystal starts at $z = 0$ and neglecting reflection at the the electric fields inside and outside of the sample $\vec{E}_{\mathrm{extern}}$ have to match.

$$\vec{E}_{\mathrm{extern}} = A_1\vec{E}_1 + A_2\vec{E}_2$$

For example, in the case of light linearly polarized along $\vec{x}$ with $\vec{E}_{\mathrm{extern}} = \begin{pmatrix} 1 \\ 0 \end{pmatrix}$ the amplitudes are

$$A_{1,2} = \mp \frac{\mathrm{i}\varepsilon_{\mathrm{off}}}{\sqrt{\varepsilon_{\mathrm{dia}}^2 + 4\varepsilon_{\mathrm{off}}^2}} \ . \tag{2.19}$$

Another example is positive circularly (right-handed) polarized light with $\vec{E}_{extern} = \sqrt{2}\begin{pmatrix} -\mathrm{i} \\ 1 \end{pmatrix}$. In this case, the amplitudes are

$$A_{1,2} = \frac{\mathrm{i}[\sqrt{\varepsilon_{\mathrm{dia}}^2 + 4\varepsilon_{\mathrm{off}}^2} \mp (\varepsilon_{\mathrm{dia}} + 2\varepsilon_{\mathrm{off}})]}{\sqrt{8\varepsilon_{\mathrm{dia}}^2 + 32\varepsilon_{\mathrm{off}}^2}} \ . \tag{2.20}$$

2.2.5 Stokes parameters

To represent the state of light one may use the Stokes parameters introduced in 1852 by G. G. Stokes [24, 25].

They are often used by experimentalists, as they only use easily accessible observables. Assuming that light propagates along $\vec{z}$ in a Cartesian coordinate

system with the axes $\vec{x}$, $\vec{y}$ and $\vec{z}$, then the Stokes parameters are

$$\mathcal{S}_0 = I = I_x + I_y = I_{x'} + I_{y'} = I_{\sigma+} + I_{\sigma-}, \tag{2.21a}$$
$$\mathcal{S}_1 = Q = I_x - I_y, \tag{2.21b}$$
$$\mathcal{S}_2 = U = I_{x'} - I_{y'}, \tag{2.21c}$$
$$\mathcal{S}_3 = V = I_{\sigma+} - I_{\sigma-}. \tag{2.21d}$$

I_x and I_y are the intensities of light linearly polarized along $\vec{x}$ and $\vec{y}$, respectively, while $I_{x'}$ and $I_{y'}$ are the intensities of light linearly polarized along $\vec{x'} = \frac{1}{\sqrt{2}} \begin{pmatrix} 1 \\ 1 \end{pmatrix}$ and $\vec{y'} = \frac{1}{\sqrt{2}} \begin{pmatrix} -1 \\ 1 \end{pmatrix}$. Further, $I_{\sigma+}$ and $I_{\sigma-}$ are the intensities of positive and negative (left-handed) circularly polarized light.

The Stokes vector contains more information than just the polarization state of light. $\mathcal{S}_0$ is the intensity of the light. If one wants to only study the polarization state of light, the normalized Stokes vector $\vec{S} = (S_1, S_2, S_3)$, will be sufficient.

$$S_1 = \frac{\mathcal{S}_1}{\mathcal{S}_0} = \frac{I_x - I_y}{I_x + I_y}, \tag{2.22a}$$
$$S_2 = \frac{\mathcal{S}_2}{\mathcal{S}_0} = \frac{I_{x'} - I_{y'}}{I_{x'} + I_{y'}}, \tag{2.22b}$$
$$S_3 = \frac{\mathcal{S}_3}{\mathcal{S}_0} = \frac{I_{\sigma+} - I_{\sigma-}}{I_{\sigma+} + I_{\sigma-}}. \tag{2.22c}$$

The length $|\vec{S}| = \sqrt{S_1^2 + S_2^2 + S_3^2}$ of $\vec{S}$ provides the total polarization degree of the beam. If $|\vec{S}| = 0$, the light is not polarized, while it is completely polarized in the case of $|\vec{S}| = 1$ [24].

2.2.5.1 Relation to Jones vector

The mathematical description of light used in equation (2.18), which is used to calculate the change of polarization during propagation through a medium, is much closer to the Jones vector. For a given z, one can simplify

$$\begin{aligned} &\vec{E}(z,t) = A_1 \vec{E}_1 e^{\mathrm{i}n_1 z/c - \mathrm{i}\omega t} + A_2 \vec{E}_2 e^{\mathrm{i}n_2 z/c - \mathrm{i}\omega t} \\ &\rightarrow \vec{E}(t) = \vec{J} e^{\mathrm{i}\omega t}, \end{aligned} \tag{2.23}$$

where $\vec{J} = (E_x, E_y)$ is the so-called Jones vector, a two dimensional complex vector of the complex electric field amplitudes E_x and E_y [24].

A comparison of the results of an experiment and the calculation is only possible if one can convert Jones into Stokes vectors. The Stokes and Jones vectors of several polarization states are shown in table 2-1. One can calculate the Stokes

State of polarization	Stokes vector	Jones vector
horizontal linear	$\begin{pmatrix} 1 \\ 0 \\ 0 \end{pmatrix}$	$\begin{pmatrix} -1 \\ 0 \end{pmatrix}$.
vertical linear	$\begin{pmatrix} -1 \\ 0 \\ 0 \end{pmatrix}$	$\begin{pmatrix} -0 \\ 1 \end{pmatrix}$.
linear along $+45°$	$\begin{pmatrix} 1 \\ 1 \\ 0 \end{pmatrix}$	$\frac{1}{\sqrt{2}}\begin{pmatrix} -1 \\ 1 \end{pmatrix}$.
linear along $-45°$	$\begin{pmatrix} 0 \\ -1 \\ 0 \end{pmatrix}$	$\frac{1}{\sqrt{2}}\begin{pmatrix} 1 \\ -1 \end{pmatrix}$.
positive circular / right-handed ($\sigma+$)	$\begin{pmatrix} 0 \\ 0 \\ 1 \end{pmatrix}$	$\frac{1}{\sqrt{2}}\begin{pmatrix} 1 \\ -\mathrm{i} \end{pmatrix}$.
negative circular / left-handed ($\sigma-$)	$\begin{pmatrix} 0 \\ 0 \\ -1 \end{pmatrix}$	$\frac{1}{\sqrt{2}}\begin{pmatrix} 1 \\ \mathrm{i} \end{pmatrix}$.

Table 2-1: Stokes and Jones vectors of different polarization states for $|\vec{J}| = 1$.

vector $\vec{S}$ from the complex amplitudes of the Jones vector as [26]

$$S_1 = \frac{|E_x|^2 - |E_y|^2}{|E_x|^2 + |E_y|^2}, \tag{2.24a}$$

$$S_2 = \frac{\Re(E_x E_y^*)}{|E_x|^2 + |E_y|^2}, \tag{2.24b}$$

$$S_3 = \frac{\Im(E_x E_y^*)}{|E_x|^2 + |E_y|^2}. \tag{2.24c}$$

The normalized Stokes vector used as a vector in a Cartesian coordinate system can be used to visualize polarization effects. Since the maximum polarization of light is 1, all the possible polarization states of light are inside a sphere with a radius of 1 around the origin of the Cartesian coordinate system. This sphere is known as the Poincaré sphere.

2.2.6 Optical activity and other polarization effects

A medium is called optically active when the linear polarization of light is continuously rotated while propagating through the medium. It has been firstly observed by the French physicist Dominique F. J. Arago in 1811 in quartz [24]. It can be explained assuming that the linearly polarized light propagates as two circularly polarized waves through the crystal. The electric field of such a wave propagating along $\vec{z}$ according to equation (2.18) and table 2-1 is

$$\vec{E}(z,t) = \underbrace{A_1 \frac{1}{\sqrt{2}} \begin{pmatrix} 1 \\ -\mathrm{i} \end{pmatrix} e^{\mathrm{i}n_1 z/c - \mathrm{i}\omega t}}_{\text{right-handed circularly polarized}} + \underbrace{A_2 \frac{1}{\sqrt{2}} \begin{pmatrix} 1 \\ \mathrm{i} \end{pmatrix} e^{\mathrm{i}n_2 z/c - \mathrm{i}\omega t}}_{\text{left-handed circularly polarized}}. \tag{2.25}$$

If the linear polarization has the angle α relative to $\vec{x}$ at $z = 0$, the amplitudes must satisfy

$$\begin{pmatrix} \cos(\alpha) \\ \sin(\alpha) \end{pmatrix} = A_1 \begin{pmatrix} 1 \\ -\mathrm{i} \end{pmatrix} + A_2 \begin{pmatrix} 1 \\ \mathrm{i} \end{pmatrix}.$$

The complex amplitudes

$$A_1 = \frac{1}{\sqrt{2}} e^{\mathrm{i}\alpha} \qquad \text{and} \qquad A_2 = \frac{1}{\sqrt{2}} e^{-\mathrm{i}\alpha} \tag{2.26}$$

are complex conjugates. The reason for optical activity is circular birefringence. This is a difference in the phase velocities $v_1 = \frac{c}{n_1}$ and $v_2 = \frac{c}{n_2}$ of the two circularly polarized waves. Thus, the two waves accumulate a phase difference $\Delta\varphi = (n_1 - n_2)lz$ by propagating a distance l through the medium. At $z = l$ the electric field is

$$\vec{E}(t) = \frac{1}{2} \left[\begin{pmatrix} 1 \\ -\mathrm{i} \end{pmatrix} e^{\mathrm{i}(\alpha + \Delta\varphi/2)} + \begin{pmatrix} 1 \\ -\mathrm{i} \end{pmatrix} e^{-\mathrm{i}(\alpha + \Delta\varphi/2)} \right] e^{\mathrm{i}(n_1+n_2)/2 \cdot (l/c) - \mathrm{i}\omega t}. \tag{2.27}$$

As the angle of linear polarization defines the phases of the two waves (see equations (2.26) and (2.25) the additional phase difference $\Delta\varphi$ rotates the angle of linear polarization to $\alpha + \Delta\varphi/2$. In quartz, where this effect was firstly discovered, it was due to the crystal structure and did not require an external field to be observed [24]. But if the effect is due to an external magnetic field applied along the direction of propagation (Faraday geometry), the effect is called Faraday rotation.

It is also possible for two linearly polarized waves to propagate at different speeds. This is called linear birefringence. Assuming that these waves are polarized along $\vec{x}$ and $\vec{y}$, the electric field of a positive circularly polarized wave can be written

as

$$\vec{E}(z,t) = \frac{1}{\sqrt{2}} \begin{pmatrix} 1 \\ 0 \end{pmatrix} e^{\mathrm{i}n_1 z/c - \mathrm{i}\omega t} + \frac{-\mathrm{i}}{\sqrt{2}} \begin{pmatrix} 0 \\ 1 \end{pmatrix} e^{\mathrm{i}n_2 z/c - \mathrm{i}\omega t}.$$

Similar to circular birefringence the two linearly polarized waves accumulate a phase difference of $\Delta\varphi$ after propagating through a crystal of thickness l. The electric field at $z = l$ is written as

$$\vec{E}(t) = \frac{1}{\sqrt{2}} \begin{pmatrix} 1 \\ -\mathrm{i}e^{-i\Delta\varphi} \end{pmatrix} e^{\mathrm{i}(n_1+n_2)/2\cdot(l/c) - \mathrm{i}\omega t + \Delta\varphi/2}.$$

When the phase difference is $\Delta\varphi = \frac{\pi}{2}$, the light is purely linear ($S_2 = -1$) polarized. An increase of the phase difference to $\Delta\varphi = \pi$ will change its polarization to negative circularly($S_3 = -1$) polarized, $\Delta\varphi = \frac{3}{2}\pi$ will make it $S_1 = 1$, while $\Delta\varphi = 2\pi$ is again positive circularly polarized ($S_3 = 1$).

While circular birefringence leads to oscillations of the first two normalized Stokes parameters S_1 and S_2, linear birefringence leads to oscillations in S_2 and S_3, when the two linear polarizations with different phase velocity are those of S_1.

The two effects described above are phase-based effects, but there are also absorption-based effects. When two polarizations are absorbed at a different rate while propagating through a medium, the effect is called dichroism. This is expressed by different imaginary parts of the refractive indexes $n_1 = n_1' + \mathrm{i}n_1''$ and $n_2 = n_2' + \mathrm{i}n_2''$. If there are no phase-based effects ($n_1' = n_2' = n'$), one can rewrite equation (2.18) as

$$\vec{E}(z,t) = e^{-\frac{n_1''+n_2''}{2}\cdot z/c} \left(A_1\vec{E}_1 e^{-\frac{n_1''-n_2''}{2}\cdot z/c} + A_2\vec{E}_2 e^{\frac{n_1''-n_2''}{2}\cdot z/c} \right) e^{\mathrm{i}n' z/c - \mathrm{i}\omega t}.$$

The ratio of the intensities I_1 and I_2 of the two polarizations changes while propagating through the crystal according to

$$\frac{I_1}{I_2} = \frac{\mathrm{Abs}(A_1|\vec{E}_1|)^2}{\mathrm{Abs}(A_2|\vec{E}_2|)^2} e^{-2(n_1''-n_2'')\cdot z/c}. \tag{2.28}$$

The ratio changes exponentially until, after propagation over a distance ($z \to \infty$), only one polarization remains.

2.2.7 Excitonic magneto-optical effects

The fundamental exciton doublet can be excited by propagating light. If a magnetic field $\vec{B}$ is applied along $\vec{B} \parallel \vec{k} \parallel [001]$ and the crystal is described by the T_d point group, the doublet of optically active states can be described by a 2x2 effective Hamiltonian $\mathcal{H}$. For an excitation being a mixture of circularly polarized

light (σ^+ and σ^-), the effective Hamiltonian $\mathcal{H}_\sigma$ takes the form

$$\mathcal{H}_\sigma = \begin{pmatrix} \hbar\omega_0 + \frac{\Delta}{2} & Vk_zB_z \\ Vk_zB_z & \hbar\omega_0 - \frac{\Delta}{2} \end{pmatrix}. \tag{2.29}$$

In a basis of light linearly polarized along $\vec{x}$ and $\vec{y}$, the Hamiltonian reads

$$\mathcal{H}_{xy} = \begin{pmatrix} \hbar\omega_0 + VB_zk_z & \frac{\mathrm{i}\Delta}{2} \\ \frac{\mathrm{i}\Delta}{2} & \hbar\omega_0 - VB_zk_z \end{pmatrix}. \tag{2.30}$$

In both Hamiltonians, $\Delta = g_{\mathrm{exc}}\mu_B B_z$ is the exciton Zeeman splitting with g_{exc} being the exciton g-factor,V is the constant responsible for the magneto-spatial dispersion. Diagonalization of $\mathcal{H}_{xy}$ given by

$$\mathcal{H}_{xy} = S \cdot \begin{pmatrix} \hbar\omega_0 + \sqrt{4B_z^2k_z^2V^2 + \Delta} & 0 \\ 0 & \hbar\omega_0 - \sqrt{4B_z^2k_z^2V^2 + \Delta} \end{pmatrix} \cdot S^{-1} \tag{2.31}$$

$$\text{with } S = \begin{pmatrix} \frac{\mathrm{i}\left(2B_zk_zV - \sqrt{4B_z^2k_z^2V^2+\Delta^2}\right)}{\Delta} & \frac{\mathrm{i}\left(2B_zk_zV + \sqrt{4B_z^2k_z^2V^2+\Delta^2}\right)}{\Delta} \\ 1 & 1 \end{pmatrix}$$

reveals two resonances split by

$$\hbar\Omega_{\mathrm{eff}} = 2\sqrt{4B_z^2k_z^2V^2 + \Delta}. \tag{2.32}$$

Starting from equation (2.31) one can calculate the dielectric tensor ε_{ij} for light with the photon energy $\hbar\omega$ according to

$$\varepsilon_{ij} = S \cdot \begin{pmatrix} \varepsilon(\omega, \hbar\omega_0 + \hbar\Omega_{\mathrm{eff}}/2) & 0 \\ 0 & \varepsilon(\omega, \hbar\omega_0 - \hbar\Omega_{\mathrm{eff}}/2) \end{pmatrix} \cdot S^{-1}. \tag{2.33}$$

Here $\varepsilon(\omega, \hbar\omega_{\mathrm{res}})$ is a dielectric function for light with a photon energy $\hbar\omega$ exciting an exciton resonance with the energy of $\hbar\omega_{\mathrm{res}}$. If Ω_{eff} is small enough, ε can be approximated by a first-order Taylor series. This simplifies equation (2.33) to

$$\varepsilon_{ij} = \varepsilon(\omega, \hbar\omega_0) \begin{pmatrix} 1 & 0 \\ 0 & 1 \end{pmatrix} + \left.\frac{d\varepsilon(\omega, \hbar\omega_{\mathrm{res}})}{d\hbar\omega_{\mathrm{res}}}\right|_{\hbar\omega_0} \begin{pmatrix} VB_zk_z & \frac{\mathrm{i}\Delta}{2} \\ \frac{\mathrm{i}\Delta}{2} & -VB_zk_z \end{pmatrix}. \tag{2.34}$$

To calulate the resulting polariton propagation, according to section 2.2.4, $\varepsilon_{\mathrm{dia}}$ and $\varepsilon_{\mathrm{off}}$ are used. If the photon energy is at least a few meV below the exciton resonance energy $\hbar\omega_0$, the simplified model will be sufficient. Using equation (2.11) to calculate the dielectric constant, the contributions to the dielectric tensor are

$$\varepsilon_{\mathrm{off}} = \frac{\varepsilon_0\omega_{LT}}{(\omega_0 - \omega - \mathrm{i}\Gamma/2)^2} \frac{\Delta}{2\hbar B_z} Bz = \mathrm{i}\gamma_1 B_z \text{ and} \tag{2.35a}$$

$$\varepsilon_{\mathrm{dia}} = \frac{\varepsilon_0\omega_{LT}}{(\omega_0 - \omega - \mathrm{i}\Gamma/2)^2} \frac{2Vk_zB_z}{\hbar} = \gamma_2 k_z B_z. \tag{2.35b}$$

Here, ω_{LT} is the longitudinal-transverse splitting, Γ is the dampening, and γ_1 and γ_2 are constant responsible for the Faraday rotation and linear birefringence, respectively. Further, if the exciton resonance is inhomogeneously broadened by Γ_{inh} one can calculate

$$\gamma_1 = \int_{-\infty}^{+\infty} \frac{\varepsilon_0 \omega_{LT}}{\hbar(\omega' - \omega - \mathrm{i}\Gamma/2)^2} \frac{\exp\left[-\frac{(\omega'-\omega_0)^2}{2\Gamma_{\text{inh}}^2}\right]}{\sqrt{2\pi}\Gamma_{\text{inh}}} d\omega' \frac{\Delta}{2B_z} + \gamma_1' \tag{2.36a}$$

$$\gamma_2 = 2\int_{-\infty}^{+\infty} \frac{\varepsilon_0 \omega_{LT}}{\hbar(\omega' - \omega - \mathrm{i}\Gamma/2)^2} \frac{\exp\left[-\frac{(\omega'-\omega_0)^2}{2\Gamma_{\text{inh}}^2}\right]}{\sqrt{2\pi}\Gamma_{\text{inh}}} d\omega' V. \tag{2.36b}$$

If the Zeeman split excitonic resonance is the only source of Faraday rotation, then $\gamma_1' = 0$. But in CdTe there are other sources of Faraday rotation [7]. These contributions are taken into account by γ_1'.

2.2.8 Excitonic polarization effects and group refractive index

There is a very strong dependence between excitonic phase-based polarization effects and the group refractive index. If we describe polarization effects according to equation (2.18), one can easily calculate the phase difference

$$\Delta\varphi = (n_1 - n_2)\frac{\omega}{c} l = \Delta n \frac{\omega}{c} l$$

between the two waves after the propagation through a crystal of thickness l. Assuming that the frequency dependence of n_1 and n_2 is the same except a small shift in frequency Ω_{eff}, one obtains

$$n_1(\omega) = n(\omega + \frac{\Omega_{\text{eff}}}{2}) \text{ and } n_2(\omega) = n(\omega - \frac{\Omega_{\text{eff}}}{2}).$$

Also $n(\omega)$ and $\frac{\partial n}{\partial \omega}$ should be continuous and Ω_{eff} small. In this case, we can use a linear approximation for Δn and get a phase difference of

$$\Delta\varphi = \frac{\partial n}{\partial \omega} \Omega_{\text{eff}} \frac{\omega}{c} l \ . \tag{2.37}$$

The group refractive index is, according to equation (2.6),

$$\begin{aligned} n_G(\omega) &= \frac{\partial}{\partial \omega} \omega n(\omega) \\ \text{or} &= n + \omega \frac{\partial n}{\partial \omega}. \end{aligned} \tag{2.38}$$

If we combine equations (2.37) and (2.38), we can calculate the phase difference as

$$\Delta\varphi \;=\; \underbrace{(n_G - n)\frac{l}{c}}_{\tau}\,\Omega_{\text{eff}}\ . \tag{2.39}$$

It is simply the delay τ introduced by the split resonance multiplied by the splitting of the resonance Ω_{eff}.

2.3 Exciton magnetic polaron formation

The term "polaron" was invented by Pekar to describe correlated states of electrons and lattice vibrations [27]. The usage of the term has been expanded to describe quasi-particles that generate at least part of their formation energy by polarizing the surrounding material.

In diluted magnetic semiconductors there is a strong exchange interaction between the carrier and magnetic ions [28]. This interaction leads to the collective alignment of the spins of the magnetic ions, which can be understood as a form of spatially confined ferromagnetism. This quasi-particle is known as a magnetic polaron.

Magnetic polarons can be divided into bound and free magnetic polarons. In the first case the carrier is bound by Coulumb potential to an impurity. This leads to a decrease of the wavefunctions volume, that is called localization. Examples of bound polarons are electrons bound to donors [29] and holes bound to acceptors [30, 31, 32]. The theory describing this system is detailed and allows an understanding of their main features [33].

Free polarons are not bound to an impurity and carriers are only localized due to the polarization which they create in their environment. A more detailed introduction to free magnetic polarons is given in subsection 2.3.1. A superficial introduction into the theory used to describe them is given in subsection 2.3.2. The conditions under which a free exciton magnetic polaron is stable are explored in subsection 2.3.3. Usually, free magnetic polarons are not stable in bulk material. Investigations of these polarons are easier in systems where the movement of carriers is confined in at least one dimension [34]. Quantum wells, which confine the movement in one dimension, are introduced in subsection 2.3.5.

2.3.1 Exciton magnetic polarons in diluted magnetic semiconductors

Exciton magnetic polarons (EMPs) are magnetic polarons formed by excitons, e.g., in diluted magnetic semiconductors with magnetic Mn^{2+} ions [10]. In diluted magnetic semiconductors carriers are coupled to the spin of the magnetic ions by sp-d exchange interaction [28]. Due to this exchange interaction the energy of an exciton can be changed by aligning the manganese (Mn) spins. One example is the giant Zeeman splitting, which is the splitting of the exciton states with different spin due to the application of an external magnetic field. For a heavy hole exciton the energy splitting ΔE_z can be described by the modified Brillouin function [10]

$$\Delta E_z = (\alpha - \beta) N_0 x S_{\text{eff}} B_{\frac{5}{2}} \left[\frac{5 \mu_B g_{Mn} B}{2 k_B (T + T_0)} \right], \tag{2.40}$$

where x is the concentration of Mn, while $N_0\alpha$ and $N_0\beta$ are the exchange integrals of the conduction- and valence-band. With increasing concentration Mn forms antiferromagnetically coupled clusters. The effective spin S_{eff} and effective temperature T_0 permit a a phenomenological description of their contribution to the Zeeman splitting.

Since the energy of the exciton can be reduced due to the alignment of Mn spins, formation of an EMP is an energetically favorable process. An EMP can be formed during the lifetime of an exciton and can be divided into two phases [33]. In the so-called fluctuation phase the exciton spin aligns along the fluctuation field reducing the energy of the exciton. This field is the average field created by the randomly aligned Mn spins inside the volume of the exciton wavefunction. Since the orientation of the exciton spin is kept stable by the fluctuation field, the exciton can align the Mn spins collectively, which also reduces the exciton energy. This phase is called the collective phase, and would not be able without the fluctuation field. Without it the exciton spin fluctuation would be faster than the response of the Mn spins [10]. The collective phase approaches an equilibrium state where all the Mn spins are collectively aligned leading to the exciton energy being fixed.

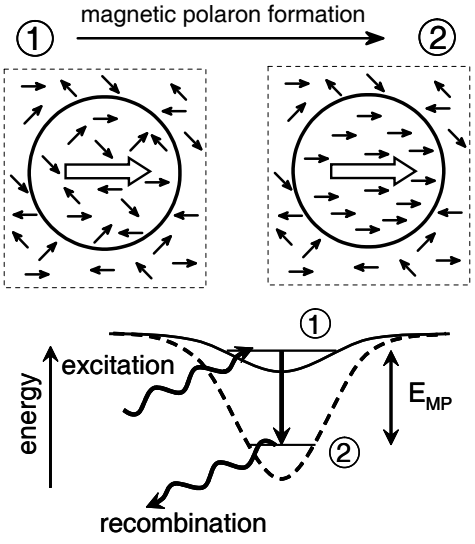

Figure 2-6: Schematic presentation of the formation of an exciton magnetic polaron. The exciton spin is represented by the big arrow while the Mn spins are shown as small arrows. Taken from Ref. [10].

Fig. 2-6 illustrates the formation of an exciton magnetic polaron. There is a popular theoretical prediction [10, 34], that during the collective regime the exciton can localize itself. By aligning the Mn spins the exciton creates a three-dimensional potential well. The potential well compresses the wavefunction leading to a higher density $|\Psi(r)|^2$ of the carrier wavefunction $\Psi(r)$. This in turn allows a stronger alignment of the Mn spins, which produces a deeper potential well. These two processes amplify each other, but are limited since the Mn spins can

be completely aligned. This behaviour is know as autolocalization and leads to an increase in the formation time of the polaron.

If an external magnetic field is applied, the Mn spins will be aligned. Since the polaron generates its energy by aligning these spins, an external field leads to the reduction of the polaron energy and to the suppression of its formation.

2.3.2 Introduction into the theory of the magnetic polaron

In this chapter the most fundamental points of the theory of exciton magnetic polarons are introduced. A more comprehensive view can be found in different publications [33, 35, 36]. After an exciton is formed its spin is aligned parallel to the magnetic moment generated by the fluctuations of the randomly aligned Mn spins. If the exciton wavefunction is in contact with N Mn spins, their magnetic moment produced is $\propto \sqrt{N}$ [10]†. The polaron gains energy and the exciton energy is reduced as its spin aligns along the fluctuation magnetic moment. During the collective phase the carrier spin is aligned along the collective magnetic moment. Since all Mn spins contribute, this magnetic moment is $\propto N$ [10]. Usually about $N = 100$ Mn spins contribute to an exciton magnetic polaron [10]. This leads to a collective magnetic moment which is about 10 times bigger than the fluctuation magnetic moment. As a result, the collective phase is dominant, unless the exciton decays before it aligns the Mn spin collectively. Temperature suppresses the collective phase, if the thermal energy $k_{\mathrm{B}}T$ exceeds the energy won by the alignment of a Mn spin. In this case, the exciton magnetic polaron energy is defined by the fluctuation phase.

In the most general case the magnetic polaron can be described by the following Hamiltonian [10]:

$$H_{\mathrm{MP}} \quad = \quad [K + U(\vec{r})] + [H_{\mathrm{dd}} + H_{\mathrm{mag}}] + H_{\mathrm{ex}}.$$

Here, K is the kinetic energy and $U(\vec{r})$ accounts for all static potentials including the Coulomb potentials of impurities and the influence of the fluctuating quantum well width. $[H_{\mathrm{dd}} + H_{\mathrm{mag}}]$ is the Hamilton-operator of the spin of the localized magnetic ions, where H_{dd} accounts for the interaction between the spins of the magnetic ions and H_{mag} accounts for the interaction with an external magnetic field. The interaction between carrier and localized ion is described by the Hamiltonian H_{ex}.

A more specific Hamiltonian is used for autolocalized magnetic polarons [10]:

$$H_{\mathrm{MP}} = K(r_{\mathrm{loc,t}}) + U(\vec{r}) + V_{\mathrm{ex}}(\Psi^2(r_{\mathrm{loc}}, t), t) \tag{2.41}$$

†The spins are randomly aligned. The expectation value for a measurement of their orientation is 0, but the expected experimental error would be $\propto \sqrt{N}$.

Here $V_{\mathrm{ex}}(\Psi^2(r_{\mathrm{loc}},t),t)$ accounts for the interaction between localized spins and the carrier. It depends on the carrier's wavefunction and it's localization radius, which is usually assumed to be proportional to a local magnetization. This can be expressed by an exchange field $B_{\mathrm{ex}}(\vec{r})$ [10, 34] . For an exciton forming a magnetic polaron with Mn^{2+} ions, one neglects the electron contribution [10]. In this case, the exchange field reads [10]

$$B_{\mathrm{ex}} = \frac{1}{3\mu_{\mathrm{B}} g_{\mathrm{Mn}}} \beta J |\Psi(\vec{r})|^2 \ . \tag{2.42}$$

Here β is the hole exchange constant, $\Psi(\vec{r})$ the carrier's wavefunction and $g_{\mathrm{Mn}} \approx 2$ the g-factor of the Mn^{2+} ions. The resulting Schrödinger equation (2.41) is non-linear as the Hamiltonian depends on the wavefunction.

This Schrödinger equation, even using the assumption that the magnetization is linear to B_{ex}, has only been solved exactly for the one dimensional case. To find solutions for other systems, calculus of variations is employed [37, 38], where a functional is minimized and it is assumed that the system will adopt a state corresponding to the minimized functional. One can show that the minimized functional is the free energy for constant temperature [39]. This makes it possible to understand a free magnetic polaron as a thermodynamic system.

2.3.3 Temperature dependence for systems of different dimensions

It is possible to study the formation of an exciton magnetic polaron using thermodynamics. The functional to be minimized to find a stable state is the free energy [39]

$$F = \Delta K(r_{\mathrm{loc}}) + F_{\mathrm{M}}(r_{\mathrm{loc}}, T) \ , \tag{2.43}$$

where ΔK is the energy gained by autolocalization and F_{M} is the free energy of the magnetic ions in the carrier exchange field. Both depend on the localization radius r_0 [34], while the free energy also depends on the temperature T.

Without the presence of an external magnetic field it is written as

$$F_{\mathrm{M}} = \sum_i -k_{\mathrm{B}} T \ln(Z_i),$$

where k_{B} is the Boltzman constant and Z_i the sum over the states of the magnetic ion i, which reads [34]

$$Z_i = \frac{1}{2s+1} \sum_{m=-s}^{s} \exp\left(\frac{mJ\beta|\Psi(r_i)|^2}{k_{\mathrm{B}}T}\right).$$

In this equation s and J are the spins of the magnetic ions and the carrier while β is the hole exchange constant and $|\Psi(r_\mathrm{i})|^2$ is the probability density of the carrier at the ion i. In a continuum approximation the free energy of the ions is

$$F_\mathrm{M} = -k_\mathrm{B}T \int \mathrm{d}^3r \ \ln\left[\frac{1}{2s+1}\cdot\sum_{m=-s}^{s}\exp\left(\frac{mJ\beta|\Psi(r_i)|^2}{k_\mathrm{B}T}\right)\right]. \qquad (2.44)$$

Assuming that the carrier is confined in a volume V, where its probability density is constant, it is useful to introduce a variational parameter $\alpha_\mathrm{d} \propto \frac{1}{VT}$. This leads to

$$F_\mathrm{M}(r_\mathrm{loc}, T) = \tilde{F}(\alpha) \propto \alpha_\mathrm{d} \qquad (2.45)$$

for the ion free energy. In contrast, ΔK strongly depends on the dimension d. This can be expressed as [34]

$$\Delta K = \frac{\hbar}{2mr_\mathrm{loc}^2}k \propto (\alpha_\mathrm{d}T)^{2/d}. \qquad (2.46)$$

The dependences of the magnetic ion's free energy and the energy won by autolocalization on a_d are shown in figure 2-7(a). The dependence of the magnetic

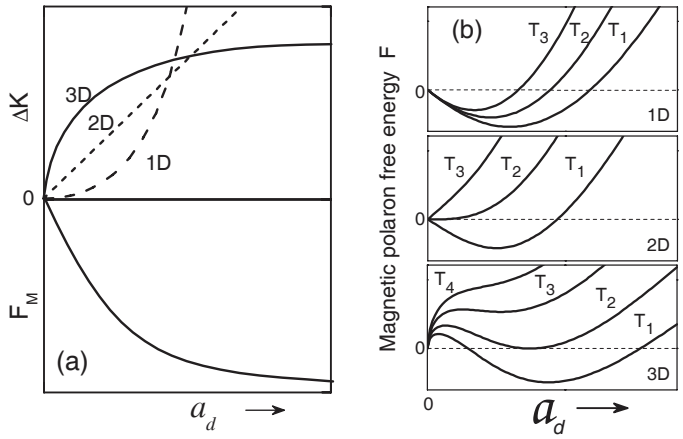

Figure 2-7: (a): Dependences of the kinetic energy gained due to autolocalization ΔK and the free energy of the mangetic ions F_MP on $\alpha_\mathrm{d} \propto \frac{1}{r_\mathrm{loc}^d T}$. (b): Free energies for one-, two- and three-dimensional systems for three difffrent temperatures $T_1 < T_2 < T_3 < T_4$ in dependence on α_d. Taken from Ref. [10].

polaron free energy on α_d is shown in figure 2-7(b) for three different temperatures. Several conclusions arise from these dependences. In contrast to two- and three-dimensional systems, the minima of the magnetic polaron free energy is at $\alpha_\mathrm{d} > 0$ for all considered temperatures. This makes magnetic polaron formation energetically favourable. For two- or three-dimensional systems there is a critical temperature T_c, where the most favorable state is $\alpha_\mathrm{d} = 0; r_\mathrm{loc} \to \infty$. In this case, there is no polaron formation. In three-dimensional systems the formation of a

magnetic polaron is hindered by an initial barrier. According to equation (2.44), the stability of the system depends on the exchange integrals, the effective mass of the carrier and the temperature.

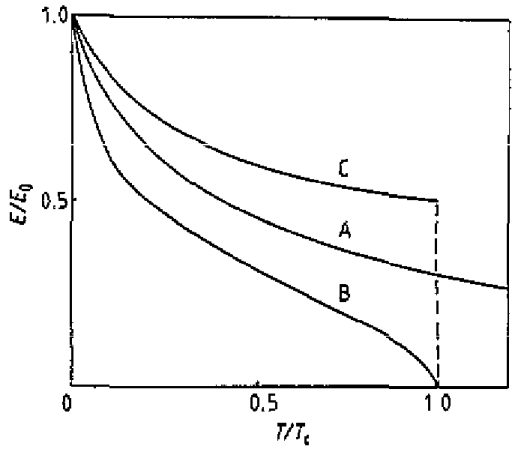

Figure 2-8: Dependence of the relative polaron energy $\frac{E}{E_0}$ on the relative temperature $\frac{T}{T_c}$ for one-dimensional systems (curve A), two-dimensional systems (curve B) and three-dimensional systems (curve C). Taken from Ref.[34].

Typical temperature dependences are shown in figure 2-8. The curve labelled 'B' refers to quantum wells. For a quantum well the polaron energy reaches 0 at a critical temperature T_c. This is the behaviour shown in figure 2-7(b), where the free energy increase for α_d and the carrier localization decreases with temperature.

Theoretical calculations for $CdTe/Cd_{0.75}Mn_{0.25}Te$ quantum wells predict a critical temperature of $T_c \approx 1.6\,K$ [34, 10]. This is in contrast to empiric values, as it is possible to observe exciton magnetic polaron formation for temperatures in excess of 20 K [11]. This difference can be explained by fluctuations of the quantum well width compressing the exciton wavefunction and enabling the magnetic polaron formation. The localization radius changes during the polaron formation. A particle of this nature is called a quasi-free polaron.

2.3.4 Indirect prediction of polaron energy

There is a relationship between the polaron energy, the magnetic exchange field of the polaron, the magnetic moment of the equilibrium state and the magnetic moment during the fluctuation phase which can be used to predict the polaron energy. In II-VI semiconductors, the presence of Mn^{2+} ions leads to the giant Zeeman splitting for excitons. According to equation (2.40), it can be described by a modified Brillouin function, which depends on the exchange integrals of the conduction- and valence-band, $N_0\alpha$ and $N_0\beta$. Since most of the splitting is due to the heavy hole, one can neglect the contributions of the electron. The Zeeman

splitting for the heavy hole reads

$$\Delta E_{\mathrm{z}}^{\mathrm{hh}} = \frac{|\beta|}{|\alpha|+|\beta|}\Delta E_{\mathrm{z}}(B). \tag{2.47}$$

Further simplification is possible if the linear approximation

$$\Delta E_{\mathrm{z}}^{\mathrm{hh}}(B) = \left.\frac{dE_{\mathrm{z}}^{\mathrm{hh}}}{dB}\right|_{B=0} B = \gamma B \tag{2.48}$$

is used, with γ being the slope of the Zeeman splitting for small magnetic fields. In this case, the alignment of the magnetic moment of the polaron $M_{\mathrm{MP}}(B_{\mathrm{ex}})$ along the exchange field yields the following energy [35]:

$$\begin{aligned} \frac{1}{2}\Delta E_{\mathrm{z}}^{\mathrm{hh}} &= B_{\mathrm{ex}} \cdot M_{\mathrm{MP}}(B_{\mathrm{ex}}) \\ \Rightarrow \frac{1}{2}\frac{d\Delta E_{\mathrm{z}}^{\mathrm{hh}}}{dM_{\mathrm{MP}}(B_{\mathrm{ex}})} &= B_{\mathrm{ex}} = \frac{1}{2}\frac{d\Delta E_{\mathrm{z}}^{\mathrm{hh}}}{dB}\frac{dB}{dM_{\mathrm{MP}}(B_{\mathrm{ex}})} \end{aligned} \tag{2.49}$$

Using the equation (2.48) the energy of the magnetic polaron is $E_{\mathrm{MP}} = \frac{1}{2}\frac{d\Delta E_{\mathrm{z}}^{\mathrm{hh}}}{dB}B_{\mathrm{ex}}$, leading to

$$E_{\mathrm{MP}} = \left(\frac{1}{2}\frac{d\Delta E_{\mathrm{z}}^{\mathrm{hh}}}{dB}\right)^2 \cdot \left(\frac{dB}{dM_{\mathrm{MP}}(B_{\mathrm{ex}})}\right). \tag{2.50}$$

One can approximate the magnetic moment of the collective phase M_{MP} as [35]

$$M_{\mathrm{MP}}(B) = \frac{< M_{\mathrm{f}}^2 >}{k_{\mathrm{B}}T}B. \tag{2.51}$$

The magnetic moment of the fluctuation phase M_f determines the gradient $\frac{d\rho}{dB}\big|_{B=0T}$ of the magnetic field dependence of the photoluminescence polarization $\rho(B)$ at $B = 0\,\mathrm{T}$ [35]. From this the magnetic polaron energy can be obtained using the following calculations:

$$\rho(B) \approx \frac{\sqrt{2 < M_{\mathrm{f}}^2 >}}{\sqrt{\pi}k_{\mathrm{b}}T}B \tag{2.52}$$

$$\left.\frac{d\rho}{dB}\right|_{B=0T} = \frac{\sqrt{2 < M_{\mathrm{f}}^2 >}}{\sqrt{\pi}k_{\mathrm{b}}T}$$

$$\Rightarrow (2.51) \Rightarrow \frac{dM_{\mathrm{MP}}(B_{\mathrm{ex}})}{dB} = \frac{\pi k_{\mathrm{B}}T}{2}\left[\left.\frac{d\rho}{dB}\right|_{B=0T}\right]^2 \tag{2.53}$$

$$\Rightarrow (2.50) \Rightarrow E_{\mathrm{MP}} = \frac{1}{2\pi k_{\mathrm{B}}T}\left(\frac{\gamma}{\Theta}\right)^2, \tag{2.54}$$

$$\text{where } \Theta = \left.\frac{d\rho}{dB}\right|_{B=0T}.$$

The possibility to predict the polaron energy from continuous wave measurements is useful if the exciton decays before the polaron is fully formed.

2.3.5 Quantum wells

Molecular beam epitaxy has enabled the growth of layers with a thickness of single atoms of different composition onto another. This opens the possibility to produce different structures which demonstrate quantum mechanical phenomena. One of these structures is a quantum well.

This structure confines the movement of excitons in one dimension by a one dimensional potential well. The quantum well is a layer with a thickness less than the exciton Bohr radius surrounded by a different material with a bigger band gap than the quantum well. The surrounding material is called barrier material. A schematic illustration of a structure is shown in figure 2-9.

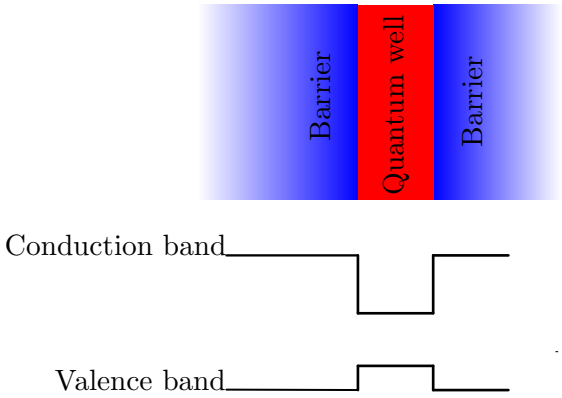

Figure 2-9: Schematic illustration of a quantum well and the related band gaps.

2.3.5.1 Idealized potential well

It is possible to determine the influence of a quantum well (QW) on an electron by a simple quantum mechanical model. The model assumes that the electron can propagate freely in $\vec{x}$- and $\vec{y}$-direction, but an infinitely deep potential well of thickness L centered around $z = 0$ confines the movement in $\vec{z}$-direction. This system can be described by the Hamiltonian

$$\begin{aligned} H &= \frac{p^2}{2m^*} + V(z) \\ V(z) &= -\infty \text{ for } z \geq \frac{L}{2} \\ V(z) &= V_0 \text{ for } z < \frac{L}{2}. \end{aligned}$$

Most likely the effective mass of the electron m^*_{A} in the quantum well material will not be the same as in the material of the barrier m^*_{B}. To take this into account one has to generalize the continuity conditions[‡] leading to

$$\frac{1}{m^*_{\mathrm{A}}} \cdot \frac{d\psi_{\mathrm{A}}}{dz} = \frac{1}{m^*_{\mathrm{B}}} \cdot \frac{d\psi_{\mathrm{B}}}{dz}, \tag{2.55}$$

where ψ_{A} and ψ_{B} are the wavefunctions inside the quantum well and the barrier. Because the potential well is infinitely deep the electron wavefunction will not penetrate into the barrier material. Under this condition equation (2.55) leads to the following electron energies:

$$E_n = \underbrace{\frac{\hbar^2}{2m^*_{\mathrm{A}}} \left(\frac{n\pi}{L}\right)^2}_{\text{Confinement energy}} + \frac{\hbar^2}{2m^*_{\mathrm{A}}} \left(k_x^2 + k_y^2\right). \tag{2.56}$$

There are several possible states n, but only the ground state $n = 1$ will be studied in the scope of this work. In this state the confinement increases the energy of the electron by $\frac{\hbar^2}{2m^*_{\mathrm{A}}} \left(\frac{n\pi}{L}\right)^2$.

2.3.5.2 Real semiconductor quantum wells

In real quantum wells the potential well is of finite depth. The energy difference between barrier and QW is known as band offset. As a result, the wavefunction penetrates into the barrier material. With decreasing thickness L and band offset the part of the wavefunction inside the barrier increases.

Quantum wells can also confine holes, vacancies in the the valence-band. The potential confining their wavefunction is known as the valence-band offset. The energy of a band is usually given for an electron. Since a hole has a positive charge, the valence-band of the material of the quantum well needs to be of higher energy than the barrier to confine a hole. Due to the sign of the valence-band offset, there are two types of quantum wells:

- Type I: Both, the electron and the hole are confined inside the quantum well.
- Type II: At least one particle is confined, but the material that is energetically favorable for one particle is not energetically favorable for the other one.

Another property of real quantum wells are imperfections created during the growth of the quantum well. The thickness of a quantum well can vary. According

[‡]Derived from the time invariant Schroedinger-Equation

to equation (2.56) this will lead to fluctuations of the energy of the confined particles. Also the composition of the quantum well can vary leading to fluctuations in the conduction- and valence- band offsets. Further, a quantum well may contain impurities, which can attract either electrons or holes. Because of imperfections, there are energetically favourable places inside the quantum well. These attract carriers, either electrons or holes, which , after emitting their excess energies as phonons, will be localized in these places. This process is known as non-magnetic localization.

Chapter 3

Measuring sub-nanosecond dynamics

Most of the measurements presented in this work were performed with either a time-of-flight setup or time-resolved photoluminescence setup. Both setups allow for studying sub-nanosecond dynamics. The main purpose of a time-of-flight setup is to determine the time necessary for light to propagate through a sample. Usually a time-resolved photoluminescence setup is used to determine the lifetime of an excited state emitting photoluminescence (PL). Both setups were modified to expand their capabilities, e.g. by applying strong external magnetic fields to the sample. The principle configuration of the time-of-flight setup is presented in section 3.1, while the time-resolved PL setup is presented in section 3.2.

3.1 Time-of-flight setup

To measure the delay introduced by a sample one creates a laser pulse, sends it through a sample and compares the time of arrival at a detector behind the sample to the time of arrival for the identical path but without the sample. The setup required to conduct this measurement is known as a time-of-flight setup and is schematically shown in Fig. 3-1. It can be divided into three parts. The excitation creating the laser pulse, the sample and the devices necessary to keep it in a certain state and the detection analysing the transmitted pulse. In Fig. 3-1 the parts belonging to the excitation are coloured green and the path of the pulse is indicated by a red line. The laser pulse is created in a mode-locked Ti:Sapphire laser. This laser produces a pulse every 13.2 ns which corresponds to a repetition rate of 75.75 MHz. The power of the laser pulses is then reduced, and their polarization is set by passing through a Glan-Thompson prism and then a retarder plate. The retarder plate is either a $\lambda/2$, if the exciting light should be linearly polarized, or a $\lambda/4$, which is used to create circularly polarized light.

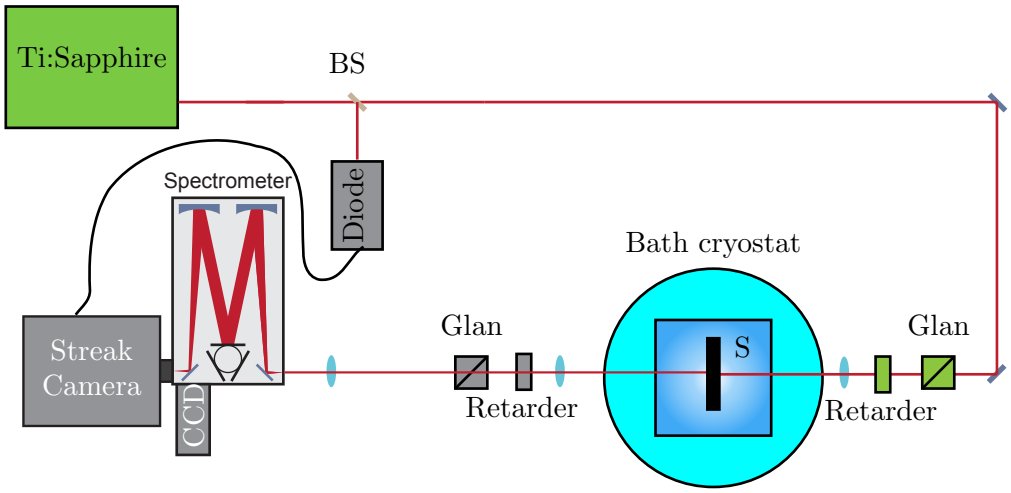

Figure 3-1: Schematic presentation of a time-of-flight setup. The polarization of the laser pulse created by the Ti:Sapphire laser is set by the Glan-Thompson (Glan) prism and a retarder plate (Retarder). The laser beam is then focused on the sample (S), which is kept inside a split coil bath cryostat. The light transmitted through the sample is collected by a lens, a retarder plate and a Glan-Thompson prism are used to select a single polarization. The temporal and spectral composition of this light is analysed by the combination of a spectrometer and a streak camera.

The light is then focused on the sample using a lens. The sample is kept inside a bath cryostat, where it is submerged in superfluid helium, which is kept at a temperature of $T = 1.8\,\mathrm{K}$. Because superfluid helium is an efficient coolant [40] and the excitation power is low ($100\,\mu\mathrm{W}$-$2\,\mathrm{mW}$), the sample has the same temperature as the helium. The cryostat can also produce a magnetic field of up to $B = 10\,\mathrm{T}$ in the direction of the laser propagation. This magnetic field is created by superconductive split coils.

The light leaving the sample on the side opposing the excitation is collected for detection into a beam by a second lens. A specific polarization of the light is selected by passing the beam through a retarder plate and a Glan-Thompson prism. It is then focused onto the vertical entrance slit of a 500 mm spectrometer. The different spectral components are spatially separated in the horizontal plane by a grating with $300\frac{\mathrm{grooves}}{\mathrm{mm}}$. As a next step, the resulting light is focused on the horizontal entrance slit of a streak camera. The streak camera is synchronized to the laser using a fast optical diode. For this purpose, a part of the laser beam is split from the main beam by a beam splitter (BS) and is focused on the diode. The different temporal components of the beam of light are spatially separated in the vertical direction by the streak camera. At the end of the streak camera the spatial intensity distribution is measured by a two-dimensional charge-coupled device(CCD). The vertical position of a pixel in the array corresponds to the time of arrival of the detected light, while the horizontal position determines the energy. The temporal resolution of the setup is 20 ps, while the spectral resolution is 1 meV.

3.2 Time-resolved photoluminescence

A time-resolved PL setup shares several components with a time-of-flight setup. It can also be divided into three parts and its schematic representation is shown in Fig. 3-2. The exciting laser pulse is created by a mode-locked Ti:Sapphire laser.

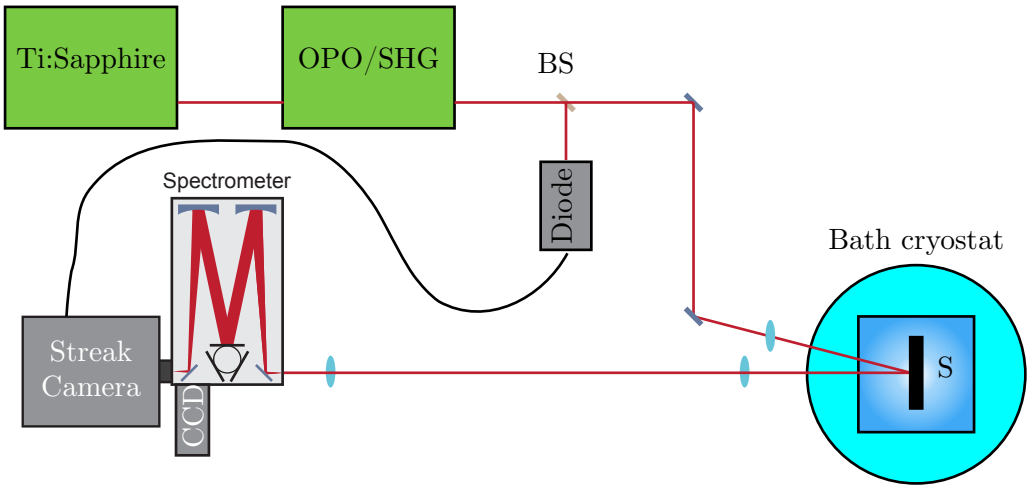

Figure 3-2: The sample (S) is kept inside a split coil bath cryostat, and is excited by a laser pulse created by a Ti:Sapphire laser and an optical parametric oscillator (OPO) in combination with a second harmonic generation crystal (SHG). The emitted PL is collected and the spectral and temporal composition analyzed by a combination of a spectrometer and a streak camera.

Since the energy of the light is too low to be absorbed, an optical parametric oscillator in combination with a second harmonic generating crystal is used to increase the photon energy of the light. Before being focused onto the sample, the power of the resulting laser beam is adjusted resulting in a power density of $P \leq 1\,\mathrm{W\,cm^{-2}}$.

The sample is kept inside a bath cryostat and is submerged in superfluid helium with a temperature of $T = 1.8\,\mathrm{K} - 2\,\mathrm{K}$. The cryostat is able to produce a strong magnetic field of up to $B = 7\,\mathrm{T}$ using superconductive split coils. By rotating the cryostat one can choose, if the magnetic field is applied in Faraday or Voigt geometry*.

The emitted PL is collected by a lens and then focused onto a spectrometer where its spectral components are resolved by a grating with $300\frac{\mathrm{grooves}}{\mathrm{mm}}$. The temporal resolution is achieved using a streak camera. The resolution of this setup is 33 ps and 2 meV. In time-integrated measurements the spectrally resolved light is focused onto a liquid nitrogen cooled CCD camera.

*In Faraday geometry the magnetic field is applied parallel to the direction of propagation of the collected PL, while it is applied orthogonal to the direction of propagation of the collected PL in Voigt geometry.

Chapter 4

Polariton propagation in (Cd,Zn)Te

The experimental work on exciton polaritons is presented in three sections. First the basic properties of the exciton polariton are determined in section 4.1. Polaritons are propagating states. The dynamics and the type of propagation in the absence of an external magnetic field are studied in section 4.2. The application of an external magnetic field results in the appearance of several polarization effects. They are identified and characterized in section 4.3. Conclusions from the experimental work are drawn in section 4.4.

4.1 Optical properties of exciton polariton

In this section the exciton polariton (EP) of the fundamental exciton will be characterized. The photoluminescence (PL) spectrum of the EP is studied in subsection 4.1.1 together with the recombination dynamics of the EP. In the next two subsection the properties of exciton resonance relevant for EP propagation are determined. In subsection 4.1.2 reflection spectra are used to determine the exciton resonance energy $\hbar\omega_0$ and the inhomogeneous broadening Γ_{inh}. The homogeneous broadening Γ is deduced from transmission measurements in subsection 4.1.3. Since the longitudinal-transverse splitting ω_{LT}, the background dielectric constant ε_0 and the effective mass M are known from literature, the exciton is then fully characterized. In subsection 4.1.4 the influence of an external magnetic field on the resonance energy and the PL spectra is studied.

The studied samples were part of a bulk $Cd_{0.88}Zn_{0.12}Te$ crystal, that was grown by the Bridgman technique at a high temperature of $T = 1200\,^{\circ}\mathrm{C}$ [41]. The crystal was not intentionally doped, resulting in a slight p-doping with a concentration on the order of $10^{15}\mathrm{cm}^{-3}$ due to limitations in the growth process. The crystal was cut along the (100) plane and divided into several samples. After chemically-mechanically polishing they had a good surface quality as evident by the low etched pits density of 10^4 cm^{-2} and a rocking curve of less than 20 arcseconds.

The samples are between 208 µm and 745 µm thick.

4.1.1 Photoluminescence

Fig. 4-1(a) shows the PLspectrum taken from the $Cd_{0.88}Zn_{0.12}Te$ crystal at $T = 1.8\,K$ using high-energetic excitation(2.33 eV). The spectrum consists of 4 main peaks. One narrow peak at 1.6643 eV and a broader one at 1.657 eV and their

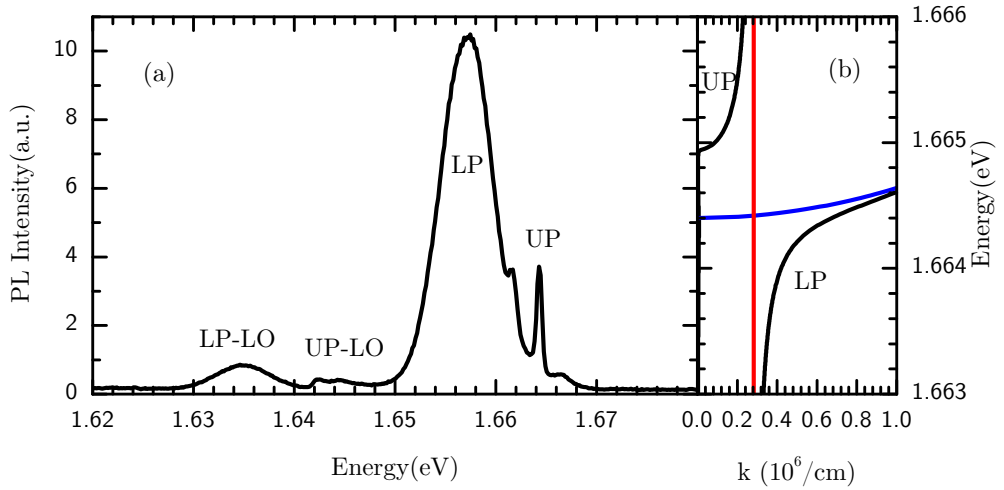

Figure 4-1: (a) PLspectrum excited by non-resonant continuous-wave excitation with a photon energy of 2.33 eV, the sample was kept at $T = 1.8\,K$. No magnetic field was applied. (b) Typical EP dispersion in bulk crystal is shown as black lines, red and blue lines represent the dispersions of light and the exciton, respectively.

optical phonon replicas. The narrow one is associated with the bottom of the upper polariton(UP) branch, while the broader one is due to emission from the lower polariton(LP) branch.

When polaritons relax in energy by emitting phonons they accumulate at the bottom of the UP branch. A typical EP dispersion is shown in Fig. 4-1(b). It is shallow at the UP bottom resulting in a narrow linewidth of the emitted PL. From the bottom of the UP branch a polariton can relax into the LP branch. Also, it can relax further within the LP branch. The gradient of the LP dispersion increases with decreasing polariton energy. As the group velocity is given by the gradient, a reduction of polariton energy will result in an increase of propagation speed. When the polariton reaches the surface it can be converted into a photon and leave the sample. Since this energy is affected by the continuous relaxation, the PL line is spectrally wide.

Polaritons of both branches can emit longitudinal optical (LO) phonons [42]. Accordingly their energies are reduced by that of an LO phonon $\hbar\omega_{LO} = 22\,meV$. Due to the strong slope of the LP dispersion at lower energies the polaritons propagation to the surface is fast after emission of an LO phonon. The two weak

peaks around 1.64 eV are replica due to this relaxation mechanism.

To confirm this relaxation path time-resolved PL was used. Fig. 4-2 shows PL measured under pulsed excitation with a photon energy of $\hbar\omega_{\mathrm{exc}} = 1.673\,\mathrm{eV}$.

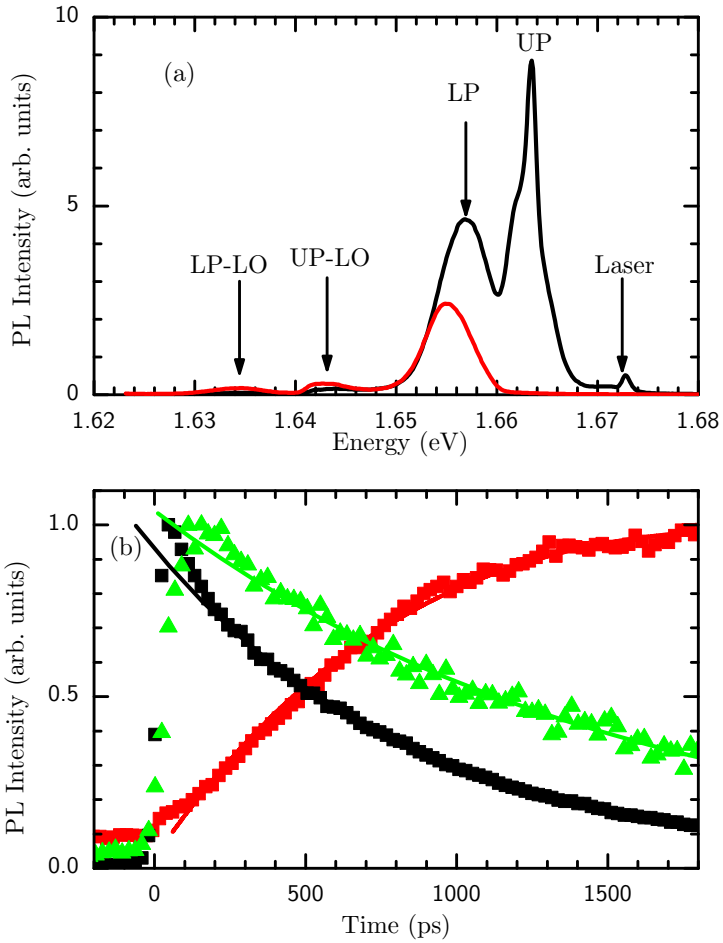

Figure 4-2: PLexcited by a laser pulse of 1 ps duration at 8 K without a magnetic field. (a): Time integrated spectra measured in reflection geometry(black line) and transmission geometry(red line). (b): Intensity transients for UP(black boxes), UP-LO(green triangles) and LP(red dots).The lines are exponential curves fitted to the data.

Both time-integrated PL spectra shown in Fig. 4-2(a) are useful for understanding the origin of the PL . The spectrum represented by the black line in Fig. 4-2(a) was acquired in reflection geometry, where the excitation was focused on the spot from which the PL was collected (detection spot). The red line represents a spectrum acquired in transmission geometry, where the PL was collected from the back side of the crystal. The first spectrum is similar to the spectrum taken under high-energy excitation shown in Fig. 4-1, but the stray light from the laser and the UP peak are much stronger. The second spectrum differs from the first. Here the LO phonon replicas are more pronounced, while the LP is shifted to lower energies, the UP and Laser peak are missing. This difference is due to the spec-

tral dependence of the transparency. As demonstrated in chapter 4.1.3, when the photon energy approaches the exciton resonance the transparency decreases until there is no propagation through the crystal. From this one can deduce that the UP peak is due to emission from polariton at the surface. The polaritons inside the crystal do not contribute to this peak, as they get absorbed before they can propagate to the surface where they could be emitted as a photon. In contrast the UP-LO peak has significant contributions from polaritons inside the crystal.

The PL intensity dynamics for the first two nanoseconds after excitation of the LP(red dots), UP-LO(green triangles) and UP lines(black squares) are shown in Fig. 4-2(b). The phonon replica of the UP decays with a time constant of 1540 ps while the UP PL decays which a time constant of 877 ps. This difference is a result of the UP peak being PL from polaritons at the surface of the crystal. At the surface the polariton population reduces faster, because a polariton can escape the sample by exciting a photon outside the sample.

Assuming, that the creation of an LP is the main relaxation path for UP inside the crystal, the populations n_{UP} and n_{LP} can be described by rate equations

$$\frac{dn_{\mathrm{UP}}(t)}{dt} = -\frac{n_{\mathrm{UP}}}{\tau_{\mathrm{f}}} \qquad \frac{dn_{\mathrm{LP}}(t)}{dt} = \frac{n_{\mathrm{UP}}}{\tau_{\mathrm{f}}} - \frac{n_{\mathrm{LP}}}{\tau_{\mathrm{d}}},$$

where is the τ_{f} is the time constant for the relaxation for from UP to LP and τ_{d} is the time constant for the decay leading to PL . If the starting population is n_{s} in the UP and 0 in the LP the UP and LP population

$$n_{\mathrm{UP}} = n_{\mathrm{s}} e^{-\frac{t}{\tau_{\mathrm{f}}}} \qquad n_{\mathrm{LP}} = \frac{\left(e^{-\frac{t}{\tau_{\mathrm{d}}}} - e^{-\frac{t}{\tau_{\mathrm{f}}}}\right) n_{\mathrm{s}} \tau_{\mathrm{d}}}{\tau_{\mathrm{d}} - \tau_{\mathrm{f}}} \tag{4.1}$$

are related, since τ_{f} is the lifetime of the UP branch and the risetime of the LP.

The LP luminescence has a rise time determined by fitting the data in 4-2(b) and is comparable to the decay time of the UP. This confirms that the UP feeds the LP branch. Furthermore, the LP branch has a lifetime of about 3 ns.

4.1.2 Reflection

At the interface between two media with different refractive indices n_1 and n_2 light can be reflected. The reflection is usually calculated using the Fresnel equations [43]. The ratio between the reflected intensity I_{R} and incident intensity I_0 is named the reflection coefficient R. Assuming that the light arrives at the surface at a normal incidence R is given by [43]:

$$R = \frac{I_{\mathrm{R}}}{I_0} \qquad R = \left|\frac{n_1 - n_2}{n_1 + n_2}\right|^2 \tag{4.2}$$

Since the refractive index for light with an energy close to a exciton resonance is influenced by the exciton according to equations (2.5) and (2.8), reflection spectra can be used to characterize excitons.

A reflection spectrum measured at a temperature of $T = 1.8\,\mathrm{K}$ is shown in Fig. 4-3 as black circles. A reflection spectrum calculated with the Fresnel equations (4.2) is also shown in this figure as the green line. In the experiment the sample is surrounded by liquid helium. When calculating the reflection spectra it was assumed that the helium refractive index is $n_1 = 1$. The second medium is the sample, its refractive index $n_2 = \sqrt{\varepsilon}$ is calculated from the dielectric function of an inhomogeneously broadened ($\Gamma_{\mathrm{inh}} = 1\,\mathrm{meV}$) and damped ($\Gamma = 8\,\mu\mathrm{eV}$) exciton with a resonance energy of $\hbar\omega_0 = 1.6644\,\mathrm{eV}$ and with spatial dispersion ($M = 1.5m_0$). This dielectric function was calculated numerically by the algorithm presented in appendix 8.1.

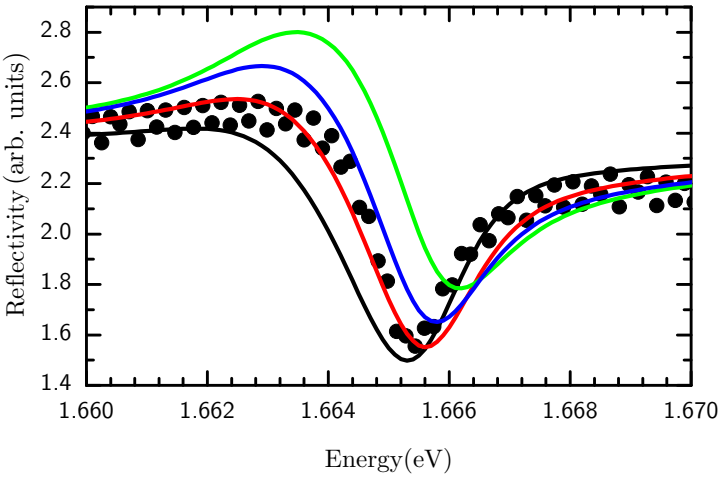

Figure 4-3: Black dots: Measured reflection spectrum at $T = 1.8\,\mathrm{K}$ without an external magnetic field. Lines: Calculated reflection spectra for an inhomogeneously broadened exciton with spatial dispersion ($\hbar\omega_0 = 1.6644\,\mathrm{eV}$,$\Gamma_{\mathrm{inh}} = 1\,\mathrm{meV}$, $\Gamma = 8\,\mu\mathrm{eV}$ and $M = 1.5m_0$) without(green) and with dead layers of 6.5 nm(blue), 13 nm(red) and 19.5 nm(black) thickness.

The calculated and measured reflection spectra do not coincide. The measurement shows a plateau at low energies followed by a dip at 1.6655 eV and another plateau at higher energies. The calculated spectrum rises towards a peak for low energies followed by a dip at higher energies.

This difference can be attributed to the existence of a dead layer. This is a layer at the interface, where excitons are suppressed by strong electric fields. [44]. As there is no exciton resonance, the dielectric function for this layer differs from the rest of the crystal [44, 2] and is given by the background dielectric constant ε_0. This layer has a thickness on the order of the exciton Bohr radius a_{x} ($\sim 10\,\mathrm{nm}$). As this is below the wavelength of light, there is always interference between the light reflected at the interface between atmosphere and the dead layer and at

the interface between the dead layer and the normal crystal. There is further interference inside the dead layer.

A convenient way to calculate the reflection of such a structure is the transfer matrix method [45, 46]. Assuming that the refractive index outside the crystal is equal to 1, the reflection coefficient R of the dead layer with the thickness l_d and refractive index $n_\mathrm{d} = \sqrt{\varepsilon_0} = \sqrt{11.2}$ [47] on top of a bulk crystal with a refractive index of n_b is

$$R = \left| \frac{n_\mathrm{d}\left(1+e^{\xi}+\left(-1+e^{\xi}\right)n_\mathrm{d}\right) - n_\mathrm{b}\left(-1+e^{\xi}+\left(1+e^{\xi}\right)n_\mathrm{d}\right)}{n_\mathrm{d}\left(1+e^{\xi}-\left(-1+e^{\xi}\right)n_\mathrm{d}\right) + n_\mathrm{b}\left(1-e^{\xi}+\left(1+e^{\xi}\right)n_\mathrm{d}\right)} \right|^2 \tag{4.3}$$

$$\xi = \frac{2\mathrm{i}\omega l_\mathrm{d} n_\mathrm{d}}{c}. \tag{4.4}$$

In Fig. 4-3 reflection spectra calculated for dead layers of 6.5 nm (blue), 13 nm (red) and 19.5 nm (black) thickness are shown. With increasing thickness the low-energy peak disappears and the dip moves to lower energies. The spectrum calculated for $l_\mathrm{d} = 13\,\mathrm{nm}$ is in good agreement with our measurement. This thickness is about twice the exciton Bohr radius, which is between $a_\mathrm{x} = 6.0\,\mathrm{nm}$[19] and $a_\mathrm{x} = 7.5\,\mathrm{nm}$[20].* This is the expected ratio between bohr radius and dead layer thickness for the lowest exciton level[44].

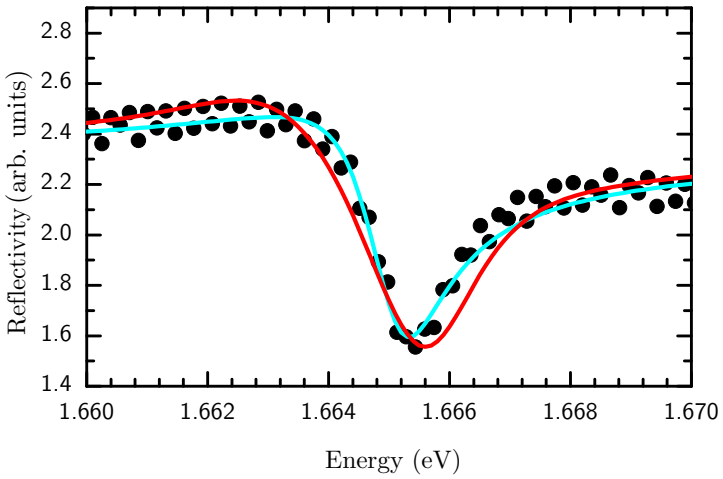

Figure 4-4: Dots: Measured reflection spectrum at 1.8 K and $B = 0\,\mathrm{T}$. Red Line: Calculated reflection spectrum for an inhomogeneously broadened exciton with $\Gamma = 8\,\mu\mathrm{eV}$ and $\Gamma_\mathrm{inh} = 1\,\mathrm{meV}$. Cyan Line: Reflection spectrum of an exciton without inhomogeneous broadening but with an homogeneous broadening of $\Gamma = 1.4\,\mathrm{meV}$ and a resonance energy of $\hbar\omega_0 = 1.6647\,\mathrm{eV}$ behind a dead layer of 12 nm thickness.

Reflection spectra are not suitable to determine all parameters of the exciton.

* According to equation (2.3), for an exciton binding energy of $E_\mathrm{x}10.5\,\mathrm{meV}$[48], a conduction-band mass of $m_\mathrm{e} = 0.094m_0$, a heavy hole mass of $m_\mathrm{hh} = 0.72m_0$ and a light hole mass of $m_\mathrm{lh} = 0.13m_0$ [49], the bohr radii are $a_\mathrm{x} = 6.6\,\mathrm{nm}$ and $a_\mathrm{x} = 8.2\,\mathrm{nm}$ for heavy and light hole excitons, respectively.

One limitation is the type of broadening. In bulk crystal an exciton will be homogeneously broadend, since the excitonic resonance is a damped oscillator. Further, crystal imperfection can lead to spacial fluctuation of the exciton resonance energy. In this case, the excitonic resonance is inhomogeneously broadened [50].†

Reflection spectra are not suitable to distinguish between these two types of broadening as demonstrated in Fig. 4-4. This figure contains the measured spectrum and two calculated spectra. The red line represents a spectrum is calculated with the same excitonic parameters, as they have been used for the best fitting reflection spectrum in Fig. 4-3. The second one, shown as a cyan line, uses the same parameters, but does not assume an inhomogeneously broadend exciton, but only a homogeneous broadening with $\Gamma = 1.4\,\mathrm{meV}$. The exciton energy $\hbar\omega_0 = 1.6647$ differs as well as the thickness of the dead layer $l_\mathrm{d} = 12\,\mathrm{nm}$. Both reflection spectra are in good agreement with the experimental data. But the one calculated for only homogeneous broadening is in better agreement than the one which also assumes inhomogeneous broadening. But as demonstrated in the next chapter one needs additional measurements to decide between them.

4.1.3 Transmission

Reflection measurements allow to determine the resonance energy $\hbar\omega_0$ of the exciton, but it is difficult to judge whether the broadening is homogeneous or inhomogeneous. For this aspect one needs a measurement that is sensitive to the imaginary part of the dielectric function, which is strongly influenced by the broadening. This is true for transmission spectra. If one neglects the reflections at the surfaces, the intensity I_t of light leaving the sample after propagation through the crystal of thickness l_b for a beam of initial intensity I_0 is given by

$$I_\mathrm{t} \quad = \quad I_0 e^{-2\Im(\sqrt{\varepsilon} l_\mathrm{b}\omega/c)}, \tag{4.5}$$

where ε is the dielectric constant and $\hbar\omega$ the photon energy. The measured transmission spectrum without magnetic field at a temperature of $T = 1.8\,\mathrm{K}$ is shown in Fig. 4-5 by black dots. The transmission drops from ≈ 0.7 at 1.65 eV to below 0.01 above 1.661 eV. In Fig. 4-5 two transmission spectra are also shown which have been calculated for the same exciton parameters as those used in Fig. 4-4, but neglecting spatial dispersion. As the transmission is already ≈ 0 at a detuning of $(\hbar\omega_0 - \hbar\omega) = 3\,\mathrm{meV}$, one can use the simplified dielectric function presented in equation (2.11) for the homogeneously broadened exciton and its convolution with a Gaussian distribution for the inhomogeneously broadened exciton.

The calculated spectrum for an inhomogeneously broadened exciton with $\Gamma_\mathrm{inh} = 1\,\mathrm{meV}$ and $\Gamma = 8\,\mu\mathrm{eV}$ is shown as a red curve and is in good agreement with the

†For a more detailed theoretical description see subsection 2.2.2.

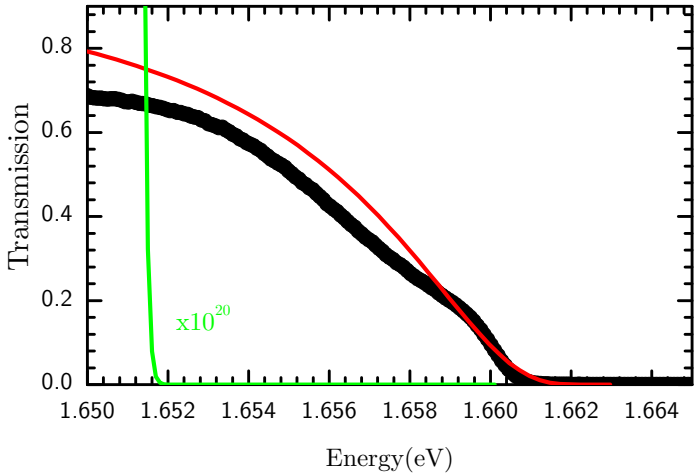

Figure 4-5: Black Dots: Transmission spectrum measured at 1.8 K and $B = 0$ T. Red Line: Calculated transmission spectrum spectrum for an inhomogeneous broadened exciton with $\Gamma = 8\,\mu$eV, $\Gamma_{\text{inh}} = 1$ meV. Green Line: Transmission spectrum of an exciton without inhomogeneous broadening, but with a homogeneous broadening of $\Gamma = 1.4$ meV. Both lines were calculated using a resonance energy of $\hbar\omega_0 = 1.6647$ eV.

measurement. For the exciton with a homogeneous broadening of $\Gamma = 1.4$ meV, the calculated transmission is so small, that it can be neglected. This clearly indicates that the large broadening is not homogeneous. Transmission close to this exciton resonance is only possible, if the homogeneous broadening due to dampening is small. The value of 8 µeV is comparable to values reported for ZnO and GaN bulk crystals [51, 52, 53].

4.1.4 Diamagnetic shift

A magnetic field influences the PL and the reflection spectra. In Fig. 4-6 both spectra for $B = 0$ T and $B = 7$ T are presented. The PL intensity of the UP peak is increased by a factor of 5, when a magnetic field of $B = 7$ T is applied compared to $B = 0$ T. Furthermore, the energy of the UP peak changes. The reflection spectra also show movement of the dip.

The energies of the UP PL peak for magnetic fields ranging from $B = 0$ T to 7 T are shown as black squares in Fig. 4-7 together with the resonance energies of the reflection spectra, which are represented by red dots. Both the UP PL and the reflection spectra resonance energy increase with the magnetic field. Two parabolas are fitted to the data in Fig. 4-7. The red parabolic line represents a diamagetic shift of 28 µeV T^{-2} and is in good agreement with the exciton resonance energy determined using reflection spectra. The UP PL peak is in good agreement with the black curve, which represents a diagmagnetic shift of 15.8 µeV T^{-2}.

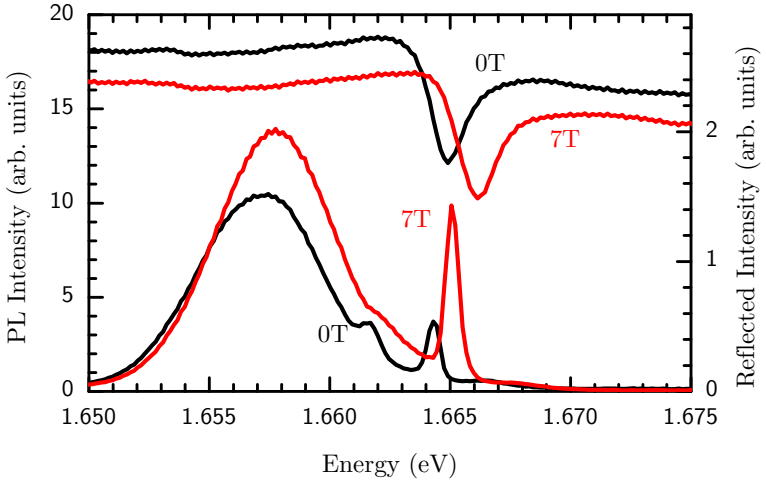

Figure 4-6: Reflection spectra, shown in the upper part, and PL spectra, shown at the bottom measured at $T = 1.8\,\mathrm{K}$. Data for $B = 0\,\mathrm{T}$ is represented by black lines, while data for $B = 7\,\mathrm{T}$ is shown as red lines.

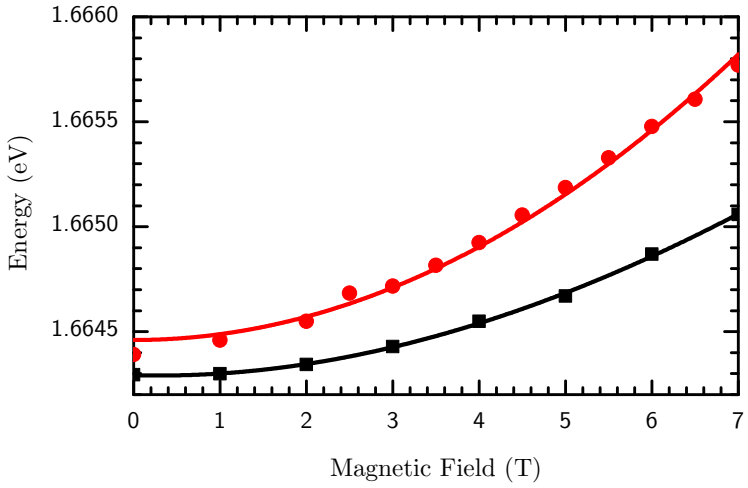

Figure 4-7: Magnetic field dependence of the resonance energy taken from the reflection spectra (red dots) and the UP PL peak energy (black squares). The lines are parabolas representing a diamagnetic shifts of $28\,\mu\mathrm{eV\,T^{-2}}$(red line) and $15.8\,\mu\mathrm{eV\,T^{-2}}$(black lines).

4.2 Exciton polariton propagation

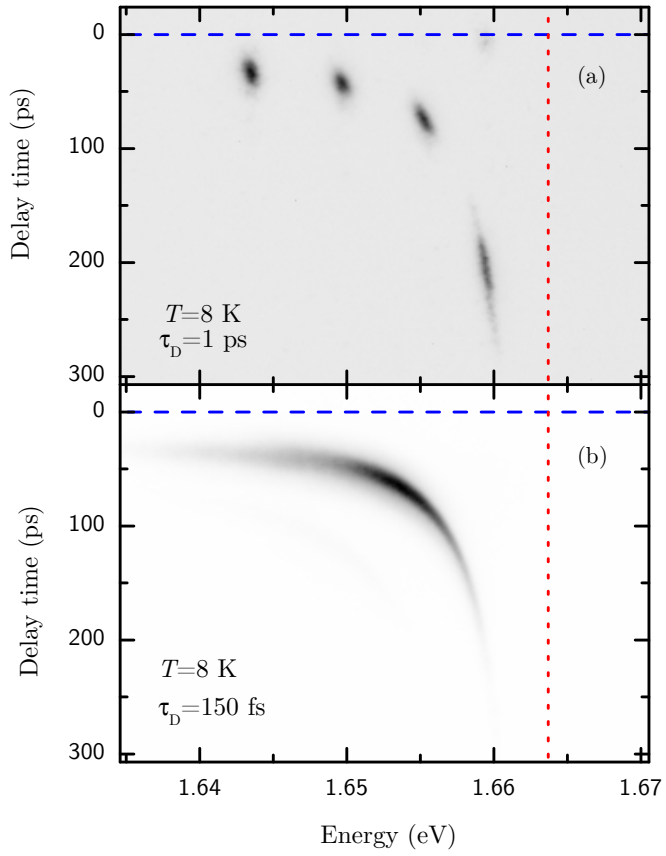

Figure 4-8: 2D contour plots with energy and time of arrival as axis of the intensity of different optical pulses transmitted through the sample. (a) Superposition of 4 pulses of 1 ps duration with different photon energy. (b) 1 pulse of 150 fs duration. Red vertical line: Exciton resonance energy $E_{exec} = 1.6644\,\mathrm{eV}$.

To study the propagation of polaritons close to the fundamental exciton resonance the setup presented in chapter 3.1 was used. The crystal had a thickness of $l = 745\,\mu\mathrm{m}$ maintained at a temperature of $T = 8\,\mathrm{K}$. The mode-locked Ti:Sapphire laser used in the experiment could produce two types of laser pulses:

(i) Pulses with a duration of $\tau_\mathrm{d} \approx 150\,\mathrm{fs}$. These pulses are spectrally broad. Their full width at half maximum is 12 meV. When using them one can obtain the polariton dispersion in this energy range within a single measurement.

(ii) Pulses with a duration τ_d of about 1 ps. Because they are spectrally narrow ($\approx 1\,\mathrm{meV}$) it takes several measurements to obtain the polariton dispersion. The advantage of this method is that one may measure the dispersion at photon energies of stronger absorption. This is not possible with spectrally wide pulses due to the limited dynamical range of the streak camera.

Fig. 4-8(a) shows the delay, which is introduced by propagation through the sample, for four laser pulses of $\tau_d = 1$ ps duration with different energy. The pulses are shown as black shadowed areas, and with increasing energy the delay increases. From the view of an experimentalist it is worth mentioning that Fig. 4-8(a) is an overlay of four measurements using 1 ps long pulses with different energies. For each measurement the power density $P \leq 10$ mW/cm^2 was kept low and is in the linear regime.

Fig. 4-8(b) is a single measurement using 150 fs long pulses of low power density ($P \leq 10$ mW/cm^2). Without the sample all energy components would arrive with the same delay. After passing through the sample the pulse is distorted, as demonstrated by the black curve. Each spectral component arrives at a different time. The higher the photon energy the stronger the delay of the pulse. It is also noteworthy that the pulse is still spectral and temporal continuous.

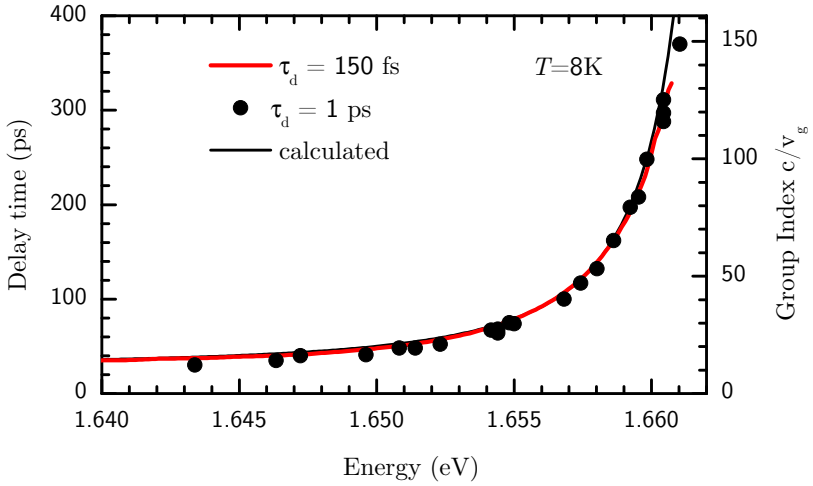

Figure 4-9: Energy dependence of the delay time measured with several pulses of 1 ps (black dots) and one 150 fs duration (red line). The calculated delay or group index is shown as a black curve.

The energy dependence of the delay time determined from these two images is shown in figure 4-9. The black dots represent measurements with ps-pulses, while the red line under the black dots is extracted from a measurement using 150 fs pulses. The two measurements are in very good agreement. From that one can conclude that there is no significant effect of the high energy tail of the 150 fs pulse on the speed of propagation.

The group index $c/v_g = n_g$, shown as a black line, was calculated neglecting spacial dispersion but including inhomogeneous broadening. For this calculation equation (2.6) from section 2.2.4 was used in combination with the dielectric function of the inhomogeneously broadened simplified model a according to equation 2.12 and the exciton parameters gained in section 4.1.2. Assuming ballistic propagation the delay τ is simply $\tau = n_g l/c$. The calculation is in good agreement with the experimental data.

4.2.1 Ballistic propagation

The calculated data shown in the previous section are based on the assumption that the propagation is ballistic. As there are two principle types of propagation, ballistic and diffusive, one needs to verify this assumption. Ballistic propagation is directional and needs changes in the medium to alter the direction of propagation. Diffusive propagation does not have a direction of propagation.

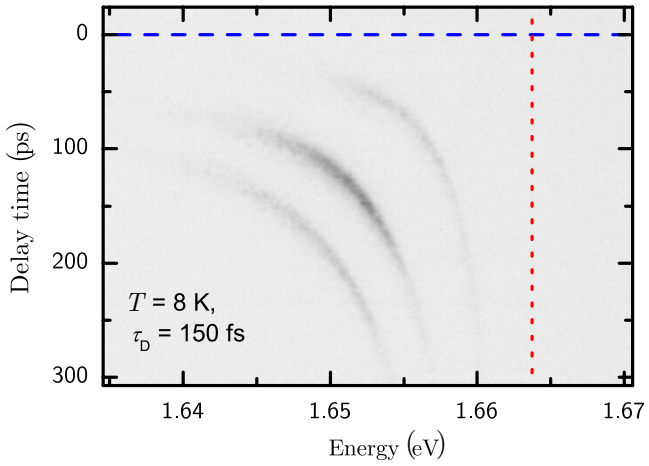

Figure 4-10: Contour plot of intensity of light leaving the sample versus delay time and energy. The sample is rotated slightly out of normal incidence and was hit Red vertical line: Exciton resonance energy $E_{\mathrm{exec}} = 1.6638\,\mathrm{eV}$.

Fig. 4-10 demonstrates the results of a time of flight measurement taken under the same conditions as for Fig. 4-8(b), but the sample is slightly rotated. While the black shadowed areas in Fig. 4-8(b), which indicate the arrival of the spectral components of the laser pulse with 150 fs duration, can be described by a single continuous curve, the shadowed areas in Fig. 4-10 form three curves. From this one can conclude that, due to the rotation of the sample, a spectral component does not arrive at a single time, but at three different times.

The smallest delay is the same as in figure 4-8, but the other two delays are three or five times its value. These curves are due to reflection at the surfaces of the sample. They leave the sample at a slight angle as the front and the back of the sample are not perfectly parallel. After reflection the light will not propagate back on the same path as the incident pulse, but under an angle.

Reflection is not possible for diffusion. Diffusion can be described with Fick's laws [54]. The first Fick's law $J = -D\nabla\phi$ states that the flux J is proportional to the gradient $\nabla\phi$ of the polariton concentration ϕ. Without external influence the gradient cannot reverse it's sign with time and the direction of flux cannot change. Since the only mayor external influence on the polariton concentration is the exciting laser pulse creating an initial population at the surface, diffusive propagation would not reverse.

As we can only explain reflections by ballistic propagation, their presence confirms that the polariton propagation is ballistic. During ballistic propagation scattering can still influence the propagation of light by changing the wave vector. This would result in a wider aperture for the cone of light leaving the sample, then the cone of light entering it. This behaviour would be visible in the angle distribution of the transmitted beam intensity. The distribution is shown for three for different photon energies in figure 4-11.

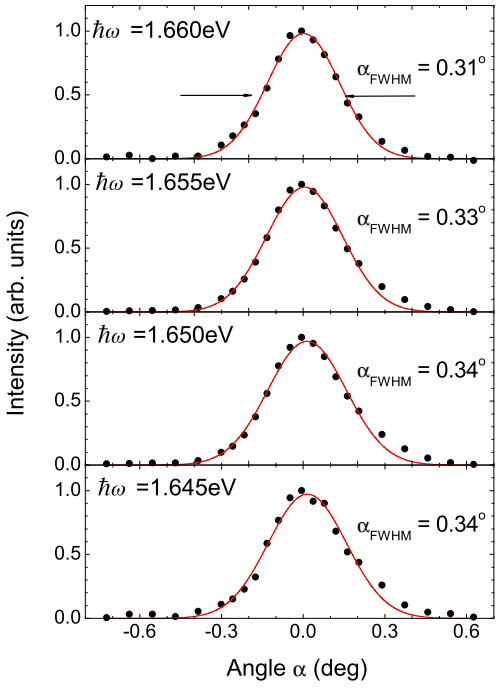

Figure 4-11: Transmitted beam intensity as a function of the detection angle α for four photon energies $\hbar\omega$. α is taken relatively to the normal of the surface. Black dots represent the measured data, while the solid red lines are fits with a Gaussian distribution.

The dependences can be described by a Gaussian distribution with a full width at half maximum $\alpha_{\mathrm{FWHM}} = 0.33°$, and is independent of the excitation energy. The width is defined by the aperture angle of the laser beam focused onto the sample and no widening of the beam can be observed. From this one can conclude, that the wave vector is conserved and the wave vector conserved. Further one can assume that the dominant source of scattering in these highly pure samples is mainly inelastic scattering on acoustical and optical phonons. Under these conditions the propagation should not influence the coherence of the transmitted light.

4.3 Exciton polariton propagation in an external magnetic field

4.3.1 Influence on the time of flight

Application of an external magnetic field leads to a diamagnetic shift of the exciton resonance, as discussed in section 4.1.4. This affects the spectral dependence of the delay of light after propagation through the sample. In Fig. 4-12 the time of

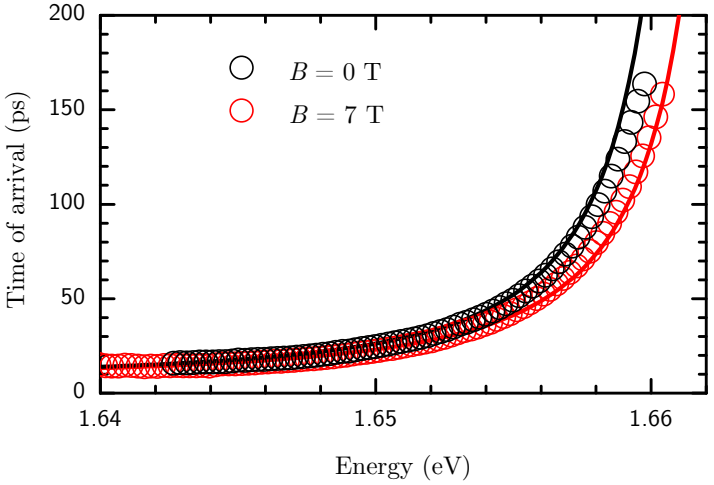

Figure 4-12: Measured spectral dependence of the time of arrival after propagation through a 655 µm thick sample kept at $T = 1.8\,\mathrm{K}$. The black circles represent results measured at $B = 0\,\mathrm{T}$, while data measured at $B = 7\,\mathrm{T}$ are shown as red circles. The black curve was calculated using equations (2.12) and (2.6) for an exciton resonance $\hbar\omega_0 = 1.6644\,\mathrm{eV}$ and the red curve was calculated for $\hbar\omega_0 = 1.6658\,\mathrm{eV}$. The inhomogeneous broadening was $\Gamma_{inh} = 1\,\mathrm{meV}$ and the homogeneous was $\Gamma = 8\,\mu\mathrm{eV}$.

arrival of the exciton polaritons measured for $B = 0\,\mathrm{T}$ and $B = 7\,\mathrm{T}$ in a 655 µm thick crystal kept at a temperature of $T = 1.8\,\mathrm{K}$ is shown. The two measurements are almost identical except that for the higher magnetic field is shifted to higher energies. In Fig. 4-12 theoretical curves for the time of arrival calculated for $\hbar\omega_0 = 1.6644\,\mathrm{eV}$ and $\hbar\omega_0 = 1.6658\,\mathrm{eV}$. The resonance energies extracted from reflection spectra demonstrated in section 4.1.4, are also shown.

The measured data and the two curves are in good agreement. From this one can derive that the spectral dependence of the delay follows the exciton resonance.

4.3.2 Change of polarization

Fig. 4-13 summarizes the temporal and spectral variations of the transmitted optical pulse intensity in the axis frame x', y' and its linear polarization S_2. They were acquired using the polarimetric time-of-flight technique described in chapter

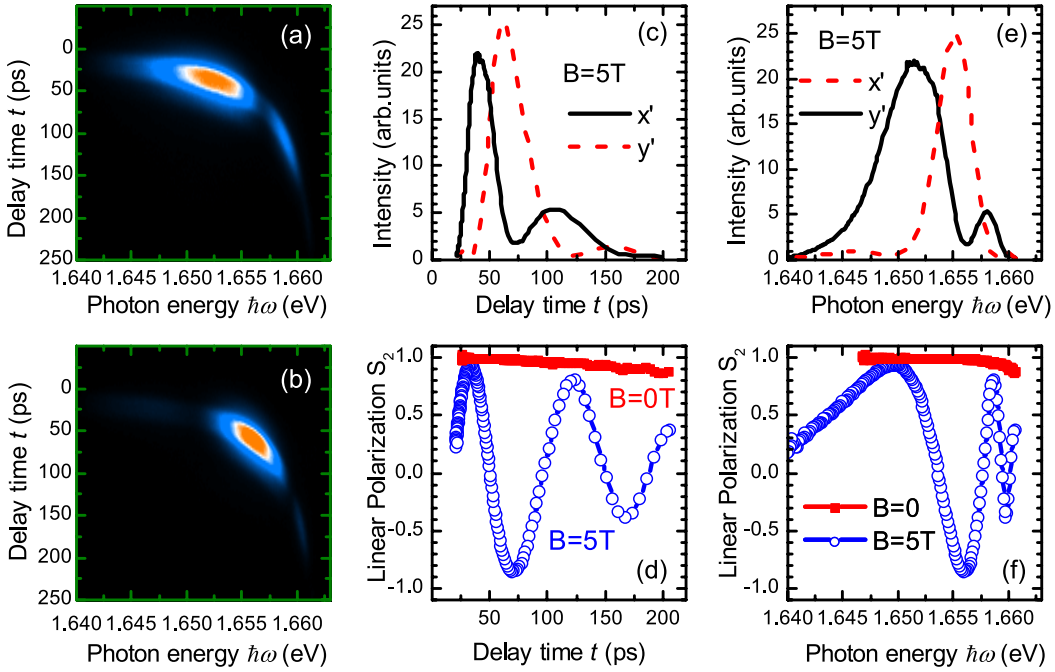

Figure 4-13: (a) and (b) Contour plots of transmitted pulse intensities measured as function of photon energy $\hbar\omega$ and time delay t at $B = 5$ T. Panels (a) and (b) correspond to the data measured in linear x' and y' polarizations, respectively. (c) gives temporal dependences of the intensities $I_{x'}$ (solid line) and $I_{y'}$ (dashed line) and (d) shows the temporal evolutions of linear polarization degree S_2 measured at $B = 5$ T (open circles) and $B = 0$ T (solid squares). The spectral dependences of $I_{x'}$ and $I_{y'}$ are displayed in (e) and of S_2 in (f). The incoming pulse is linearly polarized along x' ($S_2 = 1$).

3.1. To determine the polarization of light one needs 6 intensity measurements in total and two per polarization, see equations 2.22. The results of two such measurements, where the transmitted intensity was taken for linear polarizations along the x' and y' axes at $B = 5$ T, are shown by the contour plots in Figs. 4-13(a) and 4-13(b). The pulse incident on the sample was linearly polarized along $x'(S_2 = 1)$. The time $t = 0$ corresponds to the arrival time of the optical pulse without the sample in the optical path.

In contrast to Fig. 4-8(b), which shows a distorted but continuous pulse, in Fig. 4-13(a) and (b) certain spectral and temporal components are very weak or missing.

The intensity of the two measurements can be analyzed depending on delay time (Fig. 4-8(c)) or energy (Fig. 4-8(e)). This is possible since there is a strictly increasing relation between the photon energy $\hbar\omega$ and the delay τ, as demonstrated in chapter 4.2. Accordingly, the polarization can be calculated on basis of equation (2.22).

The application of a magnetic field leads to pronounced oscillations in the temporal and spectral dependences of the linear polarization S_2 as shown in Figs. 4-

13(d) and 4-13(f). This is in contrast to data measured without magnetic field, which are also shown in Fig. 4-13. In zero magnetic field the polarization state of the incoming pulse is fully conserved. One can see that S_2 is almost constant against the time delay and in the spectral domain. First of all, this means that the system is isotropic at $B = 0$. Secondly, nearly no depolarization takes place, so that the exciton polariton propagation is coherent.

The frequency of the oscillations induced by a magnetic field of $B = 5$ T increases with an increase of $\hbar\omega$ in the spectral domain, see Fig. 4-13(f). In the time domain, shown in Fig. 4-13(d), it is almost constant. This is as expected for a magnetic-field-induced anisotropy due to splitting of exciton Zeeman sublevels. As equation (2.39) states, that the phase difference between the two eigenwaves $\phi \approx \Omega_{\text{eff}}\tau$ increases linearly with time of arrival. The resulting polarization degree oscillates with a frequency of Ω_{eff}.

This allows the determination of the effective Zeeman splitting, even when it is hidden by inhomogeneous broadening in the spectral domain. In Fig. 4-13(d) more than two full oscillations are visible for a magnetic field strength $B = 5\,\text{T}$. Such strong retardation results from the large delays of light in the sample. This result is quite interesting from an application point of view, because it allows to achieve optical modulation at high frequencies of about 10 GHz.

4.3.3 Identification of polarization effects

In the previous chapter it was demonstrated that there are strong polarization effects. The relationship to the delay was discussed, but not which effects are present. To be able to describe the effects and their spectral and temporal behavior one must identify them first.

4.3.3.1 Faraday rotation

If one applies a magnetic field to a transparent sample in Faraday geometry, the strongest expected magneto-optical effect on the polarization of the light will be Faraday rotation. One can also assume that a resonance, that exhibits a Zeeman splitting, causes Faraday rotation. In (Cd,Zn)Te the refractive index n for the transparent region can be calculated with just two effective resonances [6]. For most of the transparent region a single effective oscillator (SEO) model, as proposed by S. H. Wemple and M. DiDomenico[5], is sufficient to calculate the refractive index [6]. In this model resonances of the X- and L- point of the band structure are represented by a single, very strong effective resonance. To calculate the refractive index for light with a photon energy close to the fundamental band gap one needs to add a second resonance of lower energy to account for the interband transitions at the fundamental band gap [6].

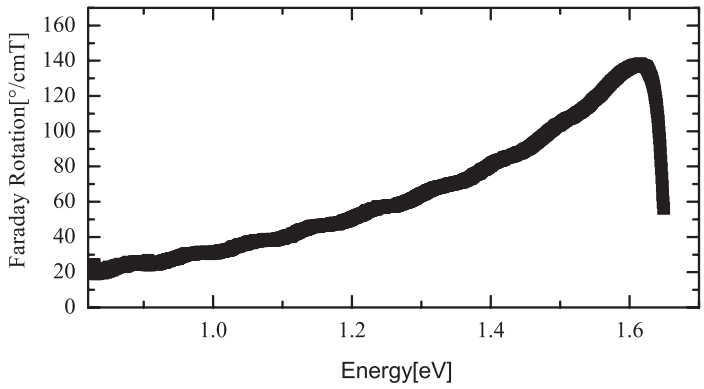

Figure 4-14: Faraday rotation measured at $B = 7\,\mathrm{T}$ and $T = 1.8\,\mathrm{K}$.

Even though it is possible to take the resonances of the X- and L-point of the band structure as a single effective resonance for the refractive index, one can not apply this model to calculate Faraday rotation. Each of these resonances can possibly cause Faraday rotation leading to a non-trivial spectral dependence. In addition to calculating Faraday rotation not being feasible [7], previous measurements for pure CdTe differ by a factor of more than 2 [9, 7]. This makes it necessary to study the Faraday rotation in a wide energy window.

In Fig. 4-14 the measured spectral dependence of the rotation angle from 0.84 eV to 1.65 eV is shown. It has been measured at a magnetic field of $B = 7\,\mathrm{T}$ and a temperature of $T = 1.8\,\mathrm{K}$ in a 655 µm thick sample. From 0.8 eV to 1.6 eV Faraday rotation slowly increases with photon energy. Above 1.62 eV the Faraday rotation decreases fast with photon energy.

This spectral dependence can be explained by the contribution of several resonances. One can attribute the slow rise to the resonances that contribute to the SEO, while the fast change is due to the Zeeman splitting of the fundamental exciton resonance. A large detuning leads to slower spectral changes for polarization effects, while a small detuning results in steeper spectral changes. Further a resonance needs to affect the refractive index in order to induce Faraday rotation. Because of this, one can neglect the effect of the of the fundamental resonance on the refractive index for light, if the photon energy is at least 200 meV below the energy of the fundamental resonance [6]. So, while the resonances of the SEO determine the refractive index and Faraday rotation of most transmitted photon energies, the fundamental resonance can only induce significant Faraday rotation in a narrrow spectral window.

The fundamental resonance and the resonances of the SEO cause Faraday rotation with opposing sign. Because of this there is an energy where the two contributions cancel each other out, resulting in the absence of Faraday rotation.

4.3.3.2 Magneto-spatial dispersion

The second phase-based polarization effect is linear birefringence. In Faraday geometry its source is magneto spatial dispersion and the sign of the product of the magneto spatial dispersion constant V and the wavevector k_z determines which linearly polarized eigenwave propagates faster.

When linear birefringence is the only polarization effect, a phase difference occurs during propagation between the two eigenwaves. This phase difference will be compensated, if the light is reflected and propagates back on its previous path This is a reliable way of distinguishing between linear birefringence due to magneto-spatial dispersion and circular dichroism. Both effects can create circular polarization, but only linear birefringence switches sign when the wavevector is inverted.

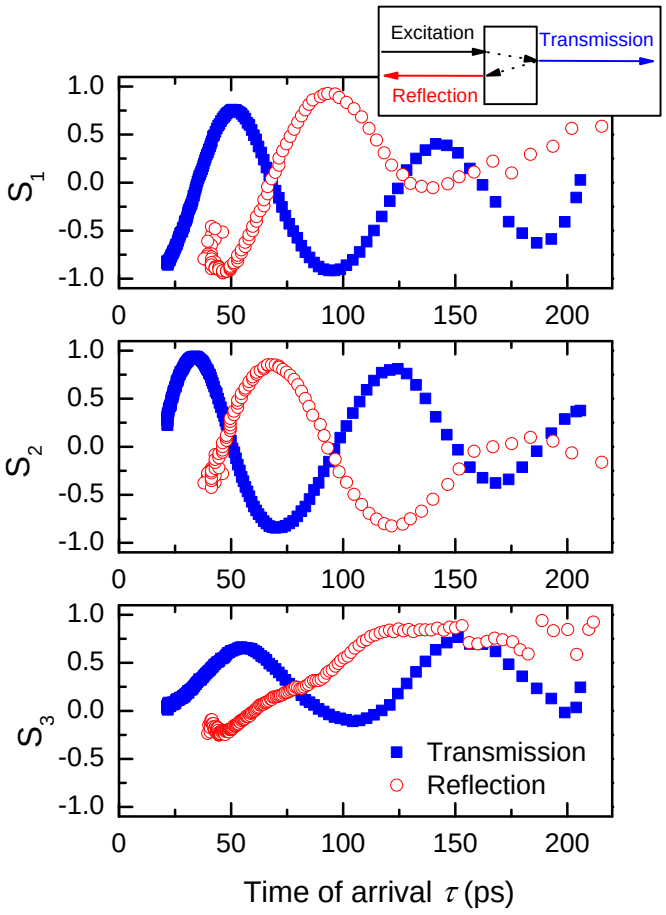

Figure 4-15: Comparison of the polarization of light leaving a 655 µm thick sample at $B = 5\,\mathrm{T}$ and $T = 1.8\,\mathrm{K}$, that was S_2 polarized before entering the sample. Blue squares: transmitted light, red circles: Light that is reflected and propagates back through the sample.

Fig. 4-15 shows the time of arrival dependence of the polarization of light leaving the sample at $B = 5\,\mathrm{T}$ and $T = 1.8\,\mathrm{K}$. The curve labeled 'Transmis-

sion' accounts for light that propagates through the sample once. 'Reflection' is attributed to light that propagates through the crystal once, is reflected at the surface and leaves the sample at the other surface. In both measurements the light is $S_2 = 1$ polarized when it first enters the sample.

'Transmission' shows oscillations in all three polarizations. 'Reflection' oscillates in the two linear polarizations S_1 and S_2 but not in S_3. In S_3 there is only a drift towards positive circular polarization. The oscillations of 'Transmission' and 'Reflection' are of similar frequency, but do not match in phase.

Since Faraday rotation does not compensate itself, both 'Reflection' and 'Transmission' show oscillations in the linear polarizations. For the same energy of light the 'Reflection' will have twice the time of flight and Faraday rotation compared to 'Transmission'. This leads to the fact that oscillations in S_1 and S_2 having the same frequency but different phase.

The oscillations in S_3 which are visible in transmission geometry are missing in reflection, since the linear birefringence compensates itself. The drift towards positive circular polarization might be due to circular dichroism.

4.3.3.3 Dichroism

Dichroism can be easily identified by its ability to polarize light by absorbing one eigenpolarization stronger than the other. Birefringence can change polarization but cannot generate it. In Fig. 4-16 the polarization of light leaving the sample is shown for applied magnetic fields of $B = 0\,\mathrm{T}$ and $B = \pm 5\,\mathrm{T}$. The light is unpolarized before entering the sample. There is no polarization generated without an applied magnetic field. At $B = \pm 5\,\mathrm{T}$ there is polarization generated in all three polarizations for energies above 1.654 eV and below 1.662 eV. If we study the effects while changing the sign of the magnetic field, we see that the total polarization $|S|$ generated by both directions of the magnetic field is the same. The generated polarization in S_1 and S_3 is of opposite sign for opposite magnetic field values. In contrast the S_2 polarization does not change sign with magnetic field.

The energy window in which polarization is generated is the same as the transmission edge shown in Fig. 4-5. As dichroism is an absorption based effect it can only occur for photon energies in the absorption region of the material. The drop of polarization above 1.66 eV is most likely not an effect of the sample but a measurement error. At these energies there is very little transmitted light and the background of the measurement, which is unpolarized, becomes more dominant.

The polarization in S_1 is generated by linear dichroism, due to different absorption for light polarized along the [100] and [010] crystal axes. By changing the magnetic field direction, this difference in absorption changes its sign.

The polarization in S_2 is of common sign for $B = \pm 5\,\mathrm{T}$. This in contrast to

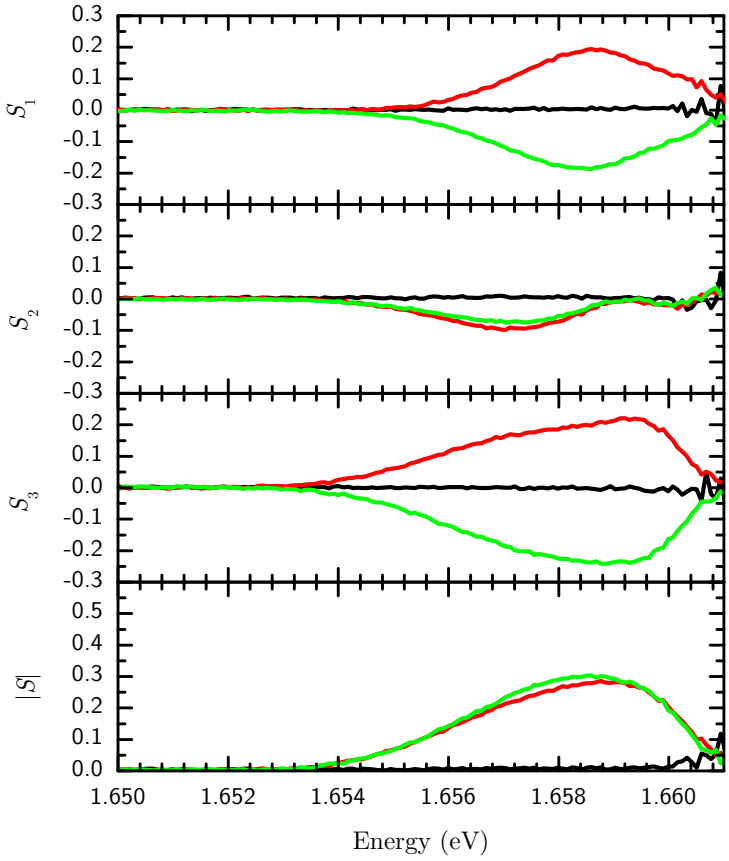

Figure 4-16: Measured spectral dependences of the polarization of beams of light, that entered the sample unpolarized, after propagation through the crystal at different magnetic fields. The black, red and green lines represent data measured at $B = 0\,\mathrm{T}$, $B = 5\,\mathrm{T}$, $B = -5\,\mathrm{T}$.

the expectation for a single resonance, where one would expect $S_2 = 0$. According to equations (2.35) and (2.36) the arguments $\varphi_{\mathrm{off}} = \arg(\varepsilon_{\mathrm{off}})$ and $\varphi_{\mathrm{dia}} = \arg(\varepsilon_{\mathrm{dia}})$ have only a neglectable difference as long as $\Im(k_z) \ll \Re(k_z)$. As shown in the appendix 8.3, S_2 vanishes for both eigenwaves if $\varphi_{\mathrm{off}} = \varphi_{\mathrm{dia}}$. Due to this, the relative suppression of one eigenwave, which is the origin of dichroism, will not generate any polarization in S_2.

The polarization observed in S_2 is due to the contribution of the resonances of the X- and L-point to $\varepsilon_{\mathrm{off}}$, which changes φ_{off}. A more visual description is, that the Faraday rotation created by the higher energy resonances rotates the linear polarization, which is generated by the linear birefringence of the exciton, from S_1 into S_2. As both the dichroism and the additional Faraday rotation change their sign with inversion of the magnetic field, the the sign of the polarization measured in S_2 keeps is the same.

The different behaviour of the sign for the polarization measured in S_1 and S_2 when the external magnetic field is inverted can be used to confirm the alignment of

the experiment.As both the polarization measured in S_1 and S_2 behave as predicted by theory, one can assume that the orientations of the experimental $\vec{x}$ and $\vec{y}$ axes to the crystal axes are $\vec{x} \parallel [100]$ and $\vec{y} \parallel [010]$. The orientation of the crystal axes has also been confirmed by Laue X-ray diffraction.

4.3.4 Characterization of magneto-spatial dispersion

The main effect of magneto-spatial dispersion is linear birefringence. The determination of the strength of linear birefringence can be simplified, if there is no circular birefringence complicating the evaluation. As discussed in chapter 4.3.3.1, there is a certain photon energy where there is no circular birefringence (Faraday rotation).

One possibility to identify this photon energy is the study of the effects of the sample on linearly polarized light. The measured polarization of light leaving the sample for different detunings $E - \hbar\omega_0$ is shown in the upper part of Fig. 4-17. The light is $S_2 = 1$ polarized before entering the sample for all photon energies. After leaving the sample light with a detuning energy below 15.2 meV is negatively S_1 polarized. With increasing energy the light gets more S_2 polarized. With higher energies circular polarization increases. At even higher energies there are oscillations in S_1, S_2 and S_3.

At a detuning energy of -15.2 meV, indicated by a black vertical line in Fig. 4-17, there is no S_1 polarization. Also the light entered the sample with no S_1 polarization. As there is no absorption at this energy, the Faraday rotation is either absent or rotated the linear polarization by a multiple of 180°. The second option can be excluded, as the Faraday rotation introduced by a sample of 655 µm thickness of $B = 5$ T never exceeds 50° for photon energies below 1.65 eV (1.65 eV correspond to a detuning energy of -15.2 meV, compare Fig. 4-14). From this one can conclude, that there is no Faraday rotation at a detuning of -15.2 meV

At this detuning energy there is a S_3 polarization indicating the presence of linear birefringence. One can characterize linear birefringence, using its dependence on the angle of exciting linear polarization. The dependence of the polarization of exiting light on the angle α of linear polarization relative to $\vec{x}$ is shown in the lower part of Fig. 4-17. The black squares are measured for a detuning energy of -15.2 meV and $B = 5$ T. The measured S_1 polarization can be described by a $\cos(2\alpha)$ function, while S_2 follows a $\sin(2\alpha)$ function, both with an amplitude close to one. S_3 also follows a $\sin(2\alpha)$ function but with a smaller amplitude.

For pure linear birefringence in the basis of $\vec{x}$ and $\vec{y}$ the circular polarization S_3 reads as

$$S_3 = \sin(2\alpha)\sin(\Delta\phi), \tag{4.6}$$

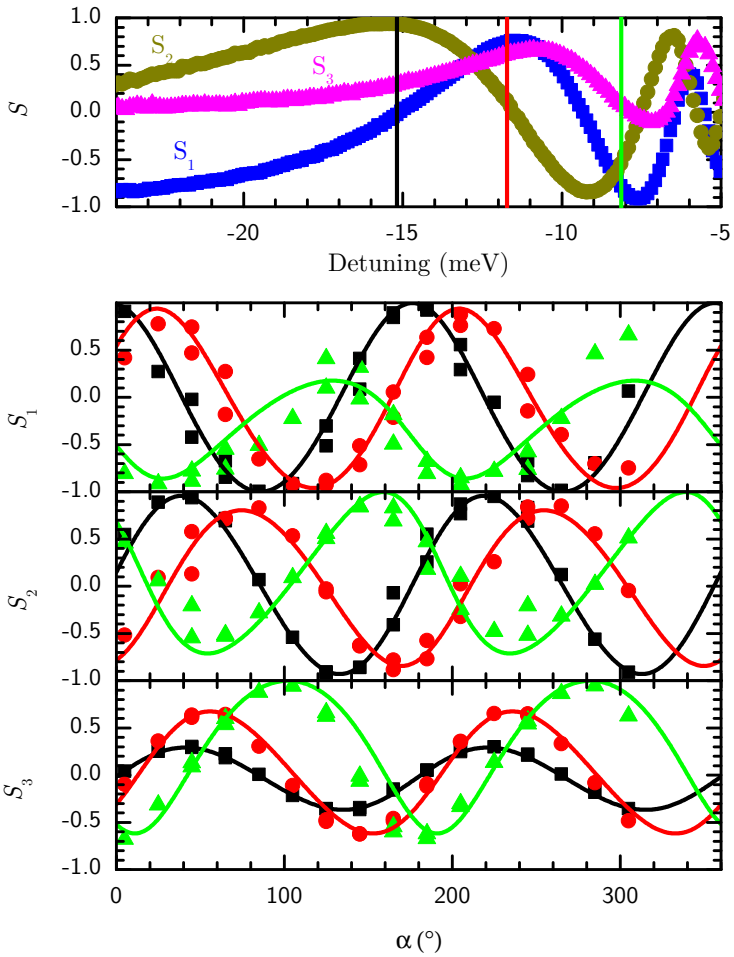

Figure 4-17: Upper graph: Spectral dependence of the polarization of transmitted light in the vicinity of the exciton resonance. The light was $S_2 = 1$ polarized before entering the crystal at $T = 1.8\,\mathrm{K}$ and $B = 5\,\mathrm{T}$. Lower graph: Dependence of the polarization of light leaving the sample at $T = 1.8\,\mathrm{K}$ and $B = 5\,\mathrm{T}$ on the angle of α of the entering linear polarization relative to $\vec{x}$. Black squares represent measured polarization at a detuning energy$(E - \hbar\omega_0)$ of $-15.2\,\mathrm{meV}$, red dots at a detuning energy of $-11.7\,\mathrm{meV}$ while green triangles where measured at $-8.1\,\mathrm{meV}$ detuning. These energies are indicated in the upper graph by vertical lines of their respective colours. The coloured curves in the lower graph are calculated from a dielectric tensor, that was fitted to the experimental data.

where $\Delta\phi$ is the phase difference of the two propagating eigenwaves. The black curve plotted in Fig. 4-17 is calculated for a phase difference of $\Delta\phi = 0.32$ and is in good agreement with the experimental data. In the absence of Faraday rotation one can simplify equation (2.32) to $\hbar\Omega_{eff} = 2Vk_zB$. Using equation (2.39) one can evaluate $V = \phi c/[2(n_g - n_0)k_zLB_z] = 5 \times 10^{-12}\ \mathrm{eVcmT}^{-1}$. With a known V, one can calculate the linear birefringence for different energies.

4.3.5 Spectral dependence of the dielectric tensor

After identifying and characterizing the polarization effects it is of interest if the excitonic model proposed in chapter 2.2.7 can describe these effects. The model predicts the dielectric tensor for a specific energy using a given dielectric function, which, in turn, has to be calculated from excitonic parameters. This model needs to be verified by comparing it with values extracted from measurements.

The dielectric tensor at the detuning energy of $-15.2\,\mathrm{meV}$ is known. Since there is no Faraday rotation or dichroism, the off-diagonal elements of the dielectric tensor vanish ($\varepsilon_{off} = 0$). The difference between the diagonal elements of the dielectric tensor $\varepsilon_{\mathrm{dia}}$ can be calculated as

$$\varepsilon_{\mathrm{dia}} = \frac{d\varepsilon_0}{d\omega}\frac{2Vk_zB}{\hbar}.$$

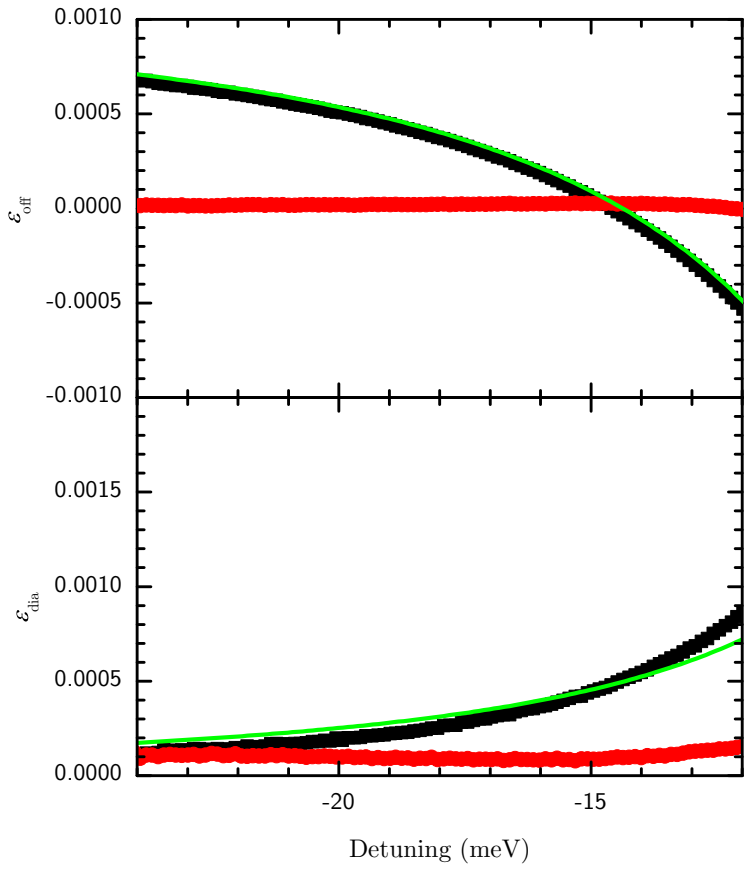

Figure 4-18: Spectral dependence of the off-diagonal ε_{off} (upper graph) and diagonal ε_{dia} (lower graph) contributions to the dielectric tensor at $B = 5\,\mathrm{T}$ and $T = 1.8\,\mathrm{K}$. Black squares represent the real part and red dots the imaginary part extracted by a fit of the angular dependence of the polarization as shown in the lower part of figure 4-17. Calculated spectral dependences of the real part are shown as green curves for a magneto-spatial constant of $V = 5 \times 10^{-12}$ eVcmT^{-1} and a Zeeman splitting of $\Delta = 55\,\mu\mathrm{eV}$.

This tensor can be a starting point for a fit to extract the dielectric tensor of all detuning energies. The dependence of the polarization $\vec{S}$ on the angle of the linearly polarization α relative to $\vec{x}||[100]$ of the incident light[‡] can be used, for this. To be able to fit it one needs to calculate the dependence for different ε_{dia} and ε_{off}. The algorithm to calculate the dependence of the polarization $\vec{S}$ on the angle of the linearly polarization is presented in appendix 8.2. The result of the algorithm is fitted to the experimental data by minimizing the sum of the squared differences between the calculated and measured stokes vectors by varying the real and imaginary parts of ε_{dia} and ε_{off}.

Fitted theoretical curves for $-11.7\,\text{meV}$ and $-8.1\,\text{meV}$ detuning are shown in figure 4-17 together with the corresponding measured data and the experimental and calculated data for $-15.2\,\text{meV}$ detuning, which has been discussed in section 4.3.4. If one compares $-11.7\,\text{meV}$ to $-15.2\,\text{meV}$ one notices that the angle dependence is shifted to higher angles. This is due to the Faraday rotation that is present at $-11.7\,\text{meV}$ but not at $-15.2\,\text{meV}$. Also the amplitude of the oscillation in S_3 is stronger, as the linear birefringence increases the closer the photon energy E is to the exciton resonance.

When comparing the results for $-8.1\,\text{meV}$ detuning to those of $-11.7\,\text{meV}$ one can see another shift to higher angles. But the most striking difference is that the oscillations are no longer around 0. S_1 is shifted to the negative, S_2 as well as S_3 is shifted towards positive values. This is the consequence of dichroism. The shifts are in the same direction as the generated polarization, shown in figure 4-16. Another consequence is that the angular dependence can no longer be described by simple sine- or cosine-functions. The calculated curves for the linear polarization start to take up the character of a sawtooth function.

The results of the fits described above are shown in figure 4-18 together with other detunings between $-24\,\text{meV}$ to $-12\,\text{meV}$[§] detuning. Real parts are shown as black squares while the imaginary parts are represented by red dots. In the upper part of figure 4-17 values for ε_{off} are shown. Its real part is 6.5×10^{-4} at $-24\,\text{meV}$ detuning energy due to the contributions of the higher energies resonances discussed in chapter 4.3.3.1. With increasing photon energy it then starts to decrease. At $-15.2\,\text{meV}$ detuning it is 0, resulting in the absence of Faraday rotation. It decreases further as the photon energy gets closer to $\hbar\omega_0$ until reaching -2×10^{-2} at $-8\,\text{meV}$ detuning. The real part of ε_{dia} is almost 0 at $-24\,\text{meV}$ detuning and increases with photon energy. At $-8\,\text{meV}$ it has a value of 2.9×10^{-2}. Both imaginary parts are 0 for detunings below $-14\,\text{meV}$. Above this energy, both

[‡]The incident light is completely linearly polarized.

[§]It is possible to fit for detunings above $-12\,\text{meV}$, but calculated and measured angle dependences differ significantly in S_1 and S_3. The model neglects reflection at the surfaces. Since the eigenwaves are not orthagonaly polarized (no anti-parallel Stokes vector) for these photon energies, see subsection 4.3.3.3, one can expect polarization dependent reflection.

imaginary parts increase in the same direction as the corresponding real parts.

After extracting values for the different contributions of the dielectric tensor one can compare them with those predicted by equations (2.36a) and (2.36b). The two green lines in figure 4-18 represent corresponding calculations. The off-diagonal contributions to the dielectric tensor are calculated according to $\varepsilon_{\text{off}} = \gamma_1 B_z$, where γ_1 is calculated according to equation (2.36a). The calculated ε_{off} for a Zeeman splitting of $\Delta = 55\,\mu\text{eV}$ and $\gamma_1' = 2.2 \times 10^{-4}\text{T}^{-1}$ is shown in figure 4-18 as a green line. It is in good agreement with the data extracted from the measurements.

The difference of the diagonal elements of the dielectric tensor are given by $\varepsilon_{\text{dia}} = VkzB\gamma_2$ using (2.36b) to calculate γ_2. It is represented in the lower part of figure 4-18 by the green curve. The agreement between the calculated and extracted data is reasonable.

As there is decent agreement between the extracted and calculated dielectric tensor, one can apply the model presented in chapter 2.2.7 to calculate the polarization of light after transmission through the sample.

The spectral dependence of the relative strength of Faraday rotation and non-reciprocal birefringence leads to a interesting phenomena one can call polarization nutation. To understand it one needs to understand the expected behaviour. For a fixed ratio of Faraday rotation and non-reciprocal birefringence, one would expect the Stokes vector of light to precess around the Stokes vector of the Eigenwaves [55] as the light propagates through the crystal. This leads to a periodic behaviour of the polarization with increasing delay. But in the crystal studied here both delay and ratio of Faraday rotation and linear birefringence depend on the energy of the transmitted light. Since this leads to a delay dependence of the eigenvectors the polarization is no longer just precessing, it is nutating. This results in a not purely periodic behaviour of the polarization with increasing delay.

4.3.5.1 Comparison with previous measurements

To check the validity of the excitonic model in section 2.2.7 one should apply it to previous measurements. Krichevtosov et al. [9] studied linear birefringence for detunings between $-63\,\text{meV}$ and $-440\,\text{meV}$ in pure CdTe. According to [8] their parameter A relates to the diagonal elements of the dielectric tensor by the following relation $(\varepsilon_{\text{dia}}/2) = Ak_zB_z = \gamma_2/2k_zB_z$. Calculating γ_2 using equation (2.36b) allows to extrapolate to these detunings.

The calculated $A = \gamma_2/2$ using equation (2.36b) and $V = 5 \times 10^{-12}$ eVcmT^{-1} is shown in Fig. 4-19 as a black line together with a red curve calculated for $V = 12 \times 10^{-12}$ eVcmT^{-1}. The measured values reported in [9] are represented by black dots in Fig. 4-19.

The curve calculated for $V = 5 \times 10^{-12}$ eVcmT^{-1}, which was determined in sec-

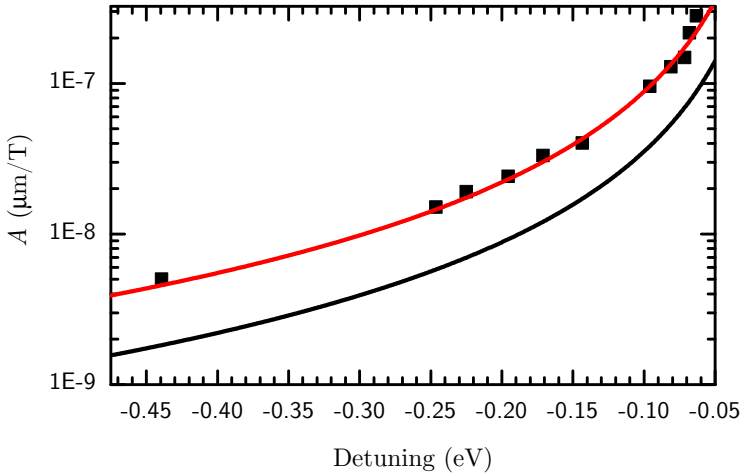

Figure 4-19: Spectral dependence of A, a constant describing the contribution of magneto-spatial dispersion to the dielectric tensor reported in [9]. The curves represent calculated spectral dependences of A using $A = \gamma_2/2$, where γ_2 is calculated according to equation (2.36b). The black and the red line represent calculations for $V = 5 \times 10^{-12}$ eVcmT^{-1} and $V = 12 \times 10^{-12}$ eVcmT^{-1}.

tion 4.3.4, is too low, but the one for $V = 12 \times 10^{-12}$ eVcmT^{-1} is in good agreement with the experimental data. One can deduce that the excitonic model is correct, because it describes the spectral dependence well. Difference in experimental techniques or sample can lead to the difference in the values of V. In [9] pure CdTe is investigated at lower magnetic fields in Voigt configuration. They also studied pure ZnTe. It showed almost no linear birefringence when compared to CdTe. Our sample is $Cd_{0.88}Zn_{0.12}Te$ which has a significant portion of Zn, leading to a weaker linear birefringence compared to pure CdTe.

4.3.6 Magnetic field dependence

Up to this point, the magnetic-field-induced anisotropy was only characterized for a single magnetic field of $B = 5\,\mathrm{T}$. To get a more complete understanding of the magnetic-field-induced optical anisotropy one needs to investigate the magnetic field dependence.

In Fig. 4-20(a) the measured delay dependence of the polarization of light leaving the 655 µm thick sample at $B = 7\,\mathrm{T}$ and $T = 1.8\,\mathrm{K}$ is represented by symbols. The light was $S_3 = 1$ polarized before entering the sample. The light is $S_3 = 1$ for the lowest delays, because the magneto spatial dispersion is too weak to convert it to S_2. With increasing delay the light is converted to S_2. At higher delays all three polarizations oscillate.

Fits of the experimental data are also shown in Fig. 4-20(a). The linear birefringence is characterized by $V = 5 \times 10^{-12}$ eVcmT^{-1} and this parameter was kept fixed. The contribution of the higher resonances to the Faraday rotation

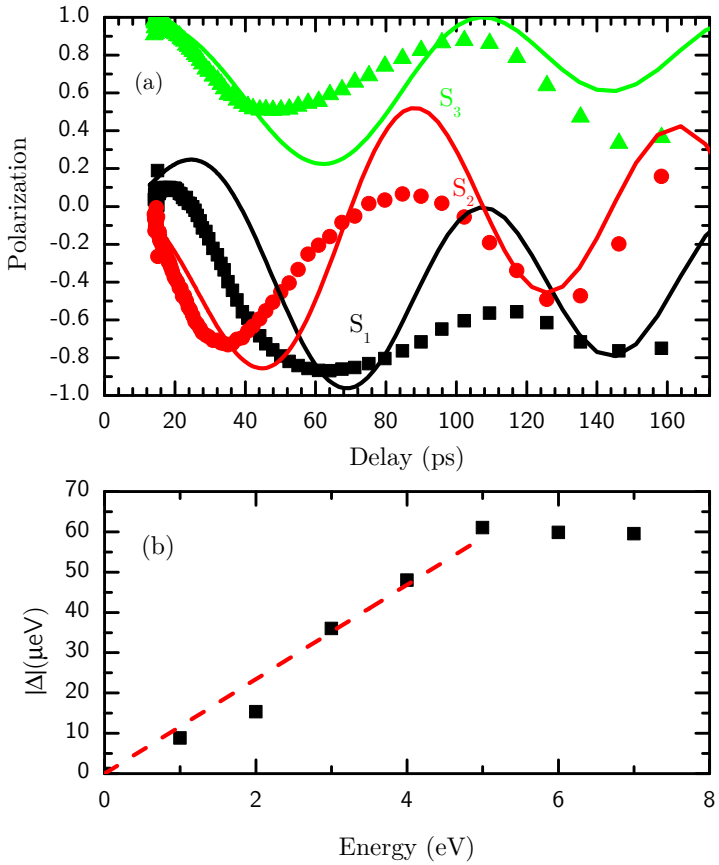

Figure 4-20: (a) Symbols: Measured polarization of transmitted light at $B = 7\,\mathrm{T}$ and $T = 1.8\,\mathrm{K}$ that was $S_3 = 1$ polarized before entering the sample. Lines: Calculated polarization for $V = 5 \times 10^{-12}$ eVcmT^{-1} and $\Delta = 60\,\mu\mathrm{eV}$. (b) Zeeman splitting extracted from fits where it was the only free parameter.

varies only slowly with energy, so one can include it by using a constant $\gamma_1' = 2.2 \times 10^{-4}\mathrm{T}^{-1}$. The Zeeman splitting Δ was the only parameter determined by fitting the curves to the data and is shown in Fig. 4-20. From $B = 0\,\mathrm{T}$ to $B = 5\,\mathrm{T}$ the Zeeman splitting increases linearly with magnetic field. For this region we can derive a g-factor of $|g_{exc}| = 0.2$. This value is comparable to the exciton g-factor estimated for bulk CdTe taking into account complex valence-band effects [56, 57, 58]. The calculations give either $|g_{exc}| \approx 0.1$, if the electron-hole exchange interaction is disregarded [58] or $|g_{exc}| \approx 0.35$ if electron-hole exchange is taken into account.

4.4 Conclusion

The propagation dynamics of exciton polaritons in a sub-mm thick (Cd,Zn)Te bulk crystal have been studied. The fundamental exciton resonance, though being inhomogeneously broadened by 1 meV, has only a small homogeneous broadening of 8 μeV. The resulting transparency for photons with an energy close to the exci-

ton resonance allows the observation of sub-nanosecond delay of light. This delay depends on the photon energy and leads to significant enhancement of magneto-optical effects if a magnetic field is applied. The magneto-optical effects were studied in Faraday configuration, where they manifest themselves in oscillations of the polarization state in the time domain, when a spectrally broad pulse is transmitted through the crystal. The frequency of these oscillations depends on the magnetic field and reaches 10 GHz at $B \sim 5$ T.

The effects leading to the oscillations of the polarization are identified as linear birefringence due to magneto-spatial dispersion and Faraday rotation (circular birefringence). Further, the presence of linear and circular dichroism for photon energies less than 10 meV below the exciton resonance has been shown. The linear birefringence and part of the Faraday rotation is due to the splitting of excitonic sublevels and can be predicted by a model assuming a split exciton resonance. The exciton Zeeman splitting leads to the Faraday rotation, and is determined even though the splitting is more than one order smaller than the inhomogeneous broadening. The exciton g-factor was evaluated to be $|g_{\mathrm{exc}}| = 0.2$, while the magneto-spatial dispersion constant is $V = 5 \times 10^{-12}$ eV cm T^{-1}.

The Faraday rotation has a non-trivial spectral dependence due to the contributions of several resonances. The contributions produce rotation in different directions leading to a sign change at photon energies close to the resonance. As a result, each spectral component of an optical pulse experiences a different anisotropy. The steep energy dependence of the relative strength of Faraday rotation and non-reciprocal birefringence lead to polarization nutation of the exciton polaritons. Nutation of the exciton polariton polarization is a quite interesting phenomenon, because it can be applied to manipulation of the polarization state of the transmitted light. The relative strength of linear and circular birefringence can be adjusted by active control of the energy of the exciton resonance.

Chapter 5

Exciton magnetic polaron dynamics

Exciton magnetic polarons in novel (Cd,Mn)Se/(Cd,Mg)Se quantum wells were already examined in my diploma thesis [59], where polaron formation was confirmed and unusual magnetic field dependences of the formation dynamics were discovered [60]. This work has been continued and new results challenge the explanation for the unusual dynamics. Further investigations resulted in a new and more complete explanation enhancing the understanding of this novel material.

This experimental work can be divided into three parts. First of all, the sample is introduced and characterized in subsection 5.1, which leads to the establishment of exciton magnetic polaron formation. Exciton magnetic polaron formation is confirmed in subsection 5.2 followed by the study of the exciton magnetic polaron formation dynamics in subsection 5.3. Finally, a conclusion is drawn.

5.1 Sample characterization

5.1.1 Sample description

The sample 1-372 has been grown in the group of S.V. Ivanov at the Ioffe Physical-Technical Institute in St. Petersburg by molecular beam epitaxy. It is a quantum well structure grown on top of an GaAs substrate. The first layer grown was a 0.4 µm thick buffer layer of $(Cd_{0.83},Mg_{0.17})Se$. This was followed by 5 periods of 9.7 nm thick $(Cd_{0.83},Mg_{0.17})Se$ barrier layers with of 3.8 nm thick $(Cd_{0.935},Mn_{0.065})Se$ quantum wells in between. A top layer of CdSe covers the structure for protection.

5.1.2 Magnetic field dependence of exciton energy

Sample 1-372 is a semimagnetic quantum as it contains manganese (Mn) ions. The concentration of MnSe is $x = 0.065$. Excitons forming at low temperatures in

quantum wells are strongly influenced by the presence of Mn ions. One effect is the giant Zeeman splitting. One would expect this splitting to increase linearly with concentration of Mn ions. But with increasing Mn concentration antiferromagnetic clusters are formed , where the spins of two Mn ions align antiparallel and compensate each other. This behavior is taken into account by an effective spin and an effective temperature in the modified Brillouin function, which is introduced in equation (2.40).

The giant Zeeman splitting affects the energy of the exciton. It can be studied by measuring the exciton energy at different magnetic fields. Reflection spectra a commonly used to determine the energy of an exciton resonance (see chapter 4.1.2 for a more detailed description).

Reflection spectra measured at magnetic fields up to $B = 7\,\mathrm{T}$ at a temperature of $T = 1.8\,\mathrm{K}$ are shown in figure 5-1. Due to the excitonic resonance every spectrum

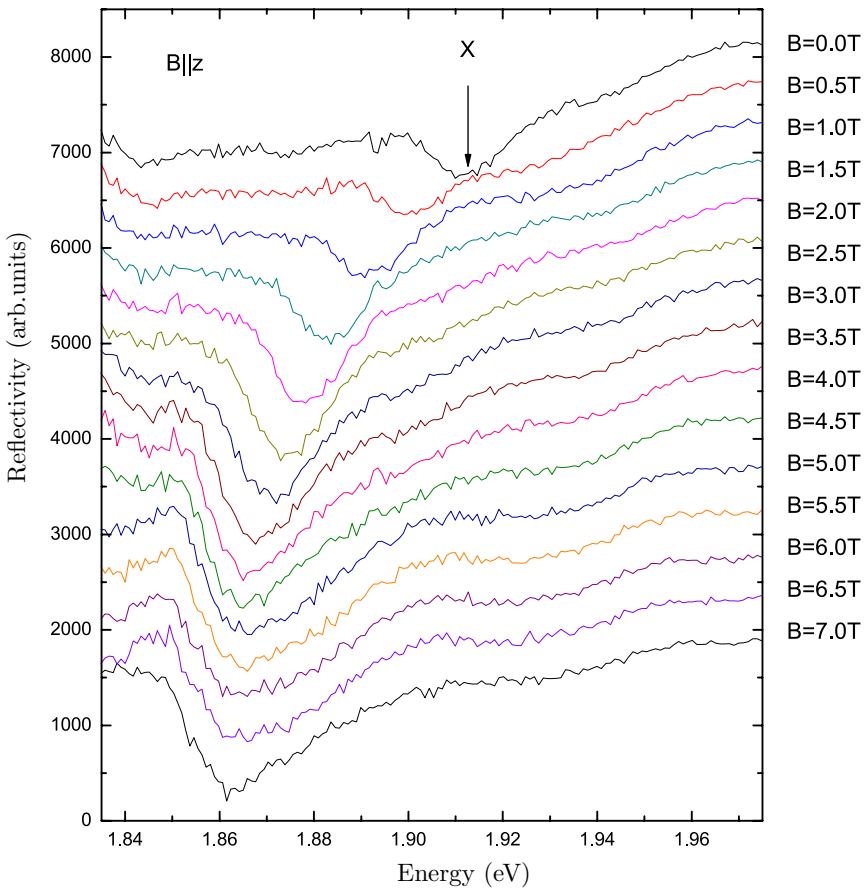

Figure 5-1: Magnetic field dependence of the reflection spectra of sample 1-372 taken at $T = 1.8\,\mathrm{K}$ [59].

shows a visible dip. The energy of this dip decreases with increasing magnetic field. Since the giant Zeeman splitting is larger than the width of the dip, it is sufficient to take the energy of the dip as the energy of the lower level of the Zeeman split

exciton resonance.

The excitonic resonance is the energy of the exciton when it is formed. It is shown for different magnetic fields in figure 5-2 as full black circles.

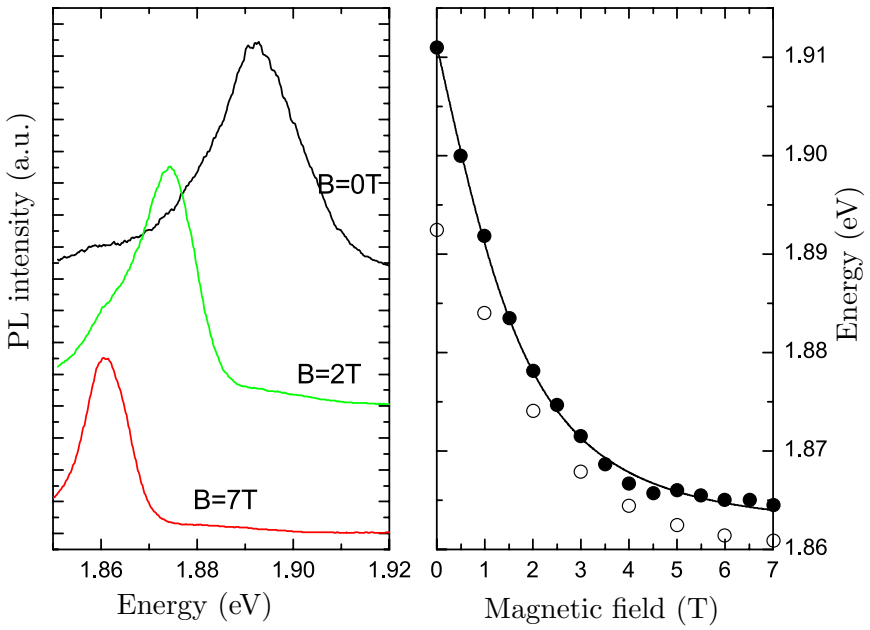

Figure 5-2: Left: PLspectra measured for sample 1-372 for different magnetic fields. Right: The exciton resonance energies measured at different magnetic fields are represented by black dots. The open circles represent the energy of the PL. The black line is a modified Brillouin-function(x =0.065, $T_0 = 1.46$ K, $S_{\text{eff}} = 1.09$) fitted to the measured exciton resonance energies [59].

The energy of the exciton resonance decreases from 1.913 eV at $B = 0$ T to about 1.872 eV at 3 T. The slope of the giant Zeeman splitting decreases with magnetic field and at $B = 7$ T the energy of the exciton resonance is 1.865 eV.

Moreover, the exciton energy can be determined by photoluminescence. Time-integrated PLspectra for $B = 0$ T, $B = 2$ T and $B = 7$ T are shown in the left part of figure 5-2. The energy of the PL is the energy of the exciton when it decays emitting a photon.

The giant Zeeman splitting can be described by a modified Brillouin-function as stated in equation (2.40). A calculated magnetic field dependence of the exciton energy at its formation is shown in the right part of figure 5-2. It has been calculated using the exchange integrals $N_0\alpha = 0.258$ eV and $N_0\beta = -1.110$ eV of bulk CdSe crystals [61]. The values of the effective spin $S_{\text{eff}} = 1.09$ and effective temperature $T = 1.46$ K have been derived by fitting equation (2.40) to the measured data. The calculated and measured magnetic field dependences are in good agreement.

There is a difference between the resonance energy determined using reflectivity

and the energy derived from PL measurements. This difference can be attributed to a Stokes shift of the exciton energy during the lifetime of the exciton. This shift decreases with magnetic field. It is 18 meV for $B = 0\,\mathrm{T}$ and 3 meV for $B = 7\,\mathrm{T}$.

This behaviour is consistent with an exciton magnetic polaron, where during its formation the exciton energy is reduced. Magnetic polaron formation can be suppressed with an external magnetic field. An external magnetic field aligns the Mn spins. In this case, the polaron cannot gain energy by aligning the Mn spins, because they are already aligned. One would expect, that it is suppressed at $B = 7\,\mathrm{T}$. The remaining shift of 3 meV is due to non-magnetic localization. In this case, one can attribute 15 meV to the localization due to the exciton magnetic polaron.

5.2 Confirmation of exciton magnetic polaron formation

5.2.1 Temperature dependence

The formation of an exciton magnetic polaron has been suggested in chapter 5.1.2. It gives an explanation for the difference between the energy necessary to generate an exciton and the energy of the exciton when it decays. This energy difference decreases with increasing magnetic field. This is consistent with the properties of an exciton magnetic polaron, as a magnetic field is one of the ways to suppress the formation of an exciton magnetic polaron.

As discussed in subsection 2.3.3, it is also possible to suppress the formation of an exciton magnetic polaron with temperature. This leads to an increase of energy the PL maximum (blue-shift) with increasing temperature. It is typical for exciton magnetic polaron formation at low temperatures.

To demonstrate this behaviour, three PL spectra taken at the temperatures of $T = 2\,\mathrm{K}$, $T = 8\,\mathrm{K}$ and $T = 15.5\,\mathrm{K}$ are shown in the left part of figure 5-3. These spectra were recorded without a magnetic field applied to the sample. The energy of the PL peak moves to higher energies with increasing temperature. To illustrate this further, the temperature dependence of the energy of maximum PL intensity is displayed in the right part of figure 5-3. The energy of the PL increases by 10 meV between 2 K and $T = 20\,\mathrm{K}$. This increase seems to asymptotically approach an energy of 1.899 eV.

This is in contrast to the expected dependence. One would expect the energy of the exciton to follow the energy of the band gap, which decreases with increasing temperature. This temperature dependence can be described by the Varshi

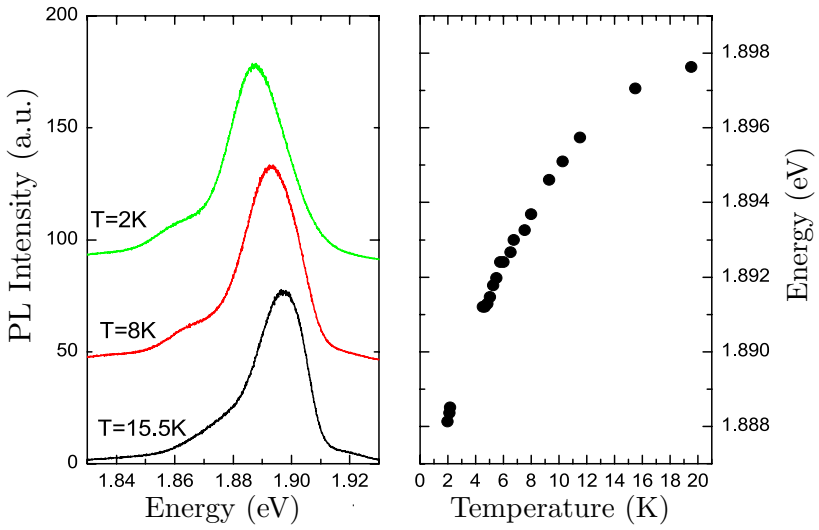

Figure 5-3: Left: PLspectra measured at $T = 2\,\mathrm{K}$, $T = 8\,\mathrm{K}$ and $T = 15.5\,\mathrm{K}$ without an external magnetic field. Right: Energy of the maximum PL intensity for temperatures between $T = 2\,\mathrm{K}$ and $T = 20\,\mathrm{K}$ [59].

equation

$$E_0(T) = E_0(0) - \frac{\alpha T^2}{\beta + T}. \tag{5.1}$$

For bulk CdSe, the parameters $\alpha = 6.396 \cdot 10^{-4}$ and $\beta = 281$ K of the Varshi equation are known [62] and one would expect, that the energy of the band gap decreases by 1.06 meV, when the temperature is increased from 2 K to 20 K. Therefore the obseved blue shift of the PL maximum with increasing temperature can not be explained by the temperature dependence of the band gap, so it must be due to an additional effect. It can be explained by the suppression of the exciton magnetic polaron formation. Since increasing the temperature suppresses the formation, the shift of the exciton energy during its lifetime is smaller. This leads to an increase of the PL energy, as it is the energy of the exciton at the end of its life.

5.2.2 Comparison with measurements of PL polarization

In the previous two chapters the typical behavior of an exciton magnetic polaron was observed. Though it is unlikely, this behavior could be produced by other effects. Another way to confirm the formation of an exciton magnetic polaron is to compare the measured energy shift to the one predicted by theory.

For an exciton mangetic polaron there is a relationship between the Zeeman splitting, the magnetic field dependence of the circular polarization of the PL and Stokes shift due to polaron formation. This relationship is further discussed in

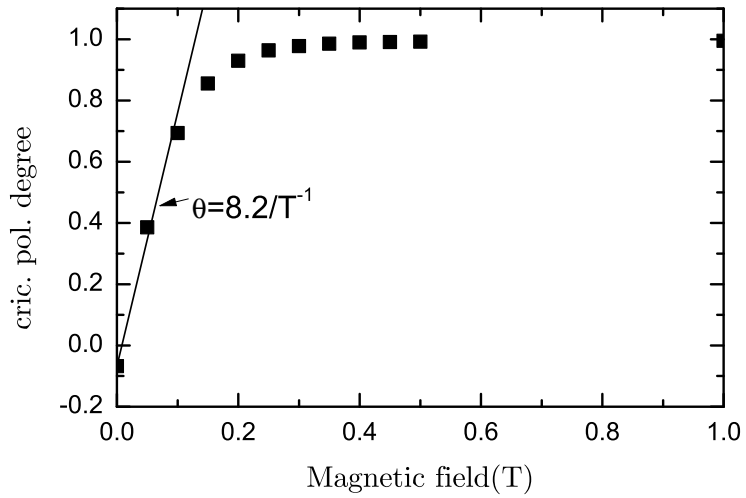

Figure 5-4: Magnetic field dependence of the circular PL polarization at $T = 1.8\,\mathrm{K}$ [59].

chapter 2.3.4.

The magnetic field dependence of the PL polarization is displayed in figure 5-4. There is almost no circular polarization without a magnetic field, but the light emitted at $B = 0.4\,\mathrm{T}$ is already completely polarized.

According to equation (2.54) the energy of the polaron induced Stokes shift, also called exciton magnetic polaron energy $E_{\mathrm{MP}} = \frac{1}{2\pi k_{\mathrm{B}} T}\frac{\gamma^2}{\theta^2}$, can be calculated using the slope $\gamma = 36\,\mathrm{meV\,T^{-1}}$ of the Zeeman splitting of the heavy hole at zero magnetic field and the slope $\theta = 8.2\,\mathrm{T^{-1}}$ of the circular polarization dependence on the magnetic field. The calculated polaron energy is 15 meV for a temperature of $T = 2\,\mathrm{K}$. This is in excellent agreement with the 15 meV difference in energy between the exciton resonance and the PL attributed to the formation of an exciton magnetic polaron.

5.3 Exciton polaron formation dynamics

An exciton magnetic polaron (EMP) is a excitonic quasi-particle. The hole of the exciton polarizes the Mn spins in its vicinity. The collective alignment of the Mn spin reduces the exciton energy. This process has its own dynamics and affects the dynamics of the exciton. A typical time-resolved PL spectrum of sample 1-372 is shown in figure 5-5(a) as a colour contour plot. It was acquired at a temperature of $T = 5\,\mathrm{K}$ without an external magnetic field applied. At $t = 0\,\mathrm{ns}$ an exciton population is generated using a laser pulse of about 1 ps duration with a photon energy of 2.06 eV. The first 2 ns of the evolution of the PL are shown. With time the PL decreases both in energy and in intensity.

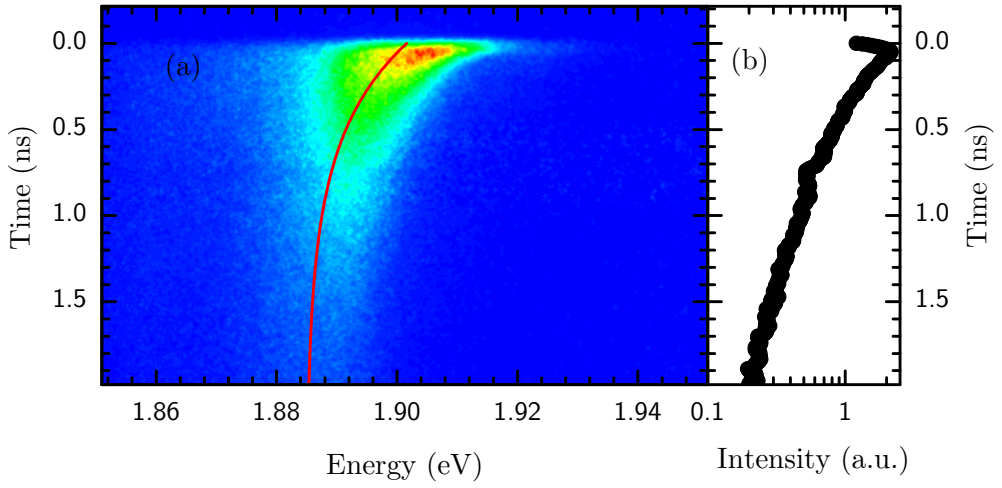

Figure 5-5: (a): Contour plot(red represents max. intensity, blue min. intensity) of a measured time-resolved PL spectrum taken at $T = 5\,\mathrm{K}$ and $B = 0T$ for sample I-372. Red line: Exponential curve describing the time evolution of the center energy of the PL. (b): Time evolution of the spectrally integrated intensity of the PL.

The evolution of the energy of the PL maximum, $E(t)$, can be described by an exponential function

$$E(t) = \delta E e^{-\frac{t}{\tau_\mathrm{f}}} + E_\infty. \tag{5.2}$$

Here δE is the localization energy, while E_∞ is the energy of the equilibrium state. The speed of the formation is given by the formation time τ_f. The red curve shown in figure 5-5(a) was calculated for $\delta E = 16.7\,\mathrm{meV}$, $E_\infty = 1.885\,\mathrm{eV}$ and $\tau_\mathrm{f} = 537\,\mathrm{ps}$ and is in good agreement with the experimental data shown in 5-5(a), which was acquired at a temperature of $T = 5\,\mathrm{K}$ without a magnetic field applied.

To investigate the recombination dynamics, the transient of the PL intensity is used. The spectrally integrated intensity of PL , which was measured at a temperture of $T = 5\,\mathrm{K}$ without a magnetic field applied, is shown in figure 5-5(b) in a logarithmic plot. Due to the limited lifetime τ_l of the exciton the intensity of the PL reads

$$I(t) = I_0 e^{-\frac{t}{\tau_\mathrm{l}}}. \tag{5.3}$$

5.3.1 Magnetic field dependence of the EMP formation dynamics

During its lifetime the exciton will loose energy if an exciton magnetic polaron is formed. This process approaches an equilibrium state. The energy difference between the energy $E(t = 0)$ during excitation and the equilibrium energy is the localization energy δE.

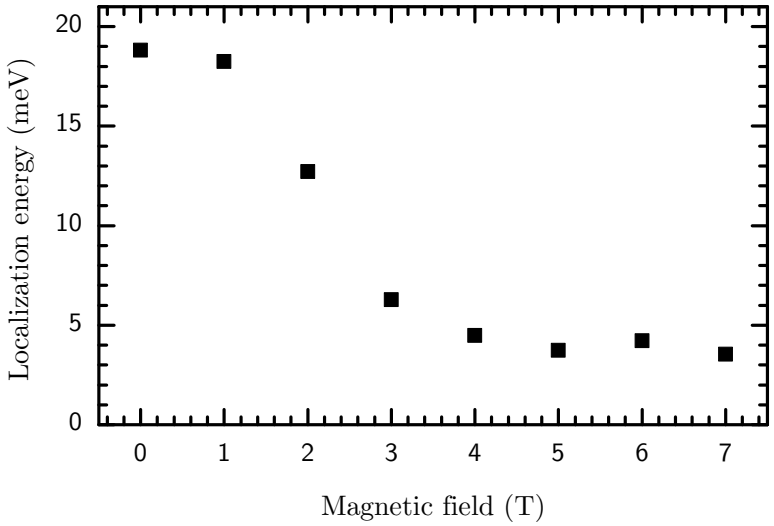

Figure 5-6: Magnetic field dependence of the localization energy δE measured at a Temperature of $T = 2\,\mathrm{K}$ in Faraday geomerty.

Application of an external magnetic field reduces the shift of the exciton energy due to exciton magnetic polaron formation. This can be observed by studying the magnetic field dependence of the localization energy δE, which is shown in figure 5-6. It has been measured for a temperature of $T = 2\,\mathrm{K}$ and the magnetic field was applied in Faraday geometry.

The localization energy is 19 meV in the absence of an external magnetic field. It is 18 meV for $B = 1\,\mathrm{T}$ and then decreases down to $\approx 4\,\mathrm{meV}$ for magnetic fields above 4 T. The formation of an exciton magnetic polaron is suppressed for $B > 4\,\mathrm{T}$. If it was not suppressed, the localization energy would decrease further with magnetic field.

The localization energy of 4 meV for $B > 4\,\mathrm{T}$ is due to non-magnetic localization. Due to fluctuations in the composition of the quantum well layer and its width the exciton can reduce its energy by moving to more favorable positions. As the non-magnetic localization is constant for $B \geq 4\,\mathrm{T}$ one can assume that the energy of the exciton magnetic polaron is $E_{\mathrm{MP}} = 15\,\mathrm{meV}$. This energy is comparable to the values determined by continuous wave measurements.

The dynamics of the exciton is shown in figure 5-7. The formation time is $\tau_{\mathrm{loc}} = 600\,\mathrm{ps}$ in the absence of an external magnetic field, which is rather slow. According to ref. [11], the usual formation time of an exciton magnetic polaron in CdTe is below 200 ps. It increases to about 800 ps for $B = 1\,\mathrm{T}$ and $B = 2\,\mathrm{T}$. With further increase the localization time decreases. It is about 300 ps for magnetic fields $B \geq 5\,\mathrm{T}$. This time can be attributed to the non-magnetic localization.

The non-monotonic behaviour of the localization time with magnetic field is unusual. One would expect the observed localization time to steadily change from the EMP localization time to the localization time of the non-magnetic localization

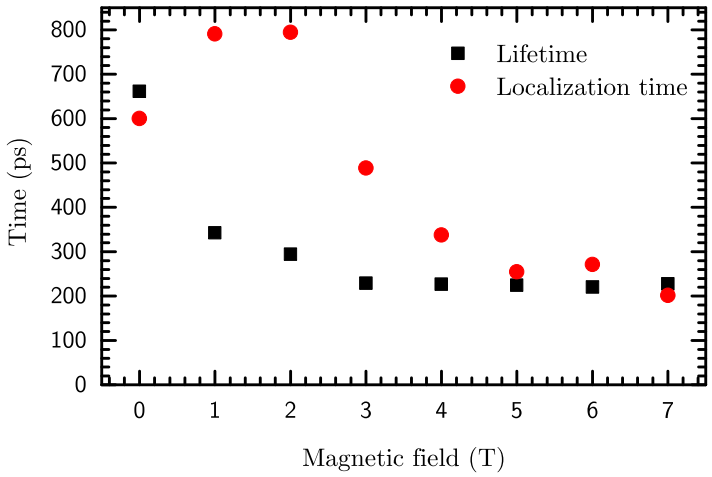

Figure 5-7: Magnetic field dependence of the localization time and exciton lifetime measured for $T = 2\,\mathrm{K}$ using fields in Faraday configuration.

when an external magnetic field is applied. Moreover, the exciton lifetime, shown in figure 5-7, drops with increasing magnetic field. The lifetime is $\tau_\mathrm{l} = 660\,\mathrm{ps}$ without an applied magnetic field. It decreases to 340 ps at $B = 1\,\mathrm{T}$ and is 230 ps for magnetic fields above $B \geq 3\,\mathrm{T}$.

A simple explanation for both peculiarities is a weak or absent hole localization inside the quantum well without magnetic field applied. The lifetime of an exciton is inversely proportional to the overlap of the hole and electron wavefunction [63], because the exciton can only recombine if the electron can take the place of the hole. When most of the hole wavefunction is inside the barrier and the electron is confined to the quantum well, the lifetime is long due to a small overlap of the two wavefunctions. Such a quantum well is a type-II structure, as the material energetically most favourable for the electron is not the one most favourable for the hole. When a magnetic field is applied the giant Zeeman splitting makes the quantum well energetically more favorable for the hole. Due to this a larger part of the hole function is inside the quantum well increasing the overlap and decreasing the lifetime.

If a larger part of the hole wavefunction is inside the quantum well, the Mn spin can decrease the energy of the exciton further, because most of the giant Zeeman splitting is due to exchange interaction between the 3d electrons of the Mn ions and the heavy hole. Accordingly, an increase in the proportion of the hole wavefunction inside the quantum well leads to a decrease of exciton energy. This results in additional localization energy which explains the small difference between the localization energies of $B = 0\,\mathrm{T}$ and $B = 1\,\mathrm{T}$.

It can also have effects on the formation dynamics. An increase in the potential well depth will increase the density of the wavefunction. This allows a stronger alignment of the Mn spins, which in turn makes the quantum well even more

favorable for the hole. This effect is known as autolocalization and it leads to an increase of formation time.

5.3.2 Effects of a Voigt magnetic field

The proposed explanation of the effects of a magnetic field on an exciton magnetic polaron in Faraday configuration depends on the hole wavefunction properties and its confinement within the quantum well layer in the absence of a magnetic field.

The influence of Voigt and Faraday fields on the energy of a heavy hole is very different when the hole is confined inside the quantum well. The confinement leads to a strong anisotropy of the heavy hole g-factor [64]. While there is a giant Zeeman splitting in Faraday configuration (see Chapter 5.1.2), there is no Zeeman splitting for Voigt geometry unless fields of several Tesla are applied [65].

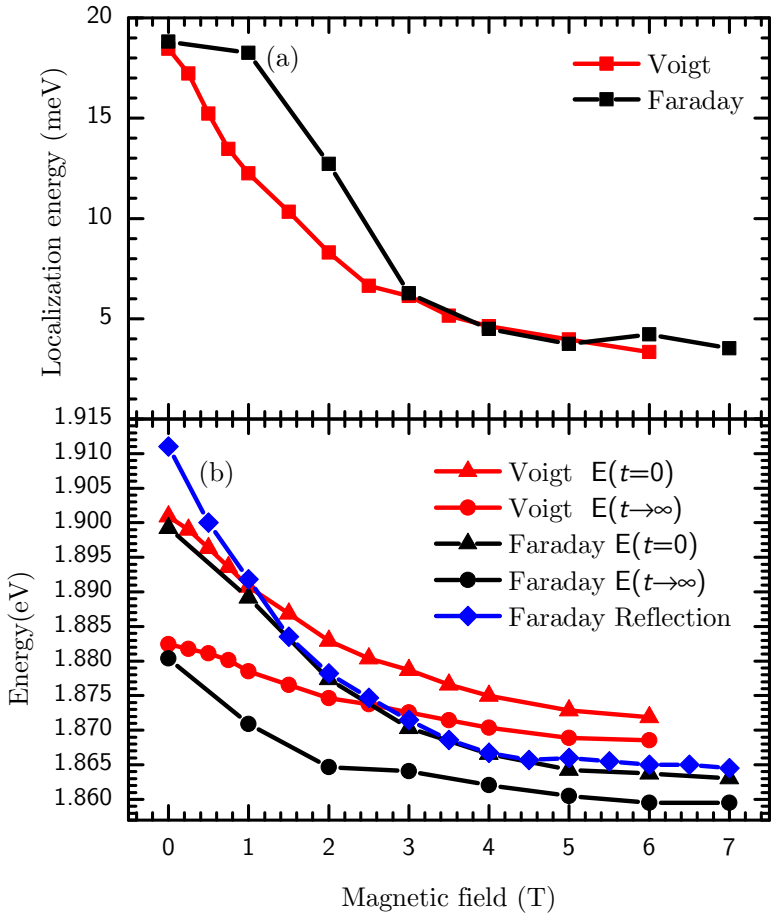

Figure 5-8: (a): Magnetic field dependence of the localization energy for Voigt and Faraday configuration. (b): Magnetic field dependence of the PL energy at the beginning of the decay $E(t = 0)$ and for the equilibrium energy $E(t \to \infty)$ for Faraday and Voigt configureation together with the exciton energy determined using reflection spectra in Faraday configuration. These measurements were performed at a temperature of $T = 2\,\mathrm{K}$.

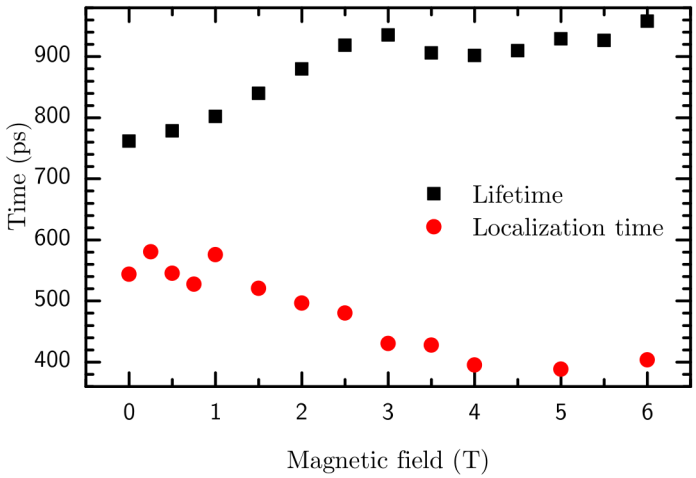

Figure 5-9: Magnetic field dependence of the exciton lifetime and the localization time in Voigt geomeetry. These measurements were performed at a temperature of $T = 2\,\mathrm{K}$.

In figure 5-8(b) the magnetic field dependence of the initial exciton energy $E(t = 0)$ and the equilibrium energy $E(t \to \infty)$ are shown for Faraday and Voigt geometries. Also, the energy of the exciton resonance is shown. It has been determined by reflection measurements for Faraday magnetic fields. The energy of the exciton resonance and $E(t = 0)$ for Faraday geometry are in good agreement except a deviation at $B = 0\,\mathrm{T}$. This makes $E(t = 0)$ a subtle indicator of the Zeeman splitting. For a magnetic field $B \leq 2\,\mathrm{T}$ there is little difference between the results measured in Voigt and Faraday geometries. In Faraday geometry the Zeeman splitting increases stronger ($36\,\mathrm{meV}$ at $B = 6\,\mathrm{T}$), than that in Voigt geometry ($29\,\mathrm{meV}$ at $B = 6\,\mathrm{T}$), but the difference is small when compared to the average value of the Zeeman splitting.

The Zeeman splitting is isotropic for magnetic fields $B \leq 2\,\mathrm{T}$, which confirms, that the hole is not strongly confined without an external magnetic field. For magnetic fields $B > 2\,\mathrm{T}$ the Zeeman splitting is anisotropic and is bigger in Zeeman configuration. This indicates that at higher magnetic fields the hole is more confined to the quantum well. Also $E(t \to \infty)$ is anistropic even at low magnetic field. Even at magnetic fields of $B = 1\,\mathrm{T}$ there is a difference of $10\,\mathrm{meV}$ in $E(t \to \infty)$. This anisotropy is more pronounced as the EMP formation leads to the localization of the hole into the quantum well. This localization makes the Zeeman splitting more anisotropic.

For a more complete understanding the dynamics of the exciton and EMP can be studied. The exciton lifetime and localization time in Voigt geometry are shown in figure 5-9. In contrast to Faraday configuration, in Voigt geometry the lifetime of the exciton does not decrease with magnetic field, but it increases from $\tau_\mathrm{l} = 760\,\mathrm{ps}$ at $B = 0\,\mathrm{T}$ to $\tau_\mathrm{l} = 960\,\mathrm{ps}$ at $B = 6\,\mathrm{T}$. In Faraday geometry the decrease of lifetime can be explained by the increase of the overlap of electron and hole wavefunction when the hole is confined to the quantum well. As the

lifetime does not decrease with an increasing magnetic field in Voigt geometry, one can assume, that a magnetic field does not lead to strong confinement of the hole to the quantum well in voigt geometry. The confinement of the hole in Faraday geometry is a result of the Zeeman splitting of the hole. This is not possible in Voigt geometry, where, because of the g-factor anisotropy on a confined hole, the Zeeman splitting is smaller if the hole is confined. If the Zeeman splitting would induce confinement, this confinement would reduce the Zeeman splitting. This interaction reduces both the Zeeman splitting and the confinement.

The small increase of lifetime between $B = 0\,\mathrm{T}$ and $B = 3\,\mathrm{T}$ could be explained by the suppression of EMP formation. If EMP formation leads to localization of the hole to the quantum well, suppresion of the EMP formation will cancel this localization and lead to a longer lifetime.

The localization time also changes weakly with magnetic field. It decreases from $\tau_\mathrm{f} = 600\,\mathrm{ps}$ at $B = 7\,\mathrm{T}$ to $\tau_\mathrm{f} = 500\,\mathrm{ps}$ at $B = 6\,\mathrm{T}$. This is also in contrast to the localization time in Faraday geometry. In Faraday geometry the localization time increases from 600 ps at $B = 0\,\mathrm{T}$ to 800 ps at $B = 1\,\mathrm{T}$ and $B = 2\,\mathrm{T}$. This increase in localization time was attributed to autolocalization, where, due to the EMP formation, a bigger part of the hole wavefunction is confined to the quantum well extending the formation process. This increase is missing in Voigt geomerty, as in this configuration the magnetic field does not lead to a confinement of the hole function.

5.4 Conclusion

The quantum well structure studied is made from the diluted magnetic semiconductor (Cd,Mn)Se. The Mn inside the quantum well induces giant Zeeman splitting, which reduces the energy on one excitonic level by up to 50 meV. This Zeeman splitting is isotropic for magnetic fields $B \leq 2\,\mathrm{T}$, which indicates that the heavy hole is only weakly confined in the absence of magnetic fields. This giant Zeeman splitting can increase the band offset for heavy holes leading to a increase of the holes confinement as evident by the threefold reduction of exciton lifetime for magnetic fields $B \geq 1\,\mathrm{T}$ applied in Faraday configuration. The magnetic field induced confinement is demonstrated by the anisotropy of the Zeeman splitting for magnetic fields $B > 2\,\mathrm{T}$.

At temperatures $T < 20\,\mathrm{K}$ and magnetic fields $B \leq 4\,\mathrm{T}$ exciton magnetic polaron formation can be observed. The energy of the magnetic polaron is about 15 meV and the formation time is $\tau_\mathrm{f} = 600\,\mathrm{ps}$ without an external magnetic field. Exciton magnetic polaron formation also induces a stronger confinement of the hole to the quantum well, which allows stronger interaction of the hole with the Mn spin. This autolocalization extends the formation time to about $\tau_\mathrm{f} = 800\,\mathrm{ps}$,

if a magnetic field between 1 T and 2 T is applied in Faraday configuration. This has been confirmed by measurements in Voigt geometry, where the magnetic field suppresses the extension of the formation time due to autolocalization.

Chapter 6

Conclusion

In this work two types of excitonic quasi-particles were studied. Exciton polaritons, the first type, are propagating states formed by photons interacting with excitonic resonances. The second type are exciton magnetic polarons which are formed by the sp-d exchange interaction of an heavy-hole exciton with localized manganese spins leading to a collective alignment of the manganese spins and a reduction of the exciton energy.

The propagation dynamics of exciton polaritons were studied in a sub-mm thick (Cd,Zn)Te bulk crystal using polarimetric time of flight techniques. Due to exciton polariton formation between a photon and the fundamental exciton resonance, the propagation speed of light decreases continuously as the photon energy approaches the energy the fundamental exciton resonance. The maximum observed delay of 350 ps was measured for a 655 µm thick crystal, and corresponds to a reduction of the propagation speed by a factor of 150.

The magnetic field induced splitting of the exciton resonance gives rise to magneto-optical effects if a magnetic field is applied. In Faraday configurations oscillations of the polarization state in the time domain were observed, when a initially linear polarized spectrally broad pulse was transmitted through the crystal. The frequency of these oscillations depends on the magnetic field and reaches 10 GHz at $B \sim 5$ T. Four magnetic field induced polarization effects , Faraday rotation, linear birefringence due to magneto-spacial dispersion, and linear and circular dichroism, were identified, characterized and explained by a theoretical model assuming polariton formation by a Zeeman split exciton resonance. Using this model it was possible to determine the exciton g-factor of $|g_{\mathrm{exc}}| = 0.2$ and the magneto-spatial dispersion constant of $V = 5 \times 10^{-12}$ eV cm T^{-1}, even though the exciton Zeeman splitting is orders of magnitude smaller than the inhomogeneous broadening.

Further, higher energy transitions also induce Faraday rotation leading to a non trivial energy dependence of the optical anisotropy and the observation of pure

linear birefringence. When using the Poincaré sphere to describe the anisotropy, both linear birefringence and Faraday rotation induce as a rotation of the Stokes vector around a vector defined by the relative strength of the two effects. The change of this rotation vector with increasing delay can be called polarization nutation.

Exciton magnetic polaron (EMP) formation has been studied in a (Cd,Mn)Se-/(Cd,Mg)Se quantum well structure, where it was observed for magnetic fields be below $B = 4\,\mathrm{T}$ and temperatures below $T = 20\,\mathrm{K}$. The reduction of the exciton energy due to EMP formation is up to 15 meV at $T = 2\,\mathrm{K}$ and B=0 T. The EMP formation dynamics are slow (650 ps) compared to more standard systems, such as CdTe(150-200ps) [11] and is even slower with magnetic field between $B = 1\,\mathrm{T}$ and $B = 2\,\mathrm{T}$ applied. This slowing down can be attributed to autolocilization, which is described below.

The excitons hole is not confined strongly to the Mn containing quantum well without an magnetic field applied, can be confined by the application of an external magnetic field The Mn induced giant Zeeman splitting reduces the exciton energy by up to 50 meV at $B = 7\,\mathrm{T}$ and increases the valance-band offset leading to a stronger confinement of the hole. Similarly EMP formation also reduces the exciton energy and induces a stronger hole confinement. Further the reduction of the exciton energy due to EMP formation increases with increasing confinement of the hole to quantum well. This leads to a positive feedback loop extending EMP formation time and increasing exciton energy reduction due to EMP formation. Experimentally the assumption of a magnetic field induced confinement is confirmed by a magnetic field induced anisotropy of the excitons g-factor and the magneitic field induced reduction of excitons lifetime by a factor of 3.

Chapter 7

Acknowledgements

First I would like to express my gratitude towards Prof. Manfred Bayer for providing the means to conduct such a variety of studies.

I would like to thank Dr. Ilya Akimov for supervising me and guiding me through my work. I really appreciate the patience and thought invested in my work during both my thesis and diploma.

Further I would like to thank Prof. Dima Yakovlev for the possibility to work with several great scientists, his insight and ability to put things in relation, while giving me the freedom to follow unexpected experimental results.

I am also grateful towards Dr. Mikhail M. Glazov for the time invested in providing me with a better understanding of exciton polariton effects, and Prof. Dr. Hans Jürgen Weber for his thought provoking insight into polarization effects in zincblende structure crystals.

I also sincerely appreciate Dr. Jörg Debus and Dr. Alexander Greilich for sharing their understanding of spin physics.

I would like to thank Jasmin Jäger, Dr. Jörg Debus, Dr. Christian Brüggemann and Michael Bombeck for their help in preperation of my thesis. Further I really need to thank most of my colleagues in E2 for proofreading the thesis.

I would also like to thank my family for supporting me and especially my mother for motivating me to take up science and showing me how to uphold this motivation. Further I do not believe that I would study physics if it wasn't for my physics teacher Mr. Tarwit who had an inspiring love for it.

Also I would like to mention the support of my friends and colleges that carried me through my PhD.

Chapter 8

Appendix

8.1 Calculating the dielectric function of an inhomogeneously broadened exciton with spatial dispersion

This is a description of the numerical algorith used to calculate the dielectric function of an inhomogeneously broadened exciton with spatial dispersion.

- Equation (2.8) was solved for $\varepsilon_B = 11.2$ [47], $\hbar\omega_{LT} = 0.65\,\text{eV}$ [47], $M = 1.5m_0$ [47] where m_0 is the free electron mass, $\hbar\Gamma = 8\,\mu\text{eV}$ and $\hbar\omega_0 = 1.6644\,\text{eV}$ yielding the upper(UP) and lower polariton(LP) branch dispersion.

- From the dispersions one calculates the refractive indexes of the UP and LP branches and derives the effective refractive index $\bar{n}$ using equation (2.9).

- The effective dielectric function $\bar{\varepsilon}(\omega)$ for an exciton without inhomogeneous broadening is $\bar{\varepsilon}(\omega) = \bar{n}(\omega)^2$. One can introduce the inhomogeneous broadening $\Gamma_{\text{inh}} = 1\,\text{meV}$ by numerically convoluting* $\bar{\varepsilon}(\omega)$ with an Gaussian distribution. The dielectric function $\varepsilon(\omega)$ was calculated as

$$\varepsilon(\omega) = \int_{-10\,\text{meV}/\hbar}^{10\,\text{meV}/\hbar} \bar{\varepsilon}(\omega+\omega') \frac{\exp\left[-\frac{(\omega')^2}{2\Gamma_{\text{inh}}^2}\right]}{\sqrt{2\pi}\Gamma_{\text{inh}}} d\omega'.$$

*It is impossible to integrate from $-\infty$ to ∞ numerically. The limits $-10\,\text{meV}/\hbar$ to $10\,\text{meV}/\hbar$ contain almost the complete Gaussian distribution. This provides it a very good approximation.

8.2 Calculating the Stokes vector for a given incident polarization and dielectric tensor

According to section 2.2.4, the dielectric tensor ε_{ij} can be divided into three contributions. ε_i is the dielectric constant for the isotropic case, while ε_{dia} and ε_{off} are the contributions to the diagonal and off-diagonal elements of ε_{ij}.

The following algorithm was used to calculate the Stokes vector after propagation through the sample for linearly polarized light. The angle between the direction of the linear polarization and $\vec{x}$ is α.

- The isotropic dielectric constant ε_i is assumed to be included in the inhomogeneously broadened simplified model presented in equation (2.12).
- The amplitudes of the eigenwaves can be calculated by

$$A_1 = \frac{2\mathrm{i}\varepsilon_{off}\cos\alpha + \left(\varepsilon_{dia} + \sqrt{\varepsilon_{dia}^2 + 4\varepsilon_{off}^2}\right)\sin\Theta}{2\sqrt{\varepsilon_{dia}^2 + 4\varepsilon_{off}^2}} \tag{8.1}$$

$$A_2 = \frac{-2\mathrm{i}\varepsilon_{off}\cos\alpha + \left(-\varepsilon_{dia} + \sqrt{\varepsilon_{dia}^2 + 4\varepsilon_{off}^2}\right)\sin\Theta}{2\sqrt{\varepsilon_{dia}^2 + 4\varepsilon_{off}^2}}. \tag{8.2}$$

- The eigenvectors $\vec{E}_{1,2}$ and eigenvalues are calculated using equations (2.16) and (2.17).
- The electric field after propagation is calculated by equation (2.18).
- Finally, the Stokes vector is calculated from the electric field using equations (2.22).

8.3 Calculating S_2 for eigenpolarization of a single exciton resonance

According to equations (2.35) and (2.36), for a single exciton resonance with no additional contributions ($\gamma_1' = 0$), the arguments $\varphi_{\text{off}} = \arg(\varepsilon_{\text{off}})$ and $\varphi_{\text{dia}} = \arg(\varepsilon_{\text{dia}})$ of the diagonal and off-diagonal elements of the dielectric tensor have only a neglectable difference as long as $\Im(k_z) \ll \Re(k_z)$. In this case ($\varphi_{\text{dia}} = \varphi_{\text{off}} = \varphi_{\text{c}}$), one can write equation (2.16) as

$$\begin{aligned}\vec{E_{1,2}} &= \begin{pmatrix} \frac{\mathrm{i}(|\varepsilon_{\text{dia}}|e^{\mathrm{i}\varphi_{\text{c}}} \mp \sqrt{|\varepsilon_{\text{dia}}^2|+4|\varepsilon_{\text{off}}|^2}e^{\mathrm{i}\varphi_{\text{c}}})}{2|\varepsilon_{\text{off}}|e^{\mathrm{i}\varphi_{\text{c}}}} \\ 1 \end{pmatrix} \\ &= \begin{pmatrix} \frac{\mathrm{i}(|\varepsilon_{\text{dia}}| \mp \sqrt{|\varepsilon_{\text{dia}}^2|+4|\varepsilon_{\text{off}}|^2})}{2|\varepsilon_{\text{off}}|} \\ 1 \end{pmatrix}.\end{aligned}$$

According to equation (2.24b) S_2 is calculated as

$$S_2 = \frac{\Re(E_x E_y^*)}{|E_x|^2 + |E_y|^2}.$$

Because E_x of $\vec{E_{1,2}}$ is completely imaginary and E_y completely real the eigenwaves are not polarized in $S_2(S_2(\vec{E_{1,2}}) = 0)$.

Bibliography

[1] M.D. Surge. "Excitons". In: ed. by E. I. Rashba. North-Holland Publishing Company, Amsterdam; New York; Oxford, 1982. Chap. Introduction, pp. 3–15.

[2] E.L. Ivchenko. "Excitons". In: ed. by E. I. Rashba. North-Holland Publishing Company, Amsterdam; New York; Oxford, 1982. Chap. Spatial dispersion effects in the exciton resonance region, pp. 141–176.

[3] H. Deng, H. Haug, and Y. Yamamoto. "Exciton-polariton Bose-Einstein condensation". In: *Rev. Mod. Phys.* 82.2 (2010), pp. 1489–1537. DOI: 10.1103/RevModPhys.82.1489.

[4] J. Kasprzak et al. "Bose-Einstein Condensation of Exciton Polaritons". In: *Nature* 443 (2006), p. 409. DOI: 10.1038/nature05131.

[5] S. H. Wemple and M. DiDomenico. "Behavior of the Electronic Dielectric Constant in Covalent and Ionic Materials". In: *Phys. Rev. B* 3 (4 Feb. 1971), pp. 1338–1351. DOI: 10.1103/PhysRevB.3.1338.

[6] Xinyu Liu and J. K. Furdyna. "Optical dispersion of ternary {II − VI} semiconductor alloys". In: *Journal of Applied Physics* 95.12 (June 2004), pp. 7754–7764. ISSN: 00218979. DOI: doi:10.1063/1.1739291. URL: http://jap.aip.org/resource/1/japiau/v95/i12/p7754_s1 (visited on 07/13/2012).

[7] M. Zvára, F. Žaloudek, and V. Prosser. "Interband Faraday Effect in CdTe Single Crystals". en. In: *physica status solidi (b)* 16.1 (1966), K21–K24. ISSN: 1521-3951. DOI: 10.1002/pssb.19660160141.

[8] B. B. Krichevtsov et al. "Magnetospatial dispersion effect in magnetic semiconductors $Cd_{1-x}Mn_xTe$". In: *Phys. Rev. B* 57 (23 June 1998), pp. 14611–14614. DOI: 10.1103/PhysRevB.57.14611.

[9] B. B. Krichevtsov et al. "Manifestation of magnetically induced spatial dispersion in the cubic semiconductors ZnTe, CdTe, and GaAs". In: *Journal of Experimental and Theoretical Physics Letters* 69.7 (Apr. 1999), pp. 551–557. ISSN: 0021-3640, 1090-6487. DOI: 10.1134/1.568066.

[10] "Introduction to the physics of diluted magnetic semiconductors". English. In: Heidelberg; New York: Springer, 2010. Chap. Introduction. ISBN: 9783642158568 3642158560.

[11] G. Mackh et al. "Localized exciton magnetic polarons in $Cd_{1-x}Mn_xTe$". In: *Phys. Rev. B* 49 (15 Apr. 1994), pp. 10248–10258. DOI: 10.1103/PhysRevB.49.10248.

[12] D. R. Yakovlev. "Two dimensional magnetic polarons in semimagnetic quantum well structures". In: *Festkörperprobleme 32*. Vol. 32. Berlin, Heidelberg: Springer Berlin Heidelberg, pp. 251–264. ISBN: 978-3-528-08040-2.

[13] B Ray. *II-VI Compounds*. Pergamon Press, Qxford, 1969.

[14] Ben Mills. *Sphalerite-unit-cell-depth-fade-3D-balls*. 2006. URL: http://en.wikipedia.org/wiki/File:Sphalerite-unit-cell-depth-fade-3D-balls.png.

[15] *Tetrahedral symmetry*. en. Page Version ID: 557458692. May 2013. URL: http://en.wikipedia.org/w/index.php?title=Tetrahedral_symmetry&oldid=557458692 (visited on 07/11/2013).

[16] James R. Chelikowsky and Marvin L. Cohen. "Nonlocal pseudopotential calculations for the electronic structure of eleven diamond and zinc-blende semiconductors". In: *Phys. Rev. B* 14 (2 July 1976), pp. 556–582. DOI: 10.1103/PhysRevB.14.556.

[17] D. E. Eastman et al. "Photoemission spectroscopy using synchrotron radiation. I. Overviews of valence-band structure for Ge, GaAs, GaP, InSb, ZnSe, CdTe, and AgI". In: *Phys. Rev. B* 9 (8 Apr. 1974), pp. 3473–3488. DOI: 10.1103/PhysRevB.9.3473. URL: http://link.aps.org/doi/10.1103/PhysRevB.9.3473.

[18] R. J. Nelmes et al. "Observation of a high-pressure cinnabar phase in CdTe". In: *Phys. Rev. B* 48 (2 July 1993), pp. 1314–1317. DOI: 10.1103/PhysRevB.48.1314.

[19] V. Esch et al. "State filling, Coulomb, and trapping effects in the optical nonlinearity of CdTe quantum dots in glass". In: *Phys. Rev. B* 42 (12 Oct. 1990), pp. 7450–7453. DOI: 10.1103/PhysRevB.42.7450. URL: http://link.aps.org/doi/10.1103/PhysRevB.42.7450.

[20] A. Waag et al. "Molecular beam epitaxial growth of ultrathin CdTe-CdMnTe quantum wells and their characterization". In: *Applied Physics Letters* 59.23 (1991), pp. 2995–2997.

[21] S. I. Pekar. In: *Sov. Phys. JETP* 6 (1958), p. 785.

[22] J. J. Hopfield. "Theory of the Contribution of Excitons to the Complex Dielectric Constant of Crystals". In: *Physical Review* 112 (5 Dec. 1, 1958), pp. 1555–1567. DOI: 10.1103/PhysRev.112.1555. URL: http://link.aps.org/doi/10.1103/PhysRev.112.1555 (visited on 11/17/2013).

[23] L. D. Landau and E. M. Lifschitz. *Klassische Feldtheorie*. Ed. by Paul Ziesche. Vol. II. Lehrbuch der theoretischen Physik. Akademie Verlag, Berlin, 1992, pp. 128–141.

[24] E. Hecht and A. Zajac. "Polarization". In: *Optics*. Addison-Wesley Publishing Company, Reading, 1974.

[25] M. J. Walker. "Matrix Calculus and the Stokes Parameters of Polarized Radiation". In: *American Journal of Physics* 22 (Apr. 1954), pp. 170–174. DOI: 10.1119/1.1933670.

[26] D Goldstein. "Polarized Light". In: 2nd ed. Mark Dekker Inc., New York, 203. Chap. 4. ISBN: 0-8247-5053-X.

[27] S. I. Pekar. In: *Zh. Eksp. Teor. Fiz.* 16 (1946), p. 335.

[28] J. K. Furdyna. "Diluted magnetic semiconductors". In: *Journal of Applied Physics* 64.4 (Aug. 1988), R29–R64. ISSN: 00218979. DOI: doi:10.1063/1.341700. (Visited on 07/26/2013).

[29] M. Nawrocki et al. "Exchange-Induced Spin-Flip Raman Scattering in a Semimagnetic Semiconductor". In: *Phys. Rev. Lett.* 46 (11 Mar. 1981), pp. 735–738. DOI: 10.1103/PhysRevLett.46.735.

[30] Tran Hong Nhung et al. "Acceptor-bound magnetic polaron in $Cd_{1-x}Mn_xTe$ semimagnetic semiconductors". In: *Phys. Rev. B* 31 (4 Feb. 1985), pp. 2388–2395. DOI: 10.1103/PhysRevB.31.2388.

[31] M. Bugajski et al. "Acceptor-bound magnetic polarons in $Cd_{1-x}Mn_xTe$". In: *Phys. Rev. B* 38 (15 Nov. 1988), pp. 10512–10516. DOI: 10.1103/PhysRevB.38.10512.

[32] Yu. G. Kusrayev et al. "Bound magnetic polarons in the very dilute regime". In: *Phys. Rev. B* 77 (8 Feb. 2008), p. 085205. DOI: 10.1103/PhysRevB.77.085205.

[33] P.A. Wolff. "Chapter 10 Theory of Bound Magnetic Polarons in Semimagnetic Semiconductors". In: ed. by Jacek K. Furdyna and Jacek Kossut. Vol. 25. Semiconductors and Semimetals. Elsevier, 1988, pp. 413–454. DOI: http://dx.doi.org/10.1016/S0080-8784(08)62426-6.

[34] A. V. Kavokin and K. V. Kavokin. "Theory of two-dimensional magnetic polarons in an external magnetic field". In: *Semiconductor Science and Technology* 8.2 (1993), p. 191. URL: http://stacks.iop.org/0268-1242/8/i=2/a=008.

[35] I. A. Merkulov et al. "Parameters of the magnetic polaron state in diluted magnetic semiconductors Cd-Mn-Te with low manganese concentration". In: *Phys. Rev. B* 54 (8 Aug. 1996), pp. 5727–5731. DOI: 10.1103/PhysRevB.54.5727.

[36] T. Dietl. "Handbook of semiconductors". In: ed. by S. Mahajan. Vol. 3b. North-Holland, Amsterdam, 1994. Chap. Diluted magnetic semiconductors, p. 1252.

[37] S. M. Ryabchenko and Yu. G. Semenov. "Spin-correlation effects for a large-radius electron center in a magnetically mixed semiconductor". In: *JETP* 57 (4 Apr. 1983), pp. 825–833. URL: http://www.jetp.ac.ru/cgi-bin/e/index/e/57/4/p825?a=list.

[38] A. V. Kavokin and K. V. Kavokin. "Self-trapping of an exciton in a quantum well with a semimagnetic barrier". In: *Sov. Phys. Semicond.* 25 (1991), p. 1053.

[39] K. V. Kavokin and A. V. Kavokin. "Comment on "Theoretical investigation of observed magnetic-polaron energies in quantum wells"". In: *Phys. Rev. B* 53 (4 Jan. 1996), pp. 2141–2142. DOI: 10.1103/PhysRevB.53.2141.

[40] P Lebrun. *Superfluid helium as a technical coolant*. Tech. rep. LHC-Project-Report-125. CERN-LHC-Project-Report-125. revised version submitted on 2004-08-19 14:20:41. Geneva: CERN, July 1997.

[41] T. Godde et al. "Subnanosecond delay of light in $Cd_xZn_{1-x}Te$ crystals". In: *Physical Review B* 82.11 (2010), p. 115332. DOI: 10.1103/PhysRevB.82.115332. URL: http://link.aps.org/doi/10.1103/PhysRevB.82.115332 (visited on 06/21/2012).

[42] S. Permogorov. "Excitons". In: ed. by E. I. Rashba. North-Holland Publishing Company, Amsterdam; New York; Oxford, 1982. Chap. Optical Emission due to Exciton Scattering by LO Phonons in Semiconductors, pp. 177–203.

[43] *Fresnel equations*. en. Page Version ID: 557723980. May 2013. URL: http://en.wikipedia.org/w/index.php?title=Fresnel_equations&oldid=557723980 (visited on 06/03/2013).

[44] F. Evangelisti, A. Frova, and F. Patella. "Nature of the dead layer in CdS and its effect on exciton reflectance spectra". In: *Phys. Rev. B* 10 (10 Nov. 1974), pp. 4253–4261. DOI: 10.1103/PhysRevB.10.4253.

[45] G. Malpuech and A. V. Kavokin. "Picosecond beats in coherent optical spectra of semiconductor heterostructures: photonic Bloch and exciton-polariton oscillations". In: *Semiconductor Science and Technology* 16.3 (Mar. 2001), R1–R23. ISSN: 0268-1242, 1361-6641. DOI: 10.1088/0268-1242/16/3/201.

[46] M. Born Landau and E. Wolf. *Principles of Optics*. Pergamon Press, Oxford, 1980.

[47] R. Sooryakumar, M. Cardona, and J.C. Merle. "Resonant Brillouin scattering in cadmium telluride". In: *Solid State Communications* 48.7 (Nov. 1983), pp. 581–584. ISSN: 0038-1098. DOI: 10.1016/0038-1098(83)90519-7. URL: http://www.sciencedirect.com/science/article/pii/0038109883905197 (visited on 07/20/2012).

[48] R. Romestain and C. Weisbuch. "Optical Detection of Cyclotron Resonance in Semiconductors". In: *Physical Review Letters* 45.25 (Dec. 1980), pp. 2067–2070. DOI: 10.1103/PhysRevLett.45.2067. (Visited on 05/27/2013).

[49] Le Si Dang, G. Neu, and R. Romestain. "Optical detection of cyclotron resonance of electron and holes in CdTe". In: *Solid State Communications* 44.8 (1982), pp. 1187–1190. ISSN: 0038-1098. DOI: 10.1016/0038-1098(82)91082-1.

[50] A. M. STONEHAM. "Shapes of Inhomogeneously Broadened Resonance Lines in Solids". In: *Rev. Mod. Phys.* 41 (1 Jan. 1969), pp. 82–108. DOI: 10.1103/RevModPhys.41.82. URL: http://link.aps.org/doi/10.1103/RevModPhys.41.82.

[51] T. V. Shubina et al. "Delay and distortion of slow light pulses by excitons in ZnO". In: *Phys. Rev. B* 84 (7 Aug. 2011), p. 075202. DOI: 10.1103/PhysRevB.84.075202.

[52] T. V. Shubina et al. "Excitonic parameters of GaN studied by time-of-flight spectroscopy". In: *Applied Physics Letters* 99.10 (Sept. 2011), pages. ISSN: 00036951. DOI: doi:10.1063/1.3625431.

[53] T. V. Shubina et al. "Resonant Light Delay in GaN with Ballistic and Diffusive Propagation". In: *Phys. Rev. Lett.* 100 (8 Feb. 2008), p. 087402. DOI: 10.1103/PhysRevLett.100.087402.

[54] J. Crank. *The mathematics of diffusion*. Qxford University Press, 1980.

[55] G.N. Ramachandran and S. Ramaseshan. "Crystal Optics". In: *Crystal Optics - Diffration*. Ed. by S. Flügge. Vol. XXV.1. Encyclopedia of Physics. Springer-Verlag, Berlin, 1961.

[56] K. Cho et al. "Theory of degenerate 1s excitons in zinc-blende-type crystals in a magnetic field: Exchange interaction and cubic anisotropy". In: *Phys. Rev. B* 11 (4 Feb. 1975), pp. 1512–1521. DOI: 10.1103/PhysRevB.11.1512.

[57] M. Altarelli and Nunzio O. Lipari. "Perturbation-Theory Investigation of the Exciton Ground State of Cubic Semiconductors in a Magnetic Field". In: *Phys. Rev. B* 7 (8 Apr. 1973), pp. 3798–3802. DOI: 10.1103/PhysRevB.7.3798.

[58] H. Venghaus. "Valence-band parameters and g factors of cubic zinc selenide derived from free-exciton magnetoreflectance". In: *Phys. Rev. B* 19 (6 Mar. 1979), pp. 3071–3082. DOI: 10.1103/PhysRevB.19.3071.

[59] T. Godde. "Magnetische Exziton-Polaronen in II-VI Halbleitern". Diplomarbeit. Technische Universität Dortmund, Experimentelle Physik IIa, Mar. 2009.

[60] T. Godde et al. "Exciton magnetic polaron in CdMnSe/CdMgSe quantum wells". In: *phys. stat. sol. (b)* 247.6 (June 1, 2010). 00001, pp. 1508–1510. ISSN: 1521-3951. DOI: 10.1002/pssb.200983277. URL: http://onlinelibrary.wiley.com/doi/10.1002/pssb.200983277/abstract (visited on 06/15/2014).

[61] I. I. Reshina et al. "Direct and indirect excitons and magnetic polarons in CdSe/CdMgSe/CdMnSe semimagnetic double quantum wells". In: *Phys. Rev. B* 74 (23 Dec. 2006), p. 235324. DOI: 10.1103/PhysRevB.74.235324.

[62] W. Shan et al. "Determination of the fundamental and split-off band gaps in zinc-blende CdSe by photomodulation spectroscopy". In: *Phys. Rev. B* 50 (11 Sept. 1994), pp. 8012–8015. DOI: 10.1103/PhysRevB.50.8012.

[63] A.V. Kavokin. "The lifetime of quasi free exciton magnetic polaron in a quantum-well with semimagnetic barriers". In: *Journal de Physique IV* 3 (C5 Oct. 1993), pp. 79–82. DOI: 10.1051/jp4:1993514.

[64] E. L. Ivchenko and G.E. Pikus. *Superlattices and other heterostructures.* Springer series in solid-state sciences. Springer, 1997. ISBN: 978-3-642-64493-1. URL: http://link.springer.com/book/10.1007/978-3-642-60650-2.

[65] B. Huhn-Heinrich et al. "Zeeman pattern of semimagnetic (CdMn)Te/(CdMg)Te quantum wells in inplane magnetic fields". In: *Solid Stat Commun.* 91.6 (1994), pp. 413–418.